

# Predicting Hemodynamic Changes During Cardiac Growth

---

A

Thesis

Presented to

the faculty of the School of Engineering and Applied Science

University of Virginia

---

in partial fulfillment

of the requirements for the degree

Master of Science

by

Vignesh Valaboju

May 2022

# APPROVAL SHEET

This  
Thesis  
is submitted in partial fulfillment of the requirements  
for the degree of  
Master of Science

Author: Vignesh Valaboju

This Thesis has been read and approved by the examining committee:

Advisor: Jeffrey W. Holmes M.D., Ph.D.

Advisor:

Committee Member: Richard J. Price Ph.D.

Committee Member: Matthew B. Panzer Ph.D.

Committee Member: Scott Lim M.D.

Committee Member:

Committee Member:

Committee Member:

Accepted for the School of Engineering and Applied Science:



Jennifer L. West, School of Engineering and Applied Science

May 2022

# PREDICTING HEMODYNAMIC CHANGES DURING CARDIAC HYPERTROPHY

Vignesh Valaboju

Department of Biomedical Engineering, University of Virginia

## ACKNOWLEDGEMENTS

The work presented below in my thesis is a culmination of intellectual efforts by my mentors, friends, and family. I would like to extend my sincerest gratitude to all those who supported me every day and encouraged me to be the best engineer possible. An acknowledgements page does not do enough justice for the support I have received throughout my time at the University of Virginia (UVA).

I would first like to thank my mentor Pim Oomen for his endless guidance and support. He was there for me starting day 1 when I joined the lab in summer 2019. Much of my knowledge about cardiac mechanics and computational modeling is because of Pim. He always encouraged me to strive to be the best engineer possible. I will miss rolling my chair around and asking Pim the most naïve of questions about my why code is crashing. I would also like to thank my advisor, Jeffrey Holmes. Dr. Holmes took the time to not only help me produce quality research, but also to make sure I appreciated the clinical impact of my research. He made sure I enjoyed the work I was doing and supported me even during his busiest times.

Thank you to the entire Cardiac Biomechanics Group for making me feel at home every time I came into lab. Specifically, thank you to Kyoko for responding to my email I sent my second year of undergrad and willing to show me the amazing research you and the lab were conducting. Thank you to Derek for always being there as a mentor and friend, especially when the lab diminished in size.

I must thank all my friends in undergrad during my time at UVA. Especially my roommates Ramiz, Gurveer, and Daniel. Whether it be running to the corner to celebrate the National Championship or eating dinner together on our tiny table, they made my time at UVA memorable. A special thanks to BME brother, Ramiz, who edited all my writing and fixed all my algebra mistakes no matter the time of day.

My fifth year at UVA would not have been possible without the help and support of the amazing friends that I made in graduate school. I will miss the weekly trivia nights and Friday night drinks. They pushed me to be a better researcher, always asking intriguing questions about my work and sharing the insights of their work.

And most importantly, I would like to thank my mother, father, and sister – Nitha, Vijay, and Vrinda Valaboju. I cannot thank them enough for supporting my endeavors financially and emotionally these past five years. We would have daily facetime calls every night to catch up, and I would look forward to seeing them every night regardless of how busy I was. My parents made numerous trips down to Charlottesville, on minutes notice, to help me with whatever I needed. My sister was always there to share a laugh and support me anytime of the day. Thank you to my family for shaping the man I am today.

## ABSTRACT

Heart failure (HF), a progressive disorder with high mortality rates, currently affects 6 million Americans. One of the main causes of HF is left ventricular (LV) hypertrophy: a structural abnormality that results from growth of LV walls during cardiomyopathy, arterial hypertension, and/or valve disease. Valve diseases such as aortic stenosis and mitral regurgitation cause pressure and volume overloading of the heart, respectively. Chronic progression of volume and pressure overload leads to large amounts of LV hypertrophy resulting in HF. Prospective patient-specific computational models of LV hypertrophy have the potential to aid diagnoses and drive development of tailored treatment plans to prevent progression of HF. As a result, our lab previously developed a rapid-computational growth model of the LV to model cardiac growth during pressure and volume overload. Although successful in accurately predicting growth, the model could only do so retrospectively because it relied on several hemodynamic parameters that were manually prescribed. To prospectively model patients, hemodynamic changes are often unknown and must be predicted to accurately model LV growth. Thus, this thesis aimed to develop a hemodynamic model that predicts hemodynamic changes to model LV growth during pressure and volume overload. (1) We modeled baroreceptor reflexes to predict short-term hemodynamic changes immediately following the onset of pressure or volume overload in canines. (2) We then modeled the renin-angiotensin II system to predict long-term hemodynamic changes several months after the onset of pressure and volume overload in canines. (3) Lastly, we coupled our short- and long-term hemodynamic models with the rapid-computational growth model to predict regression of LV hypertrophy following MitraClip implantation in individual mitral regurgitation patients. Overall, we built a hemodynamic and cardiac growth modeling framework to prospectively model patient-specific responses and help guide personalized treatments to prevent progression of HF.

# TABLE OF CONTENTS

|   |             |
|---|-------------|
| <b>ACKNOWLEDGEMENTS</b> .....   | <b>1-2</b>  |
| <b>ABSTRACT</b> .....   | <b>1-3</b>  |
| <b>1 CHAPTER 1: INTRODUCTION AND BACKGROUND</b> .....                                       | <b>1-6</b>  |
| 1.1 SIGNIFICANCE OF HEART FAILURE .....   | 1-6         |
| 1.1.1 <i>Left Ventricular Hypertrophy</i> .....   | 1-6         |
| 1.2 CARDIAC GROWTH MODELING .....   | 1-7         |
| 1.3 HEMODYNAMICS DURING CARDIAC GROWTH .....  | 1-8         |
| 1.4 EXISTING HEMODYNAMIC MODELS .....   | 1-9         |
| 1.5 GOALS & OBJECTIVES .....  | 1-11        |
| <b>2 CHAPTER 2: SHORT-TERM REFLEX SYSTEM</b> .....  | <b>2-13</b> |
| 2.1 INTRODUCTION.....   | 2-13        |
| 2.2 METHODS .....   | 2-14        |
| 2.2.1 <i>Rapid-Computational Model of Cardiac Growth and Mechanics</i> .....                | 2-14        |
| 2.2.2 <i>Modifying Rapid-Computational Model to Account for Baroreceptor Location</i> ..... | 2-15        |
| 2.2.3 <i>Constructing the Physiologically Detailed Short-Term Reflex Model</i> .....        | 2-17        |
| 2.2.4 <i>Constructing the Phenomenological Short-Term Reflex Model</i> .....                | 2-20        |
| 2.2.5 <i>Overview of 3 Different Short-Term Reflex Models</i> .....                         | 2-22        |
| 2.3 RESULTS.....  | 2-22        |
| 2.3.1 <i>Physiologically Detailed Short-Term Reflex Model Results</i> .....                 | 2-22        |
| 2.3.2 <i>Physiologically Detailed Capacitance-Controlled Short-Term Reflex Model</i> .....  | 2-25        |
| 2.3.3 <i>Phenomenological Short-Term Reflex Model Results</i> .....                         | 2-27        |
| 2.4 DISCUSSION .....  | 2-31        |
| 2.4.1 <i>Comparing the 3 Short-Term Reflex Models</i> .....                                 | 2-33        |
| <b>3 CHAPTER 3: LONG-TERM REFLEX SYSTEM</b> .....   | <b>3-37</b> |
| 3.1 INTRODUCTION.....   | 3-37        |
| 3.2 METHODS .....   | 3-38        |
| 3.2.1 <i>Adapting Long-Term SBV</i> .....   | 3-38        |
| 3.2.2 <i>Coupling the Short- and Long-term Reflex Systems</i> .....                         | 3-38        |
| 3.2.3 <i>Reflex System Fitting and Validation</i> .....                                     | 3-39        |
| 3.3 RESULTS.....  | 3-40        |
| 3.4 DISCUSSION .....  | 3-45        |
| <b>4 CHAPTER 4: CLINICAL MODEL VALIDATION WITH MITRACLIP PATIENTS</b> .....                 | <b>4-47</b> |
| 4.1 INTRODUCTION.....   | 4-47        |
| 4.2 METHODS .....   | 4-48        |
| 4.2.1 <i>Curating the Dataset</i> .....   | 4-48        |
| 4.2.2 <i>Fitting Baseline State for Patients</i> .....                                      | 4-50        |
| 4.2.3 <i>Using Rapid-Computational Model and Reflex Model to Predict LV Growth</i> .....    | 4-53        |
| 4.3 RESULTS.....  | 4-54        |
| 4.3.1 <i>Exploratory MitraClip Dataset Analysis</i> .....                                   | 4-54        |
| 4.3.2 <i>Patient-Specific Modeling Results</i> .....  | 4-56        |
| 4.4 DISCUSSION .....  | 4-62        |
| <b>5 CHAPTER 5: CONCLUSIONS AND FUTURE DIRECTIONS</b> .....                                 | <b>5-65</b> |
| 5.1 SHORT-TERM REFLEX MODELING.....   | 5-65        |
| 5.2 LONG-TERM REFLEX MODELING .....   | 5-66        |
| 5.3 MITRACLIP PATIENT-SPECIFIC MODELING .....   | 5-67        |

|          |                         |             |
|----------|-------------------------|-------------|
| <b>6</b> | <b>APPENDICES</b> ..... | <b>6-69</b> |
| 6.1      | APPENDIX A.....         | 6-69        |
| 6.2      | APPENDIX B.....         | 6-72        |
| 6.3      | APPENDIX C.....         | 6-74        |
| 6.4      | APPENDIX D.....         | 6-76        |
| 6.5      | APPENDIX E.....         | 6-77        |
| <b>7</b> | <b>REFERENCES</b> ..... | <b>7-78</b> |

# 1 CHAPTER 1: INTRODUCTION AND BACKGROUND

## 1.1 SIGNIFICANCE OF HEART FAILURE

Nearly 6 million Americans have heart failure (HF) with a mortality rate of 45-60% within five years after diagnosis [1], [2]. It is expected that total medical costs of HF will increase from \$31 billion to \$70 billion by 2030 [3]. HF can be caused by various structural and functional abnormalities of the myocardium such as altered myocardial material properties, dysfunction of the pericardium, dysfunction of the heart valves, and/or diseased coronary arteries [4]. Understanding the physiological mechanisms of HF can help guide diagnosis and treatment of cardiovascular diseases to prevent HF. One of the main causes of HF is left ventricular (LV) hypertrophy: a structural abnormality that results from growth of the LV walls during cardiomyopathy, arterial hypertension, and/or valve disease [5]. Aortic stenosis and mitral regurgitation (MR), which are two common valve diseases, cause LV hypertrophy and ultimately HF due to pressure and volume overloading of the LV, respectively.

### *1.1.1 Left Ventricular Hypertrophy*

Both pressure and volume overloading of the LV cause LV hypertrophy, a key independent risk factor for HF, which is a response mechanism to deal with the increased overload of the heart [6]. There are two main types of LV hypertrophy: eccentric and concentric hypertrophy [7]–[12].

Volume overload is a pathological state that results in eccentric hypertrophy. LV cavity diameter and mass increase due to sarcomeres lengthening and being added in series [13]. During MR, a valve disease, blood is regurgitated from the LV back into the left atrium. Since the blood ejected from the LV during systole does not all go into systemic circulation, the regurgitation causes an increased amount of blood to be pumped by the LV and results in larger end diastolic volumes (EDV) [9], [10].

Concentric hypertrophy is observed in conditions that increase afterload and is characterized by thickening of the myocardial wall due to sarcomeres being added in parallel [13]. LV pressure overload is a pathological state in which higher than normal pressures are required to pump blood out of the aortic valve which leads to prolonged and increased afterload. Pressure overload has been shown to produce changes in stress, strain, and circulating hormones; these changes combine to stimulate myocyte growth [14]. During aortic stenosis, a valve disease, the calcified aortic valve cusps make it difficult to pump blood across the valve at normal pressures. As a result, pressure overload is developed, and is associated with increased LV systolic and diastolic pressures [12], [15], [16].

Understanding how the LV grows during pressure and volume overload will allow for better predictions of long-term remodeling that leads to HF and potential evaluation of patient responses to therapies designed to prevent or treat failure. Although the underlying mechanism that causes eccentric and concentric hypertrophy is still unknown, hormonal, electrical, and mechanical stimuli have all been shown to drive cardiomyocyte growth and remodeling [17]. Prospective mathematical models using hormonal, electrical, and mechanical stimuli have been shown to successfully predict hypertrophy and regression of hypertrophy in response to pressure and volume overload [14], [18]–[20]. These prospective mathematical models can be used to predict patient-specific therapy outcomes during pressure and volume overload. For instance, following mitral valve replacement or mitral valve repair for MR patients, the LV is expected to undergo reverse hypertrophy to reduce cavity diameter. Mitral valve repair and replacement are different procedures with diverse risk profiles that may lead to variable outcomes depending on the amount of the MR that needs to be reduced [21]. Therefore, predicting outcomes for individual patients before surgery could provide clarity in selecting the best treatment possible. In addition, patient-specific mathematical models of the heart allow us output detailed information about LV pressures and volumes at several time points that cannot be measured clinically. Clinicians can use these detailed model outputs to provide better treatments and diagnostics.

## 1.2 CARDIAC GROWTH MODELING

A wide range of cardiac growth models have been developed to successfully capture concentric and eccentric hypertrophy during pressure and volume overload. The geometric changes that occur, such as changes to the diameter of the cavity and thickness of the myocardium, are key factors in determining the course and severity of the HF that develops. Therefore, subsequent treatments could be guided using the provided model predictions such as changes in LV mass, end diastolic wall thickness, and maximum LV volumes. Hypertrophy often occurs on a spectrum ranging from concentric to eccentric, and the growth is progressive; therefore, simply predicting the expected remodeling in individual patients could also have important prognostic value in determining how closely to monitor, when to treat, etc. [22], [23].

It is widely accepted that mechanics play an essential role in tissue growth and remodeling. Computational models have been able to successfully predict cardiac growth using differential equations that predict growth as a function of stress and/or strain [7], [18], [19], [24]. The so-called growth laws usually assume that myocardium grows to drive stress and/or strain back to a homeostatic setpoint; therefore, larger changes in stress or strain result in more growth [7]. Consequently, growth causes a change in tissue volume because myocardium is added or subtracted, and in many models the amount and direction of these changes are specified by a growth deformation tensor [25]. Many models also assume that growth is driven based on the

change in stress or strain between a baseline (before intervention) and acute state (immediately after intervention) [26]. During volume overload (eccentric growth), the LV grows in the fiber direction where the LV cavity dilates resulting in larger end diastolic internal diameters and larger EDVs. During pressure overload (concentric growth), the LV grows in the radial direction where the LV wall thickens resulting in larger end diastolic wall thickness and larger systolic pressures.

The aforementioned growth laws can be applied within a wide array of models ranging from the cellular to organ level scales. The stresses and strains can be computed locally for each cardiomyocyte/region of the LV or on a global scale for the whole LV depending on the physiological detail needed from the model. Since the geometry of the LV is often complicated and the myocardium is mechanically anisotropic with varying myocardial fiber orientations, 3D finite-element models can be used to compute changes in stress or strain at many locations within the LV. Computing local mechanics in a finite-element model provides excellent anatomical details that can be used to drive local myocardial growth but is also relatively computationally expensive [27]. Kerckhoffs et al. developed a non-linear finite-element model that modeled LV growth during pressure and volume overload using a single set of strain based equations; however the model is computationally expensive taking over 3 weeks to simulate 1 month growth on a fairly powerful computer [18], [26].

Cardiac growth models have the potential to guide time-sensitive surgeries in routine clinical settings because they can predictively model each patient's needs; however, to achieve that goal, models must be calibrated and run in a short time period to best guide clinical interventions [23]. To this end, our lab previously developed a rapid-computational model of the heart and circulation system that can predict growth following pressure overload, volume overload, and myocardial infarction using Kerckhoffs growth law [18]. The rapid-computational model treats the LV as a thin-walled sphere. The geometry of a sphere is much simpler than that of a finite-element LV; as a result, computing the mechanics is much simpler and faster. Despite simplifying the LV to a sphere, our rapid-computational model still accurately predicted 3 months of growth during pressure overload, volume overload, and myocardial infarction in under 3 minutes on a local 16GB machine. We suspect that this was possible because the global changes in mechanics associated with severe disease are more sizable than the regional differences. Rondonina and Bovendeerd also developed a thin-walled LV sphere computational model using a different growth law that calculates growth based on the myofiber stress and sarcomere length. They were also able to accurately predict growth during pressure and volume overload without the detail needed from a finite-element model [24].

### 1.3 HEMODYNAMICS DURING CARDIAC GROWTH

Hemodynamics have been shown to play a vital role in cardiac growth and are consequently incorporated into cardiac growth modeling. Witzenburg and Holmes showed that pressure and

volume overload predictions using the rapid-computational model are highly sensitive to hemodynamic perturbations [18]. They also showed that, when using the rapid-computational model to predict growth post myocardial infarction, perturbations to hemodynamics such as heart rate (HR), vascular resistance, and blood volumes greatly affected growth outcomes six weeks after infarction [28]. Patients with aortic stenosis often have reduced systemic arterial compliance which results in different severity levels of aortic stenosis and ultimately varying degrees of pressure overload [29]. Modeling hemodynamics such as systemic arterial compliance is necessary to compute the degree of concentric hypertrophy in patients with aortic stenosis. Rondanina and Bouvendeerd best matched patient EDVs and wall thicknesses following aortic stenosis, aortic regurgitation, or mitral regurgitation when they modeled hemodynamic changes concurrently with LV growth [30].

As a result, cardiac models using growth laws require a circulation system to control the hemodynamics during a cardiac cycle. The circulation system is also used control the hemodynamic overloading during pressure and volume overload.

The rapid-computational model developed by Witzenburg and Holmes used a lumped-parameter circuit model of the circulation system previously published by Santamore and Burkhoff [31]. Blood flow and volumes across the circulation are controlled by arterial and venous resistances and capacitors. Pressures in the LV during the cardiac cycle are determined through a time varying elastance model. End-diastolic pressures (EDP) are determined volume and an exponential pressure-volume relationship reflecting nonlinear material properties, while end-systolic pressures (ESP) are determined by a linear, time-varying elastance contraction model [31].

In both of the Witzenburg and Holmes [18] and Rondanina and Bovendeerd [24] computational models, hemodynamic parameters such as systemic vascular resistance, stressed blood volume (SBV), and heart rate were essential inputs to run a cardiac cycle and compute growth; however, these parameters were manually input to the models during growth. When growth models are used retrospectively to predict patterns that have already been observed in patients or animals, hemodynamic data are available as model inputs. Unfortunately, for prospective modeling of cardiac growth in patients, these parameters are unknown yet essential for computing growth. Kerckhoffs et al. discuss that in the absence of a hemodynamic adaptation system, they cannot match experimental blood pressures during chronic pressure overload with their LV growth model [26]. To allow for patient-specific, prospective growth modeling of pressure and volume overload, predicting the hemodynamics across cardiac cycles is essential.

## 1.4 EXISTING HEMODYNAMIC MODELS

Similar to how cardiac growth models use stimuli to predict growth, hemodynamic models use various organ and cellular stimuli to predict hemodynamics. To maintain blood flow

and pressure at homeostasis, the body uses several feedback control systems that adjust vascular resistances, vascular compliances, and cardiac output. Two of the main physiological feedback control systems that influence cardiac function include the baroreflex and renin-angiotensin systems.

The baroreflex system is comprised of neurons called baroreceptors that are located in the aortic arch and carotid sinus. Baroreceptors detect changes in arterial wall stretch which initiate action potentials that modulate the sympathetic and parasympathetic nervous system to regulate heart rate, cardiac output, and vascular resistances. Baroreceptors control mean arterial pressure (MAP) using a negative feedback loop. When there is an increase in blood pressure, the baroreceptor firing rate increases leading to increased inhibition of sympathetic outflow to the peripheries. This results in vasodilation, and the opposite is true when there is a decrease in MAP [32]. Baroreceptors are mainly responsible for controlling short-term changes in blood pressure on the order of seconds to minutes [33]–[35].

The renin-angiotensin system (RAS) is responsible for controlling blood volumes, water and salt balances, through modulation of circulating hormone concentrations [36]. Juxtaglomerular cells in the arterioles of the kidneys respond to changes in blood pressure and decreased sodium levels resulting in the formation of renin. Renin is then released into the bloodstream where renin activates angiotensin II (ang-II) through the help of angiotensin converting enzyme [37]. Ang-II is responsible for vasoconstriction which helps the body regulate systemic vascular resistances and blood volumes [37]. The RAS has been shown to help regulate chronic hemodynamic changes during cardiac hypertrophy. More specifically, RAS is responsible for long term (order of hours to days) regulation of blood volumes and arterial pressures [33], [36].

Just as cardiac growth models range widely in complexity, predictive models of short- and long-term hemodynamic changes vary in complexity and physiological detail. Beard et al. developed an ordinary differential equations (ODE) model that models 6 different regulatory systems. The model captured short- and long-term changes in hemodynamics due to different interventions such as hemorrhages and blood volume infusions [33]. Mahdi et al. developed a hemodynamic model that focused on the modeling the mechanoreceptors that control baroreceptor firing rates. They modeled, in high detail, baroreceptor responses to changing pressure stimuli [35]. In terms of baroreceptor reflexes, both hemodynamic models model the mechanical changes occurring in the arterial wall to regulate baroreceptor firing; however, Mahdi et al. has a more physiologically detailed setup of viscoelastic components and membrane conductance. As a result, the model can better match experimental data for a wider array of pressure stimuli with varying frequencies and amplitudes. Beard et al. trades off this detail for a more phenomenological representation of the baroreceptor response so that systems for long-term regulation can also be included in the model. Mahdi et al. uses a computationally expensive system to capture baroreceptor activity whereas Beard et al. uses fewer parameters in the

baroreceptor model component to allow for modeling of more regulatory systems with less computational demand.

Rondanina and Bovendeerd showed that hemodynamic models of regulation can be further simplified by indirectly modeling the baroreceptors and RAS [30]. Beard et al. controlled the sympathetic tone of the vasculature based on baroreceptor responses due to changes in arterial stretch and long-term blood volumes based on renin-angiotensin II levels. On the other hand, Rondanina and Bovendeerd used a system of 2 differential equations to control peripheral vascular resistance and stressed blood volume (SBV) [30], [33]. Since baroreceptors and the RAS indirectly control cardiac output (CO) and MAP, Rondanina and Bovendeerd assumed that CO and MAP always drive back to a homeostatic setpoint and used that principle to control peripheral vascular resistance and SBV – a simplified method of modeling one of the functions of the baroreceptors and SBV [30]. The trade-off for more detailed baroreceptor and RAS responses is computational cost and model simplicity.

## 1.5 GOALS & OBJECTIVES

The aforementioned hemodynamic models by Beard et al. and Rondanina and Bovendeerd can predict key hemodynamic values, such as vascular resistance, SBV, and HR, that are essential to compute cardiac growth. Rondanina and Bovendeerd coupled their hemodynamic model to a simplified LV growth model [30]; however, the lack of separate short- and long-term hemodynamic systems results in limited patient-specific modeling capabilities for cardiac hypertrophy. Witzenburg and Holmes showed that hemodynamics play a major role in cardiac hypertrophy, and that the rapid-computational model is sensitive to hemodynamic changes [18], [28]. In terms of long-term hemodynamic changes during volume overload, one of the studies that the Witzenburg and Holmes modeled reported pulmonary congestion, suggesting that the hemodynamic parameter stress blood volume needs to be adapted during chronic volume overload [18]. Reducing systemic vascular resistance has been previously shown to work as a therapy for severe MR; thus, modeling the changes in vascular resistance using a coupled hemodynamic and growth model will allow us to predict how a patient may respond to this therapy [38]. Yoshida et al. recently showed that modeling of ‘reverse’ growth (regression of hypertrophy) is useful for modeling how the heart adapts after an intervention to treat pressure or volume overload [19]. Homeostatic setpoints for MAP and CO will likely adapt after interventions for treatment such as mitral valve or aortic valve repair. During retrospective modeling, we can manually feed in hemodynamic information to match growth; however, to prospectively model LV growth in patients, we must predict hemodynamic changes necessary for growth.

Thus, the goal of this thesis is to develop a short- and long-term hemodynamic model coupled with rapid-computational growth model to accurately predict LV growth during pressure

and volume overload. In Chapter 2, we will explore two hemodynamic models that differ in complexity and couple them with a rapid-computational model to predict acute short-term (minutes after an intervention) changes during pressure and volume overload in canines. Chapter 3 will then incorporate a long-term (days or months after intervention) hemodynamic control system to predict chronic changes in pressure and volume overload in canines. Lastly, Chapter 4 will aim to test the clinical feasibility of our coupled hemodynamic and growth model from Chapters 2 and 3 to model reversal of LV hypertrophy in patients who received mitral valve repair surgery (MitraClip) to treat MR.

## 2 CHAPTER 2: SHORT-TERM REFLEX SYSTEM

### 2.1 INTRODUCTION

Changes in LV mechanics between immediately before an intervention (baseline) and immediately after an intervention (acute) drive cardiac growth in Witzenburg and Holmes' rapid-computational model. Differences in hemodynamics between the baseline and acute states are drivers of those changes in mechanics, and are therefore vital to predicting LV hypertrophy [18]. The rapid-computational model can accurately predict cardiac growth during pressure and volume overload; however, it is not able to predict the hemodynamic changes that occur after inducing pressure or volume overload. As a result, the rapid-computational model was only able to retrospectively model LV hypertrophy since the hemodynamic changes were manually prescribed. Prospective modeling requires predicting hemodynamic changes in addition to cardiac growth because the hemodynamic parameters are not known. As described in section 1.4, hemodynamic models are necessary to predict hemodynamic changes. Physiologically detailed models of the baroreflex can provide hemodynamic predictions necessary for modeling LV growth.

Beard et al. previously developed a detailed physiological model of short- and long-term hemodynamic regulation of arterial pressure by developing a model composed of 6 different systems: aorta/large artery mechanics, kinetics of baroreflex afferent firing, mechanics of the heart and circulation, autonomic system, RAS, and pressure-diuresis/natriuresis. The baroreceptors and autonomic system are the primary regulators of short-term hemodynamic regulation because they regulate the sympathetic tone of the vasculature on the order of seconds to minutes [33].

After an intervention that causes pressure or volume overload, the body immediately responds by adapting HR and vascular constriction to maintain both CO and MAP. The baroreflex system in Beard et al's model controls vaso- and venoconstriction and HR by computing the sympathetic tone of the vasculature based on baroreceptor activity [33]. HR and vascular tone are necessary inputs for the rapid-computational model to compute cardiac growth.

We discussed earlier in section 1.4 that there also exist high-level physiological hemodynamic models (phenomenological hemodynamic models) that represent the activity of several systems with just one or two equations. To calculate growth with the rapid-computational model, the most important hemodynamic parameter of interest is the vascular constriction that determines stressed blood volume and systemic arterial resistance ( $R_{as}$ ). The hemodynamic model previously published by Rondanina and Bovendeerd adapts vascular constriction by trying to maintain homeostatic CO and MAP [30]. Short term CO and arterial pressure are generally controlled by peripheral resistance and compliance, LV pumping capacity,

and blood volumes which all greatly influence acute LV hypertrophy [39]. Since the baroreceptors control sympathetic tone, they lumped together the baroreceptor and autonomic system to indirectly control vascular constriction and blood volumes based on changes in CO and MAP. Rondanina and Bovendeerd showed that without incorporating any baroreflex information, the global average changes in CO and MAP can be matched without the local detail needed from the baroreflex system that Beard et al. uses. However, hemodynamic adaptation is affected by different systems for short- and long-term scales, and the Rondanina and Bovendeerd hemodynamic model cannot differentiate between these scales. This also limits the changes in MAP and CO homeostatic setpoints that may occur during forward and reverse modeling of cardiac hypertrophy. As a result, we treat the Rondanina and Bovendeerd hemodynamic model as only a short-term hemodynamic model and modify their system of ODEs to incorporate baroreflex characteristics. We later develop a long-term hemodynamic model in Chapter 3.

In this chapter, we develop three short-term hemodynamic reflex models that are coupled to our rapid-computational model: two physiologically detailed short-term reflex models and one phenomenological short-term reflex model. The physiologically detailed short-term reflex models use the baroreflex system of ODEs from Beard et al. to compute the short-term hemodynamic changes between the baseline and acute states following sudden creation of pressure or volume overload in canines. In addition, we modify the rapid-computational model so that the circulation system can better reflect the location of the baroreceptors in the carotid artery. To build the phenomenological short-term reflex model, we modify the hemodynamic model built by Rondanina and Bovendeerd to include a baroreflex component to allow specifically for short-term hemodynamic adaptation. The three short-term hemodynamic reflex models are compared to determine which approach is better to predict the hemodynamic changes necessary to model LV growth using the rapid-computational model.

## 2.2 METHODS

### *2.2.1 Rapid-Computational Model of Cardiac Growth and Mechanics*

As previously discussed in section 1.2, our lab previously developed a rapid-computational model of cardiac growth and mechanics that treats the LV as a thin-walled sphere to model cardiac growth during pressure and volume overload [18]. The rapid-computational model uses Kerckhoffs growth law where the differences in LV strain between baseline and acute states are used to calculate growth in the radial (thickening of the LV wall) and fiber (lengthening of the LV wall) directions. To account for hemodynamic loading, the LV and right ventricle are connected to a previously published lumped-parameter circulation system [31]. The systemic and pulmonary arteries and veins are described by capacitors and resistors (**Figure 2.1**). Total blood volume in the system is split up into unstressed and stressed blood volume (SBV). Unstressed

blood volume is the maximum amount of blood that can fit in the system without changing the pressure from 0 mmHg. Any blood volume left over is considered the SBV. SBV and systemic arterial resistance,  $R_{as}$ , were fitted to match experimental pressure or volume overload data. The rapid-computational model was defined by a system of ordinary differential equations for the changes in volume of the LV, right ventricle, system arteries and veins, and the pulmonary arteries and veins.

### 2.2.2 *Modifying Rapid-Computational Model to Account for Baroreceptor*

#### *Location*

We adapted the previously published rapid-computational model for cardiac growth by Witzenburg and Holmes to include the carotid artery baroreceptor response using a system of differential equations from Beard et al. [18], [33]. Prior to incorporating the baroreceptor response, the method of inducing pressure and volume overload in the rapid-computational model had to be changed to account for the location of the baroreceptors. To simulate aortic banded pressure overload in canines, the rapid-computational model originally prescribed an increase in  $R_{as}$  to increase pressure in the LV. However, baroreceptors are located in the ascending aorta, well upstream of the small arterioles that account for most of the resistance in the arterial tree. Furthermore, the studies we are using for fitting and validation induce pressure overload by banding the ascending aorta [8], [11]. Therefore, to incorporate a baroreceptor response into the rapid-computational model, we must simulate pressure overload by constricting the ascending aorta rather than the small arterioles so that the carotid artery baroreceptors can detect the change in pressure. As a result, to best capture the pressure changes detected by the baroreceptors, the rapid-computational model was refitted and validated to induce pressure overload by increasing (characteristic systemic resistance)  $R_{cs}$ , instead of  $R_{as}$ , from baseline to acute. In our rapid-computational model,  $R_{cs}$  is located before the baroreceptors (**Figure 2.1**). The rapid-computational model was fitted and validated against independent canine pressure overload studies [8], [11].

Additionally, to simulate MR volume overload in canines, the rapid-computational model originally prescribed a decrease in mitral valve backflow resistance (MVBR) and an adjustment of  $R_{as}$ . Later in this chapter, we discuss that  $R_{as}$  can be adapted using the baroreceptor response, so we did not want to prescribe  $R_{as}$  to induce volume overload. We also wanted to prescribe as few parameter changes as possible. As a result, we refitted the rapid-computational model to induce volume overload by only prescribing a decrease in MVBR. By decreasing MVBR, blood regurgitates back in the left atrium causing LV volume overload. The rapid-computational model was fitted and validated against independent canine volume overload studies [9], [10]. The optimal parameters from fitting the pressure and volume overload cases are shown in **Appendix Table A.1**. The baseline and acute pressure-volume (PV) loops are shown in **Appendix Figures A.1-2**. The results suggest that we obtained similar baseline and acute PV loops to that of

Witzenburg and Holmes when refitting the pressure and volume overload simulations. For all the pressure and volume overload studies, the growth parameters were not refitted. These versions of the rapid-computational model are used for all subsequent simulations in Chapters 2 & 3.

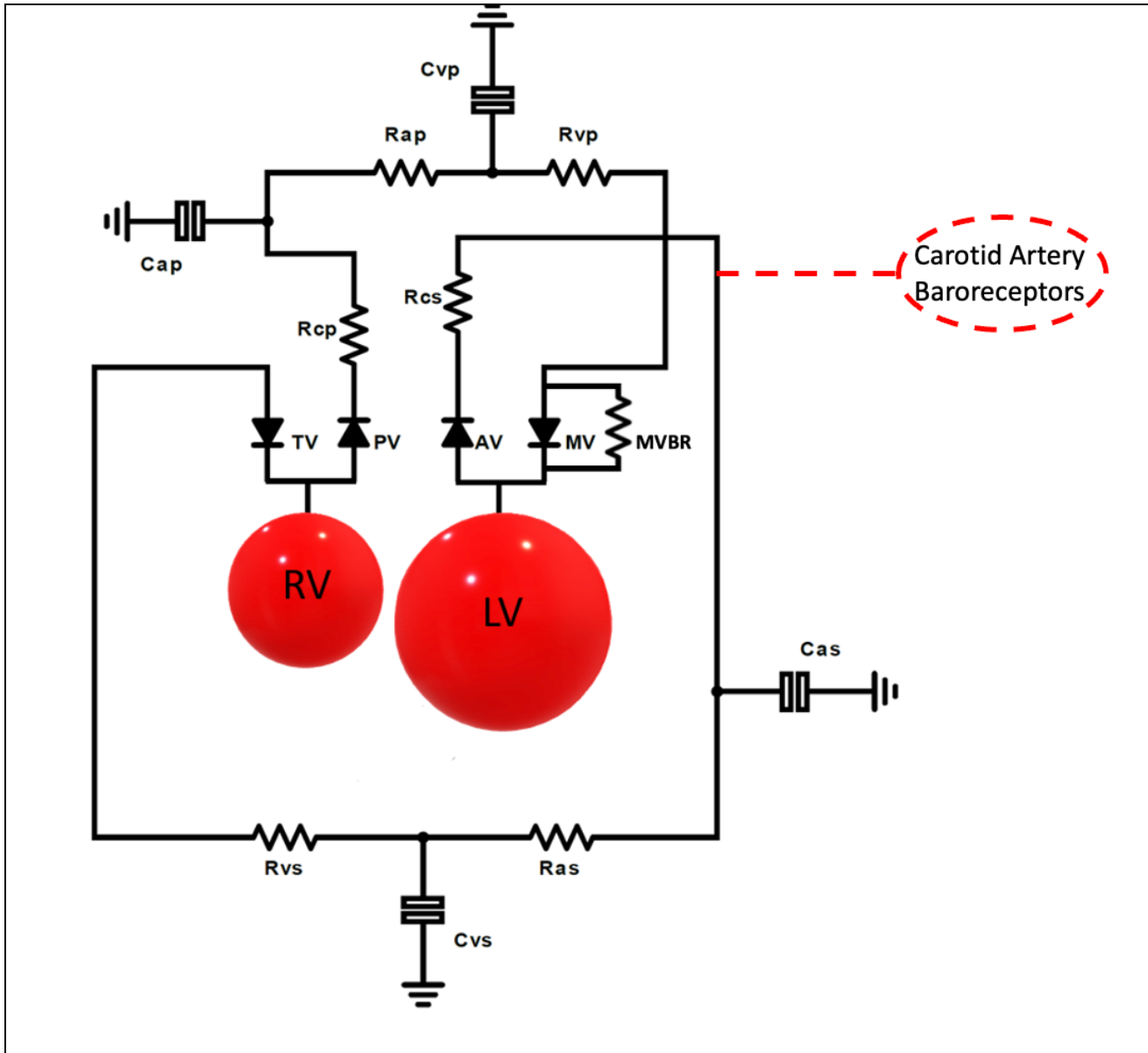


**Figure 2.1:** Depicted is the circuit diagram representation of the lumped parameter system used by the rapid-computational model [18]. The LV and RV are treated as thin-walled spheres, and the heart valves are represented as pressure sensitive diodes (tricuspid, pulmonary, mitral, and aortic valves). The systemic and pulmonary resistances and capacitances are represented as resistors and capacitors.  $R_{cs}$  &  $R_{cp}$ : systemic and pulmonary characteristic resistances.  $R_{as}$  &  $R_{ap}$ : systemic and pulmonary arterial resistances.  $R_{vs}$  &  $R_{vp}$ : systemic and pulmonary venous return resistors.  $C_{as}$  &  $C_{ap}$ : systemic and pulmonary arterial compliance.  $C_{vs}$  &  $C_{vp}$ : systemic and pulmonary venous compliance. To simulate hemodynamic pressure overload,  $R_{cs}$  is increased from the baseline to acute state. To simulate hemodynamic volume overload though mitral regurgitation, the mitral valve backflow resistance (MVBR) is decreased from the baseline to acute state. Note: when  $MVBR = \infty$ , then there is no backflow.

## 2.2.3 Constructing the Physiologically Detailed Short-Term Reflex Model

### 2.2.3.1 Baroreceptor Firing and Sympathetic Tone Control

After modifying the rapid-computational model to account for the baroreceptor location, the baroreceptor component from Beard et al.'s hemodynamic model was adapted to create a physiologically detailed short-term reflex model that can be coupled the rapid-computational model. Beard et al. calculated the baroreceptor afferent firing rate by computing the change in aortic strains. We used a similar approach by calculating the maximum stretch systemic arteries,  $\lambda$ :

$$\lambda_{as} = \sqrt{\frac{V_{as}}{V_{U,as0}}} \quad \text{Equation 2.1}$$

where  $V_{as}$  is the volume in the systemic arteries at maximum pressure in the arteries and  $V_{U,as0}$  is the unstressed blood volume (UBV) in the systemic arteries:

$$V_{U,as0} = \frac{C_{as}}{T_C} (TBV - V_{0LV} - V_{0RV}) \quad \text{Equation 2.2}$$

where  $C_{as}$  is the systemic arterial capacitance,  $T_C$  is sum of all capacitances,  $V_{0LV}$  &  $V_{0RV}$  are the unloaded volumes of the left and right ventricles respectively, and TBV is the total blood volume.. TBV is the sum of UBV and SBV of the system. We will assume that at any one point, the ratio of UBV to SBV is 85% to 15% [40]. We will also assume that  $V_{0LV} = V_{0RV}$ .

Baroreceptor activity is physiologically regulated by changes in stretch of the carotid artery [41]. To capture the maximum arterial stretch after each cardiac cycle, we employed a moving average stretch for the arteries,  $\bar{\lambda}(t)$ :

$$\tau_s \frac{d\bar{\lambda}}{dt} = \lambda_{as} - \bar{\lambda} \quad \text{Equation 2.3}$$

where  $\tau_s$  is an adjustable time constant.  $\tau_s$  determines the length of the moving average window. A saturable relationship is used to calculate the baroreceptor firing rate,  $f_{BR}$ . The firing rate is proportional to  $\delta_\lambda = \max(\lambda_{as} - \bar{\lambda}, 0)$  [33]:

$$f_{BR}(t) = f_0 S(t) \frac{\delta_\lambda}{\delta_\lambda + \delta_0} \quad \text{Equation 2.4}$$

Where  $f_0$  is the adjustable gain parameter,  $\delta_0$  is the adjustable saturation constant, and  $s(t)$  describes the ratio of baroreceptor afferents that are in an active state. The baroreceptors go from active to inactive at a rate proportional to  $f_{BR}$  and go to the active state at a constant rate [33]:

$$\frac{ds}{dt} = a(1 - s) - bs \frac{\delta_\lambda}{\delta_\lambda + \delta_0} \quad \text{Equation 2.5}$$

where  $a$  and  $b$  are adjustable constants. Beard et al. fitted  $\tau_s$ ,  $\delta_0$ ,  $f_0$ ,  $a$ , and  $b$  based on experimental data of step changes in non-pulsatile carotid sinus pressure and pulsatile aortic pressure, and we used identical parameters in our implementation [33], [34], [42]. It is important to note that Beard et al. controls the baroreceptors during every step of the cardiac cycle; however, to limit computational resources, we controlled the baroreceptors once every cardiac cycle.

We used sympathetic tone,  $\varphi_{SN}(t)$ , to control the autonomic system based on baroreceptor reflex arc [33]:

$$\frac{d\varphi_{SN}}{dt} = f_{SN}(1 - \varphi_{SN})(\lambda_{as} \neq \bar{\lambda}) - f_{BR}\varphi_{SN} \quad \text{Equation 2.6}$$

where  $f_{SN}$  is an adjustable constant parameter.  $\varphi_{SN}$  has a range from 0 to 1 and at baseline  $\varphi_{SN}(t) = 0.25$ . When there is a drop in arterial pressure, the sympathetic tone parameter will increase towards 1. At baseline, the  $f_{BR} = 0$  because the arterial strain is equal to the moving average arterial stretch; therefore, the  $(\lambda_{as} \neq \bar{\lambda})$  term ensures that at baseline, there is no change in  $\varphi_{SN}$ .  $(\lambda_{as} \neq \bar{\lambda})$  returns 1 if  $\lambda_{as}$  is not equal to  $\bar{\lambda}$ ; otherwise, the expression returns 0.

### 2.2.3.2 Stress Blood Volume (SBV) and Heart Rate (HR) Adaptation

SBV, HR,  $R_{as}$ , and MVBR are hemodynamic parameters necessary to run the rapid-computational model of growth.  $R_{as}$  or MVBR are prescribed to induce pressure or volume overload, respectively; thus, it is only necessary to predict SBV and HR. Since SBV reflects vaso- and venoconstriction in the rapid-computational model, SBV can be adapted using the sympathetic tone determined by the baroreflex. The sympathetic tone of the system helps control vaso- and veno-constriction. As a result, SBV and HR were both controlled by the sympathetic tone parameter,  $\varphi_{SN}$ :

$$HR = HR_0 + HR_1(\varphi_{SN} - 0.25) \quad \text{Equation 2.7}$$

$$SBV = SBV_0 + SBV_1(\varphi_{SN} - 0.25)$$

Equation  
2.8

where  $HR_0$  and  $SBV_0$  are set so that the minimum HR and SBV can go down to a maximum of 25% lower than the baseline HR and SBV, respectively.  $HR_1$  and  $SBV_1$  are set so that the maximum HR and SBV are set to create upper limits on HR and SBV. At maximal sympathetic tone  $\varphi_{SN}=1$ ; therefore, the upper limit of SBV and HR is the sum of  $SBV_0$  and 75% of  $SBV_1$ . The upper limits were estimated based on the upper range of HR values in the experimental pressure and volume overload datasets [8]–[11] and the upper range of SBV values from Witzenburg and Holmes' rapid-computational model simulations [18].

**Equation 2.1** through **2.8** describe the physiologically detailed short-term reflex model.

### 2.2.3.3 Optional Capacitance Control (Physiologically Detailed Capacitance-Controlled Short-Term Reflex Model)

**Equation 2.8** shows that sympathetic tone can be used to regulate short-term SBV. We now propose an alternative mechanism to simulate vaso- and venoconstriction by adapting systemic arterial capacitance through sympathetic tone. Baretta et al. showed that there is a geometric relationship between the resistance and capacitance of a blood vessel [43]:

$$C_{as_i} = C_{as_0} \left( \frac{R_{as_i}}{R_{as_0}} \right)^{-4}$$

Equation  
2.9

where  $C_{as_i}$  and  $R_{as_i}$  are the arterial capacitance and resistance respectively at each time step increment  $i$ .  $C_{as_0}$  and  $R_{as_0}$  are the initial arterial capacitance and resistance, respectively. Since systemic arterial resistance is directly related to the sympathetic tone parameter, we adapt  $R_{as_i}$  using the equation below:

$$R_{as_i} = R_{as_0} + R_{as_1}(\varphi_{SN} - 0.25)$$

Equation  
2.10

where  $R_{as_1}$  is an arbitrarily set parameter to help define maximum constriction. When capacitance control is used, SBV is kept at baseline throughout the short-term time course. We can simulate constriction by adapting  $C_{as}$  or SBV because they both increase mean pressure. By increasing SBV, more blood is stressed the mean pressure increases which can simulate constriction. By decreasing  $C_{as}$ , we are making the blood vessels in the systemic arteries more

compliant which simulates constriction. HR is adapted at the same rate as shown in **Equation. 2.7**.

**Equation 2.1-2.7** and **Equation 2.9-2.10** describe the physiologically detailed capacitance-controlled short-term reflex model.

#### 2.2.3.4 Physiologically Detailed Short-Term Reflex Model Fitting and Validation

The physiologically detailed short-term reflex model was then fitted and validated for both pressure and volume overload. For pressure overload, the physiologically detailed short-term reflex model, coupled to the rapid-computational model, was fitted to match reported changes in LV EDV, EDP, end-systolic volume (ESV), and maximum pressure (MaxP) 30 minutes after experimental aortic constriction from Sasayama et al. (**Appendix B Equation B.1**) [8]. After fitting, the coupled model was validated using an independent canine aortic constriction study by Nagatomo et al. [11]. For volume overload, the coupled model was tuned to match reported changes in LV EDP, minimum volume (MinV), MAP, and regurgitant fraction (RF) 30 minutes after experimental induction of mitral valve regurgitation (**Appendix B Equation B.2**) by Kleaveland et al. [9]. After fitting, the coupled model was validated against an independent canine mitral valve regurgitation study from Nakano et al. [10]. Note that these are the same fitting and validation studies used to calibrate the rapid-computational model. Fitting was done using the MATLAB 2020b *fminsearch* algorithm [44]. Since the time step,  $dt$ , is a known constant, the short-term reflex system of ODEs can be solved algebraically without a numerical ODE solver.  $dt$  and the time between the baseline and acute states determines the number of reflex model iterations. Note: the rapid-computational model still uses the Runge-Kutta4 numerical ODE solver. The same process was repeated to fit and validate the physiologically detailed capacitance-controlled short-term reflex model.

For both physiologically detailed short-term reflex models, we ran a Monte Carlo uniqueness analysis to test the uniqueness of the fitted solution. The fitted parameters were varied  $\pm 50\%$  300 times, and the fitting cost function value was recorded.

### 2.2.4 *Constructing the Phenomenological Short-Term Reflex Model*

#### 2.2.4.1 Adapting SBV and $R_{as}$

SBV and  $R_{as}$  are adapted to maintain a homeostatic CO and MAP using a similar mechanism as Rondanina and Bovendeerd [30]. A decrease in  $R_{as}$  causes an increase in stroke volume; thus, to compensate for a drop in CO,  $R_{as}$  can be decreased to bring CO back up (**Equation. 2.11**). Changes in MAP are inversely related to SBV because a drop in SBV can be compensated for an increase in MAP (**Equation. 2.12**):

$$\frac{1}{R_{as}} \frac{d(R_{as})}{dt} = S_{CO}, S_{CO} = \frac{CO - CO_{hom}}{CO_{hom}} * \lambda_1 e^{-\lambda_2 t * \frac{CO - CO_{hom}}{CO_{hom}}} \quad \text{Equation 2.11}$$

$$\frac{1}{SBV} \frac{d(SBV)}{dt} = -S_{MAP}, S_{MAP} = \frac{MAP - MAP_{hom}}{MAP_{hom}} * \lambda_3 e^{-\lambda_4 t * \frac{MAP - MAP_{hom}}{MAP_{hom}}} \quad \text{Equation 2.12}$$

where  $CO_{hom}$  and  $MAP_{hom}$  are the homeostatic setpoints for CO and MAP, respectively. For short-term reflexes, the homeostatic setpoints are kept at their baseline values. To prevent massive changes in SBV and  $R_{as}$  that could cause the rapid-computational model to crash, the maximum change in SBV and  $R_{as}$  allowed was  $\pm 75\%$  and  $\pm 250\%$ , respectively.

We assume that the body's reflex system will try to drive CO and MAP back to baseline immediately after an intervention but concede that the body may fail to do so because the intervention is too drastic. Furthermore, multiple studies have shown that baroreceptor activity decreases with sustained increased arterial pressure [34], [42]. Baroreceptors have a direct influence on MAP directly and CO indirectly; thus, we added an exponential decay gradually term that turns off the baroreceptor response after continued activation at high increased pressure. This is an indirect method of the system reaching a new homeostatic setpoint using the baroreflex.  $\lambda_1$  and  $\lambda_3$  control the magnitude of baroreceptor deactivation while  $\lambda_2$  and  $\lambda_4$  control the rate at which the baroreceptors decay. The decay rate is proportional to the change in either CO or MAP [34]. The entire phenomenological short-term reflex model is described by **Equation 2.11** and **2.12**.

#### 2.2.4.2 Phenomenological Short-Term Reflex Model Fitting and Validation

We fitted  $\lambda_4$ , the decay rate constant for MAP (**Equation 2.11**), to match canine experimental baroreceptor activity from Chapleau et al. [44] for a step pressure increase from 40mmHg to 90mmHg. The *fminsearch* optimization algorithm in MATLAB 2021b was used to fit  $\lambda_4$ .

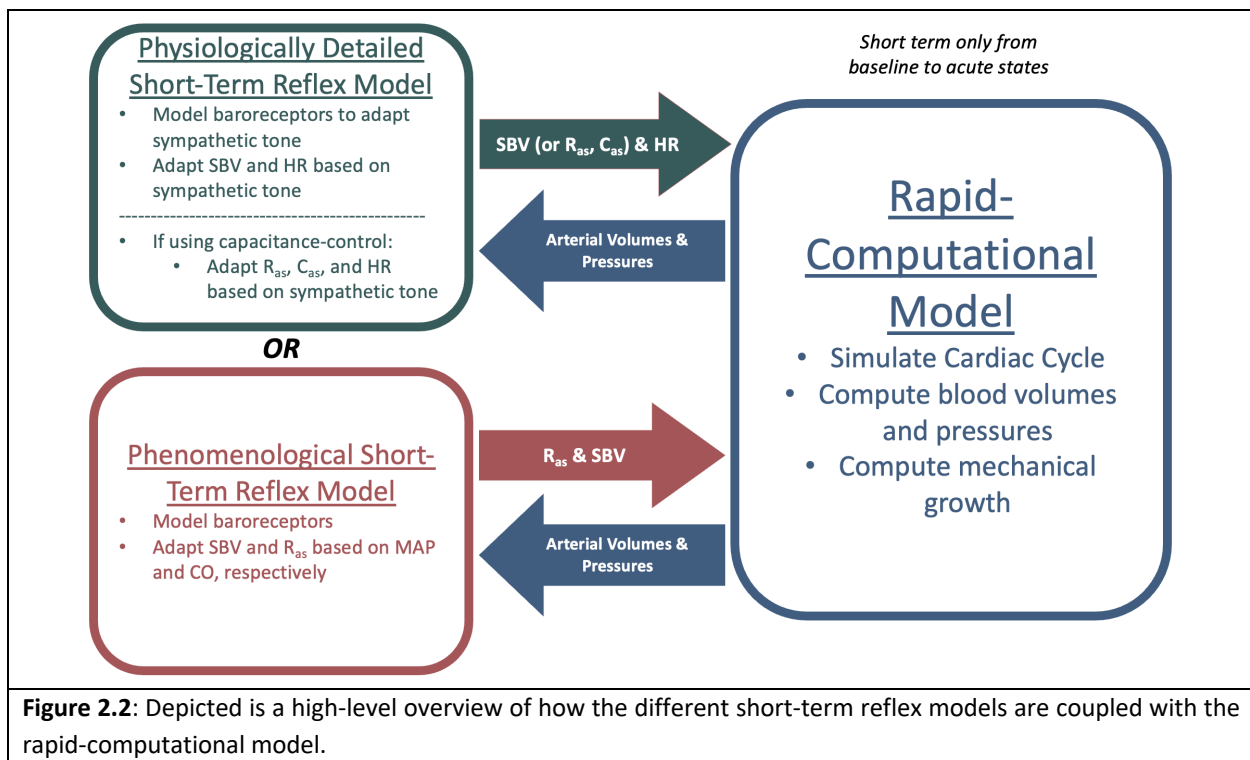
To our knowledge, the hemodynamic short-term reflex response mechanism for pressure and volume overload should physiologically be the same; as a result, we simultaneously matched canine experimental data for both types of overloads to fit  $\lambda_1$ ,  $\lambda_2$ , and  $\lambda_3$ . We matched EDV, ESV, MaxP, EDP, MAP, MinV, and RF from Sasayama et al. and Kleaveland et al. (**Appendix C Equation C.1**) [8], [9]. We simulated 30 minutes of post-intervention hemodynamic reflexes with a time step ( $dt$ ) of 2 minutes. Like before, the reflex system of ODEs was solved without a numerical solver because  $dt$  is known at each iteration. The rapid-computational model is run at its baseline state, and then either aortic constriction or MR is induced by increasing  $R_{cs}$  or decreasing MVBR, respectively. Then the phenomenological short-term reflex model was run to compute the acute state SBV and  $R_{as}$ , and was fitted using the *fmincon* optimization algorithm, with a non-negativity

constraint, in MATLAB 2021b [45]. The phenomenological short-term reflex model was then validated against an independent canine volume overload study by Nakano et al. [10].

To check the uniqueness of the fitted solution, we ran a Monte Carlo uniqueness analysis where  $\lambda_1$ ,  $\lambda_2$ , and  $\lambda_3$  were each randomly varied  $\pm 50\%$ . The phenomenological short-term reflex model was run at each variation and the cost function (**Appendix C Equation C.1**) value was recorded.

### 2.2.5 Overview of 3 Different Short-Term Reflex Models

**Figure 2.2** summarizes the 3 different short-term reflex models and how they interact with the rapid-computational model.



## 2.3 RESULTS

### 2.3.1 Physiologically Detailed Short-Term Reflex Model Results

The LV pressure-volume (PV) loops from the pressure overload fitting simulation are shown in **Figure 2.3A**. The fitted parameters (**Appendix Table B.1**) were then used in the validation study as shown in **Figure 2.3B**. The simulations were run with and without the reflex model. In both the fitting and validations, the results suggest that when no reflexes are used, experimental systolic and diastolic pressures were not matched. Using the reflex model, we

matched experimental LV pressure and volumes. Since this was a pressure overload study, we expect to see an increase in ESP and ESV from baseline to acute which is only apparent when the reflex system is used. The results suggest that the physiologically detailed short-term reflex model can adapt SBV and HR to match the pressure overload acute state.

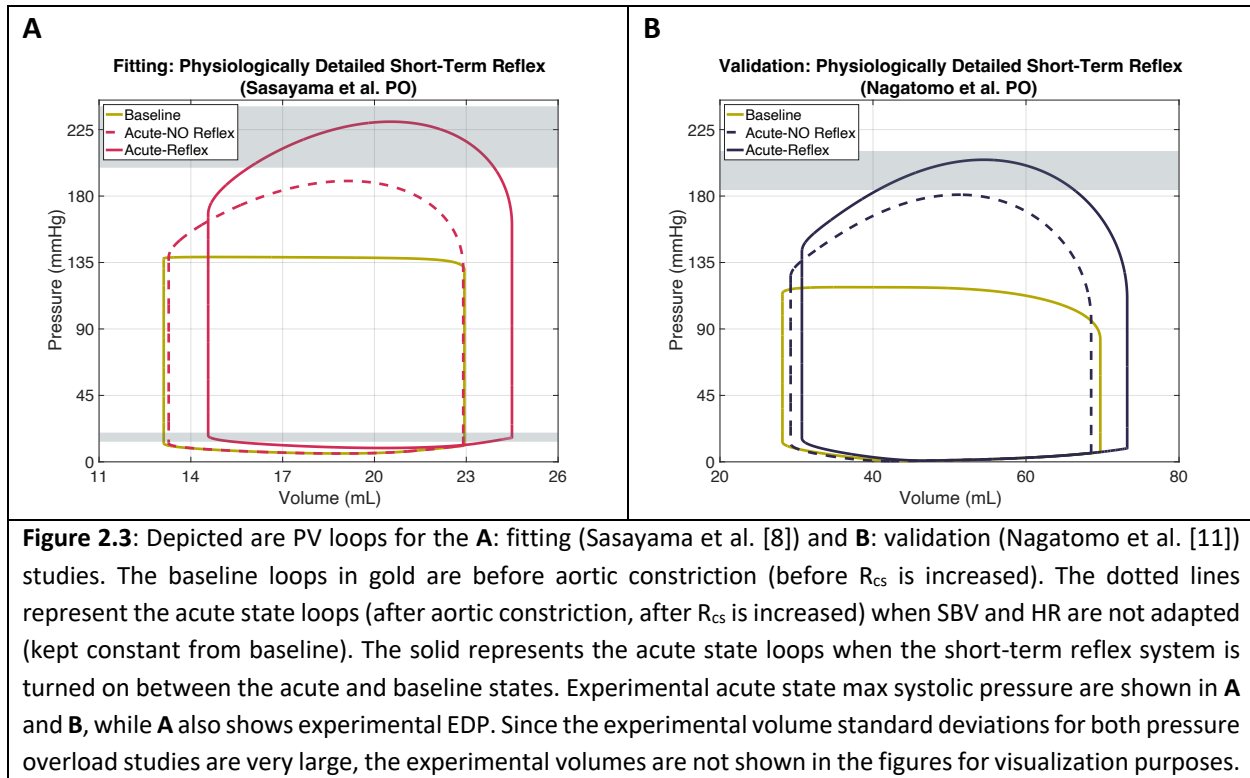
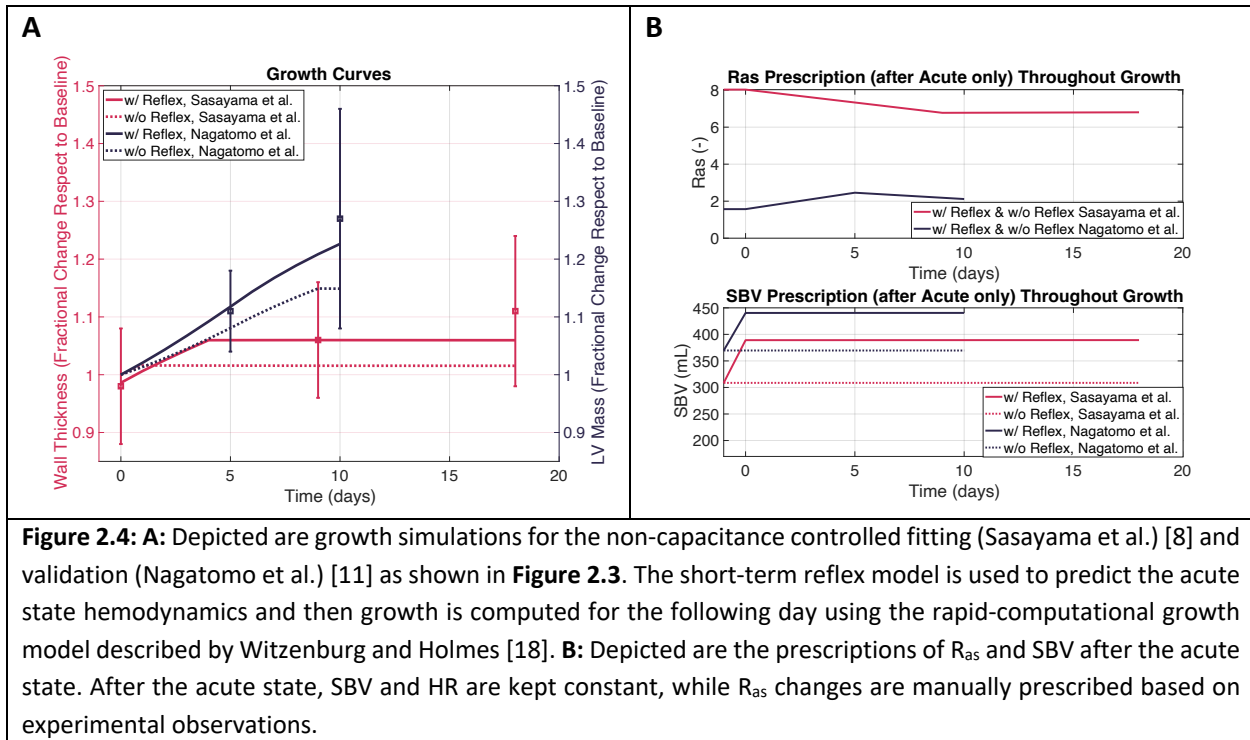


**Figure 2.4A** shows the growth curves for what happens when we use the physiologically detailed short-term reflex model to compute acute state hemodynamics, and then calculate growth 10-18 days later (chronic state) using the rapid-computational model. Since the physiologically detailed short-term reflex can only predict hemodynamic changes from the baseline to acute states, we manually prescribed hemodynamics ( $R_{as}$  and SBV) changes after the acute state until the chronic state.  $R_{as}$  and SBV are prescribed after the acute state the same way Witzenburg and Holmes originally prescribed them to compute growth (**Figure 2.4B**) [18]. When we do not predict the hemodynamic changes from baseline to acute state (without reflexes), then even when manually prescribing hemodynamics after the acute state, we cannot match the experimental mean changes in growth as well as we can when predicting the baseline to acute hemodynamic changes (with reflexes). **Figure 2.4** highlights that hemodynamic changes from baseline to acute are very important for computing long-term growth.



We also tried to run the physiologically detailed short-term reflex model for volume overload simulations; however, the model was not able to converge to a solution. Model parameter perturbations always resulted in the rapid-computational model crashing due to large changes in SBV and HR. As a result, the Runge-Kutta4 ODE solver in the rapid-computational model would crash due to extremely small, even negative, or large LV volumes, and we were not able to obtain a solution.

Figure 2.5 shows the uniqueness test for the fitted solution to the Sasayama et al. pressure overload study when using the physiologically detailed short-term reflex model. It is evident that we did not obtain a unique solution. When we vary the parameter values, we obtained similar solutions especially when the parameter distance is far away from the fitted solution.

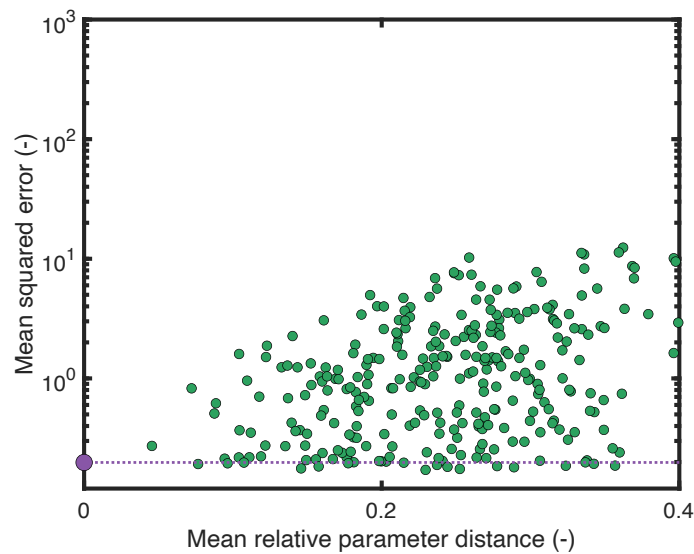


**Figure 2.5: A:** Monte Carlo parameter uniqueness analysis for the Sasayama et al. pressure overload as shown in **Figure 2.3A**. The fitted parameters in **Appendix Table B.1** were randomly varied  $\pm 0$ -50% 300 times. Each time the parameters were varied, the short-term reflex model was run and the error from **Appendix B Equation B.1** was recorded. Data is plotted on a log y-scale and the x-axis displays the mean relative parameter distance to the optimal fitted solution. The purple dot is the fitted simulation, and each green dot is a parameter varied simulation.

### 2.3.2 Physiologically Detailed Capacitance-Controlled Short-Term Reflex Model

Next, we ran a version of the physiologically detailed short-term reflex model using capacitance-control as described in section 2.2.3.3. In this version,  $C_{as}$  and  $R_{as}$  are adapted based on sympathetic tone (determined by the baroreflex), while SBV is not adapted (**Equation 2.8** is not used). The PV loop results for volume overload are shown in **Figure 2.6**. Note: volume overload study from Nakano et al. was used for fitting the volume overload case using the **Appendix B Equation B.3** cost function [10]. We were not able to obtain a converged solution for the pressure overload because the model would crash due to negative LV volumes during fitting. In addition, we tried to run an independent volume overload simulation using the Kleaveland et al. study; however, the model would crash due to negative LV volumes. Although we were able to fit the physiologically detailed capacitance-controlled short-term reflex model to the Nakano et al. volume overload study, the acute state when using the reflex model versus not using the reflex are not any better. We got closer to matching EDP using the reflex model, but we were no longer able to match peak end systolic LV pressure (**Figure 2.6**).

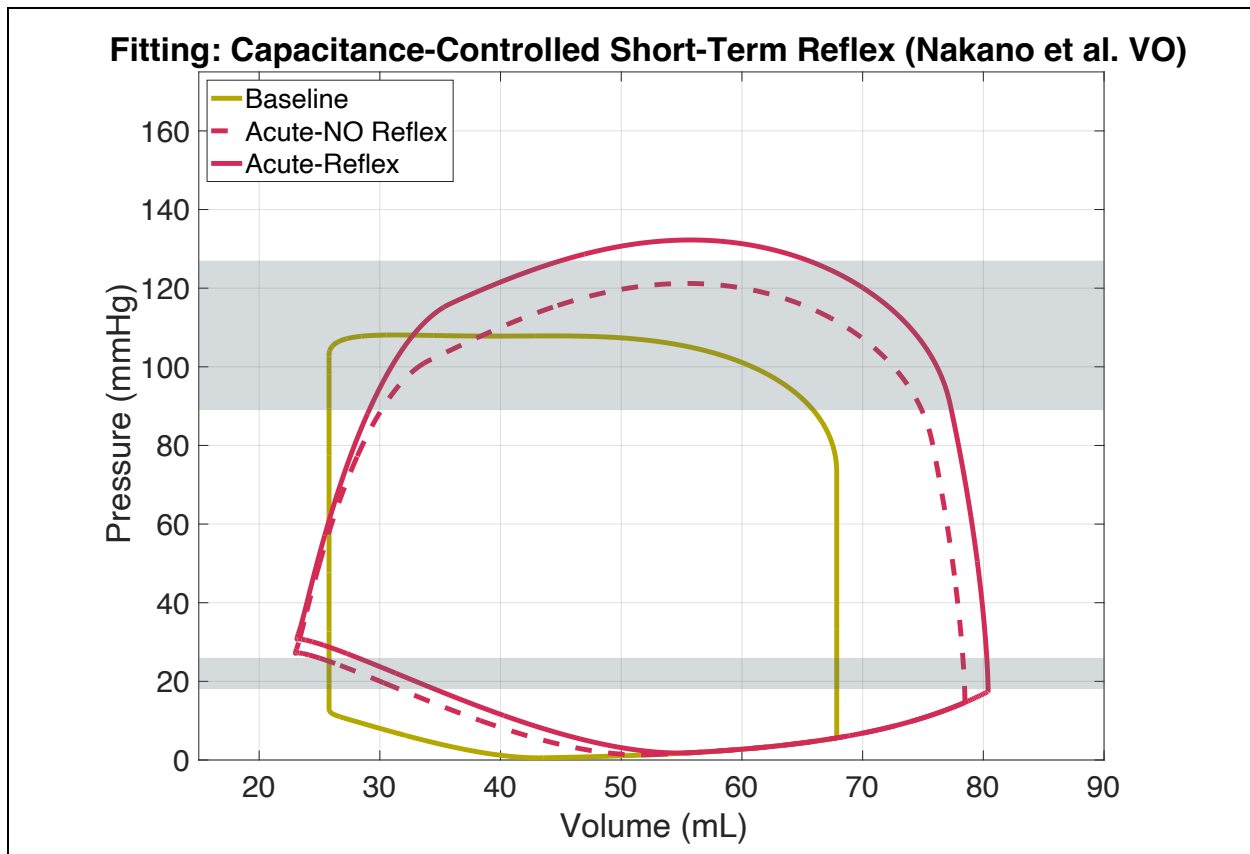


**Figure 2.6:** Depicted are PV loops for the capacitance controlled short-term reflex system fitted to Nakano et al. [10]. The dotted lines represent the acute state loops (after MR, after MVBR is decreased) when  $R_{as}$  and  $C_{as}$  are not adapted (kept constant from baseline). The solid represents the acute state loops when the short-term reflex system is turned on between the acute and baseline states. Experimental acute state EDP and max systolic pressure are shown in shaded gray regions. Since the experimental volume standard deviations are very large, the experimental volumes are not shown in the figures for visualization purposes.

**Figure 2.7** shows the uniqueness test for the fitted solution to the Nakano et al. volume overload study when using the physiologically detailed capacitance-controlled short-term reflex model. It is evident that we did not obtain a unique solution. When we vary the parameter values, we observed several similar solutions with different parameter values.

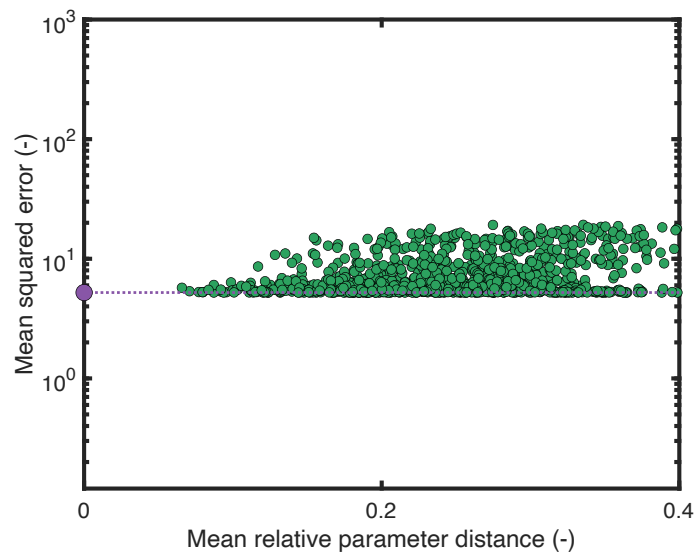


**Figure 2.7:** Depicted is a Monte Carlo sensitivity analysis simulation for the Nakano et al. Volume Overload simulation with capacitance control shown in **Figure 2.6**. The fitted parameters in **Appendix Table B.1** were randomly varied  $\pm 0$ -50% 1000 times. Each time the parameters were varied, the short-term reflex model was run and the error from **Appendix B Equation B.3**) was recorded. The purple dot is the fitted simulation, and each green dot is a parameter varied simulation. Data is plotted on a log y-scale and the x-axis displays the mean relative parameter distance to the optimal fitted solution. The purple dot is the fitted simulation, and each green dot is a parameter varied simulation.

### 2.3.3 Phenomenological Short-Term Reflex Model Results

Our third short-term reflex modeling approach was to use a phenomenological short-term reflex model as described in section 2.2.4. We first fitted part of the phenomenological short-term reflex model to match decay in baroreceptor activity. **Figure 2.8** shows the baroreceptor response of the phenomenological short-term reflex system fitted against experimental baroreceptor activity at an elevated pressure. The decay constant in **Equation 2.12** can capture the decrease in baroreceptor activity during elevated MAP, which is often seen in between the baseline and acute states of pressure and volume overload due to the sudden intervention. The optimal value for  $\lambda_4$  is shown in **Appendix C Table C.1**.

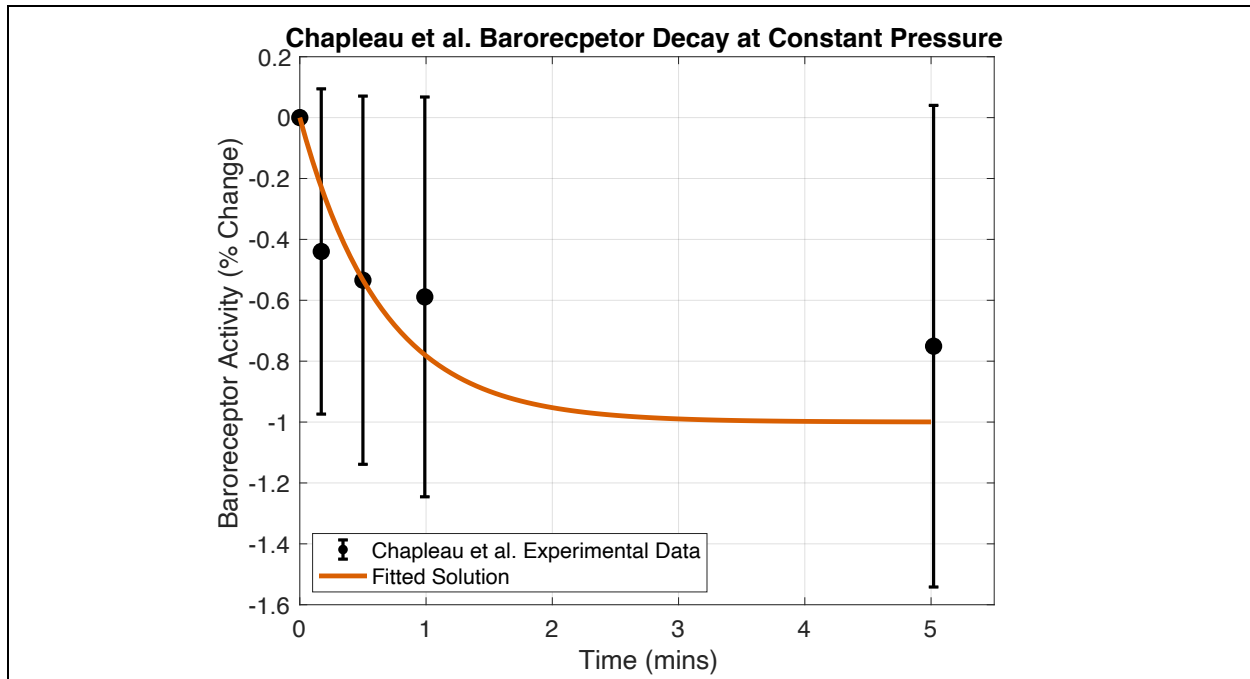


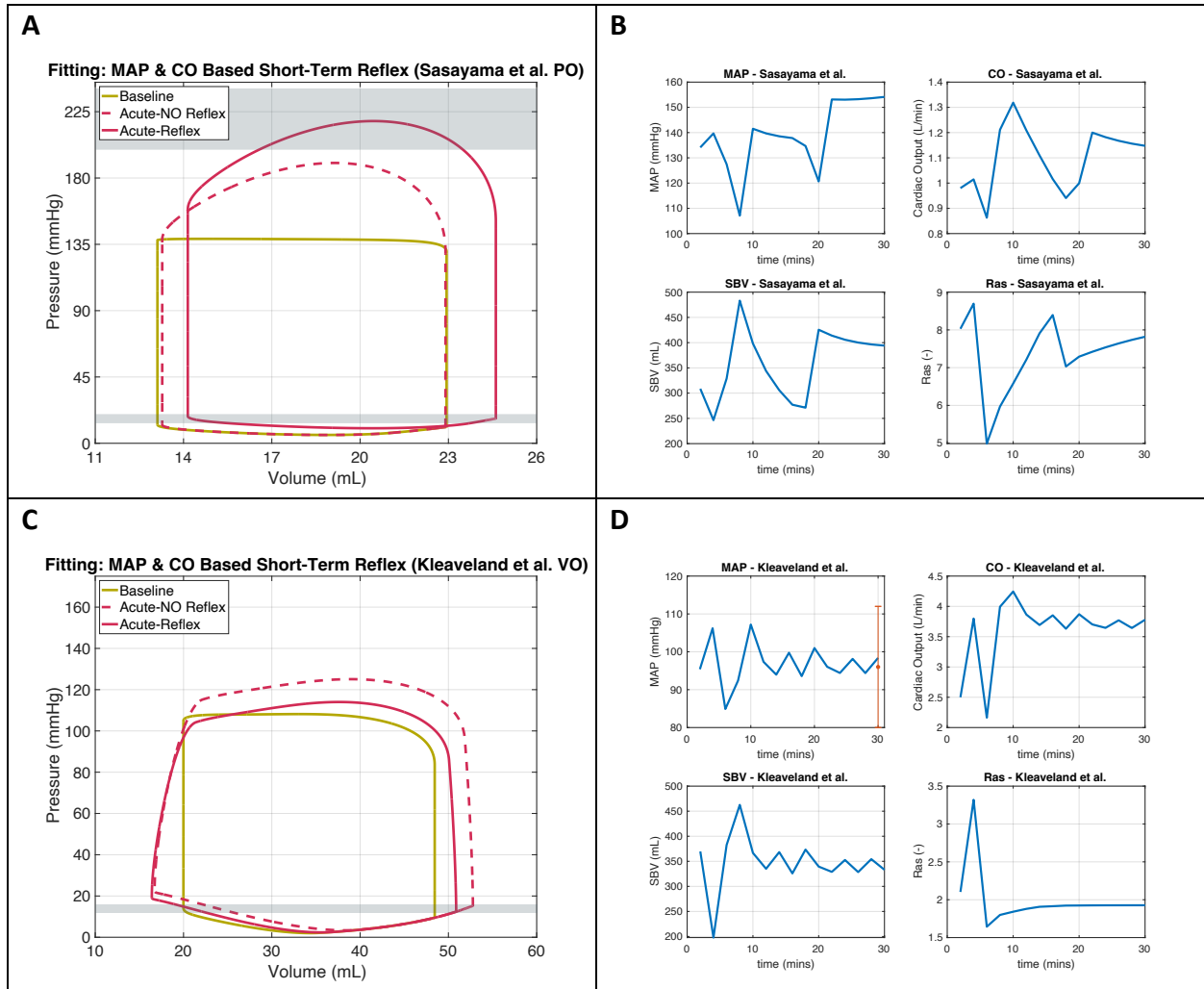
**Figure 2.8:** Depicted in orange is **Equation 2.12** where  $\lambda_3$  and  $\lambda_4$  are fitted to match the experimental data from Chapleau et al. shown in blue [34]. MAP was elevated from 40 mmHg to 90 mmHg right after time zero and kept constant at 90 mmHg for the entire simulation. Note: **Equation 2.12** was shifted down by 1 to ensure the output started at zero.  $\lambda_3$  was only fitted to provide a magnitude for fitting  $\lambda_4$ .  $\lambda_3$  results from this simulation were not used subsequently in the short-term reflex model.

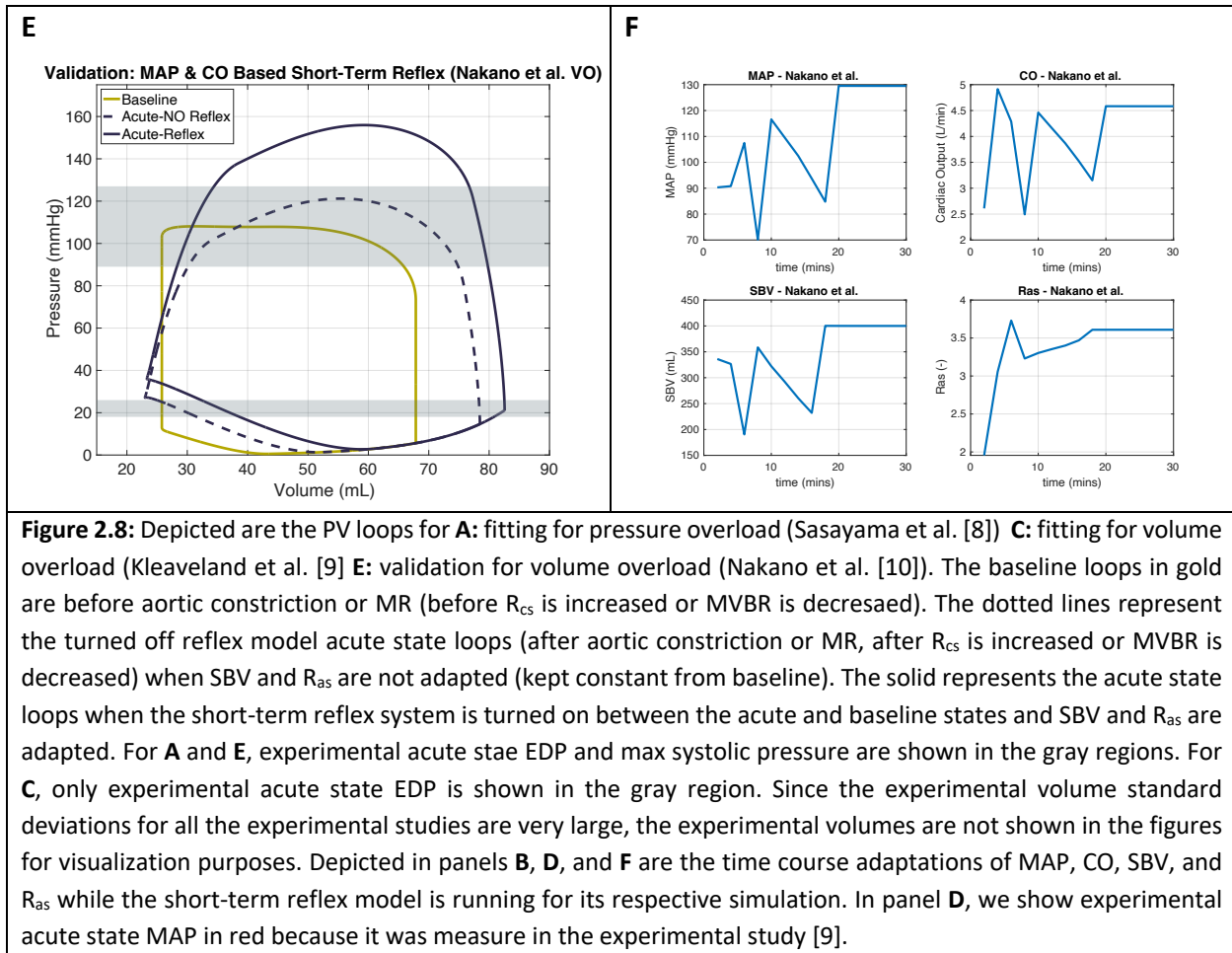
The PV loops from the pressure [8] and volume [9] overload fitting simulation are shown in **Figure 2.8A, C**. The fitted parameters of **Equation 2.11** and **Equation 2.12**, shown in the green column of **Appendix Table C.1**, were then used in the independent validation study as shown in **Figure 2.8E**. The simulations were run with and without the reflex model to highlight the importance of hemodynamic predictions. In the Sasayama et al. pressure overload fit (**Figure 2.8A**), we were only able to match the experiment EDP and peak systolic LV pressure when using the phenomenological reflex model. In the same fitting study with Kleaveland et al. volume overload, we were still able to match the experimental EDP; although, it is evident that the reflex and no reflex PV loops are fairly similar in this study. In the Nakano et al. validation, we did not match the experimental pressures as well as we would've liked to (**Figure 2.8E**). It is evident that the with the phenomenological short-term reflex model, we were able to match EDP; however, we overshoot the peak systolic LV pressure.

In addition to the PV loops shown, the adaptive stimuli (MAP and CO) and adapted parameters (SBV and  $R_{as}$ ) from the short-term reflex model are shown in **Figure 2.7B, D, F**. We knew experimental acute state MAP for the Kleaveland et al. study, and the phenomenological short-term reflex model was able to match the acute state MAP (**Figure 2.8D**). These figure panels show that in each case, the model reached almost steady state stimuli values at the 30-minute time point. Since we observed some oscillations in SBV and  $R_{as}$ , we ran the simulations for an

additional 50 minutes to verify that there was no change in the hemodynamic predictions, and we observed no change.

To verify the uniqueness of the solution, we ran a Monte Carlo uniqueness analysis, and the results are displayed in **Figure 2.9**. The analysis suggests that the fitted solution is unique because no other parameter variation results in the same cost function value.





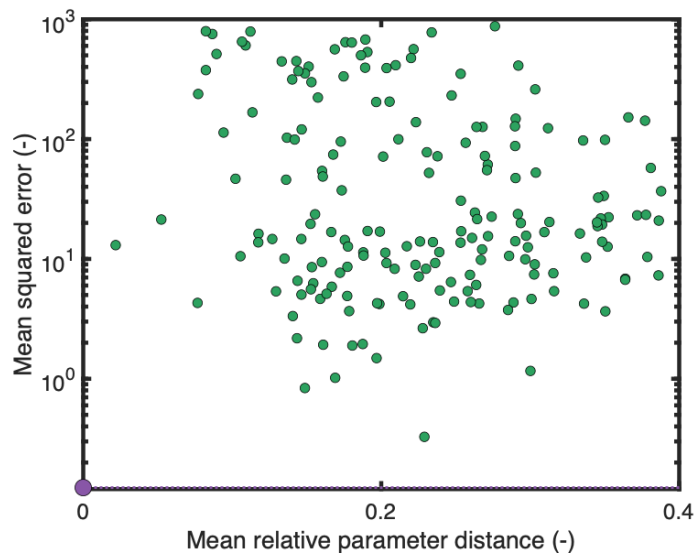


**Figure 2.9:** Depicted is a Monte Carlo uniqueness analysis for the fitted Sasayama et al. and Kleaveland et al. pressure and volume overload simulations shown in **Figure 2.8**. The fitted parameters in **Appendix Table C.1** ( $\lambda_1$ ,  $\lambda_2$ , and  $\lambda_3$ ) were randomly varied  $\pm 0-50\%$  500 times. Each time the parameters were varied, the phenomenological short-term reflex model was run and the error from **Appendix C Equation C.1** was recorded. Data is displayed on a log y-scale and the x-axis displays the mean relative parameter distance to the optimal fitted solution. The purple dot is the fitted simulation, and each green dot is a parameter varied simulation.

## 2.4 DISCUSSION

The goal of this chapter was to develop a hemodynamic model that can predict the hemodynamic changes immediately following an intervention that causes pressure or volume overload in canines. **Figure 2.4** highlights the importance short-term hemodynamics play, supporting the findings of Witzenburg and Holmes [18]. We were not able to develop a short-term reflex model that predicted hemodynamics changes and matched experimental data for all pressure and volume overload cases; however, each type of short-term reflex model developed has unique characteristics that allow it accurately to predict the acute state in different cases.

The physiologically detailed short-term reflex model can predict hemodynamic changes necessary to compute growth for pressure overload only, and this version of the model was successfully validated against an independent pressure overload study (**Figure 2.3**). The physiologically detailed capacitance-controlled short-term reflex model was only able to predict hemodynamic changes in one volume overload study (**Figure 2.6**), and we could not validate this model with an independent study. Using the two physiologically detailed short-term reflex models, we can capture the hemodynamic changes in pressure and volume overload; however, we were not able to support the use of different constriction mechanisms for hemodynamic reflexes in pressure versus volume overload from the literature. The reflex responding system should be the same in pressure and volume overload. The phenomenological short-term reflex

model predicted hemodynamic changes in both a pressure and volume using the same set of parameters; however, we were not able to fully validate the model against an independent study (**Figure 2.8**).

For the physiologically detailed short-term reflex model, several assumptions were made that may also have contributed to difficulty fitting both pressure and volume overload simulations with the same reflex system. Baroreceptors are mechanically sensitive and respond to changes in aortic stretch. Beard et al. modeled aortic mechanics to compute aortic stretches; however, the rapid-computational model does not have an aortic compartment. Consequently, we had to estimate aortic stretches based on arterial volumes (**Equation 2.1-2.3**) resulting in less accurate baroreceptor activity. In addition, adapting SBV was dependent on a maximal SBV and that were set based on the mechanics of an average blood vessel which may not be true throughout the vasculature.

For the physiologically detailed capacitance controlled short-term reflex model, we only adapted the arterial capacitances and resistances. However, much of the blood volume in the vasculature is on the venous side in our system: ~4.5% of the blood is in the systemic arteries and ~74% of the blood is in the systemic veins. Although the changes in systemic arterial capacitance were still large enough to match the acute state for the Nakano et al. study, adapting the venous capacitances using the relationship in **Equation 2.9** is worthwhile to explore because it may result in better acute state predictions for the volume and pressure overload studies we did not match.

A major challenge of coupling the physiologically detailed short-term reflex model with the rapid-computational model was working with two different time scales. Beard et al. originally computed baroreceptor activity during each cardiac cycle on the order of seconds [33]. The rapid-computational model is much more simplified in that it only computes one cardiac cycle for each baseline and acute state, and during growth, one cardiac cycle equals one day of growth. When constructing the physiologically detailed reflex model, we had to update baroreceptor activity only once per cardiac cycle to match the time scale of the rapid-computational model. Since baroreceptors respond to changes in arterial stretch very rapidly, we likely did not capture the true baroreceptor response in our physiologically detailed short-term reflex model.

The results from the two physiologically detailed reflex models helped motivate exploring and developing the phenomenological reflex model. A simplified hemodynamic model allowed us to ignore the difference in time scale because there was no longer a need to compute baroreceptor activity in real time.

For the phenomenological short-term reflex model, we were not able to validate it against the Nakano et al. volume overload study. Although we matched EDP, we did worse in matching peak systolic LV pressure compared when not using any reflexes. It is important to note that the goal of the rapid-computational model in volume overload studies is to compute LV growth. Growth during volume overload, eccentric growth, is driven by maximum fiber strain which occurs at end diastole [18]. In **Figure 2.8**, we see that when we use the phenomenological short-

term reflex model, we obtain larger strains at end diastole indicated by the larger EDV compared to when no reflexes are used. Thus, although we overshoot the peak systolic LV pressure, in terms of modeling eccentric growth, it is more important for us to match EDP and EDV as accurately as possible.

Prior to settling on a system of ODEs to describe the phenomenological short-term reflex system, several variations were explored. **Equation 2.11** and **2.12** both contain an exponential decay term to describe the decrease in baroreceptor activity when high MAP is sustained for extended periods of time [34]. We originally did not include the exponential decay terms, similar to how Rondanina and Bovendeerd control SBV and  $R_{as}$ ; however, this resulted in large magnitude changes in MAP and CO which led to the rapid-computational model crashing due to very low or high blood volumes. The exponential decay term allowed large magnitudes to be diminished much faster than without the decay term allowing us to reach a solution during fitting.

We showed that the phenomenological short-term reflex model solution fitted against Sasayama et al. and Kleaveland et al. pressure and volume overload studies can be partially validated against the Nakano et al. volume overload study. We previously showed that the rapid-computational model, without a reflex system where hemodynamics are manually prescribed, can be validated against the Nagatomo et al. pressure overload study [11]. We tried to validate our phenomenological short-term reflex model the against Nagatomo et al. pressure overload, but the model would often crash due to negative LV volumes and resistances. We also tried to fit against different combinations of the four aforementioned canine studies and validate against others; however, the best solution was obtained by fitting simultaneously to Kleaveland et al. and Sasayama et al. **Appendix Table C.2** shows the cost function errors for each of the fitting and validation combinations. During fitting, we restricted the domain of the fitting parameters to try to obtain a solution faster. When fitting to Nagatomo et al. or Nakano et al. the optimizer would often try to go past either the lower or upper to essentially make the change in SBV or  $R_{as}$  either 0 or extremely high (parameter values shown in **Appendix Table C.1**).

#### *2.4.1 Comparing the 3 Short-Term Reflex Models*

Part of our analysis included comparing the results between each of the 3 short-term reflex models. We used the physiologically detailed and phenomenological short-term reflex models to simulate pressure overload for the Sasayama et al. studies. We used the physiologically detailed capacitance-controlled and phenomenological short-term reflex models to simulate volume overload for the Nakano et al. studies. We decided to re-plot the results from **Figures 2.3A, 2.6, and 2.8E** so that we can see how the different short-term reflex models predicted the acute states (**Figure 2.10**). In addition, we overlaid the results from **Appendix A Figures A.1A and A.2B** to see how the reflex results compare to when we fitted the acute state by manually prescribing hemodynamics in the Sasayama et al. and Nakano et al. simulations.

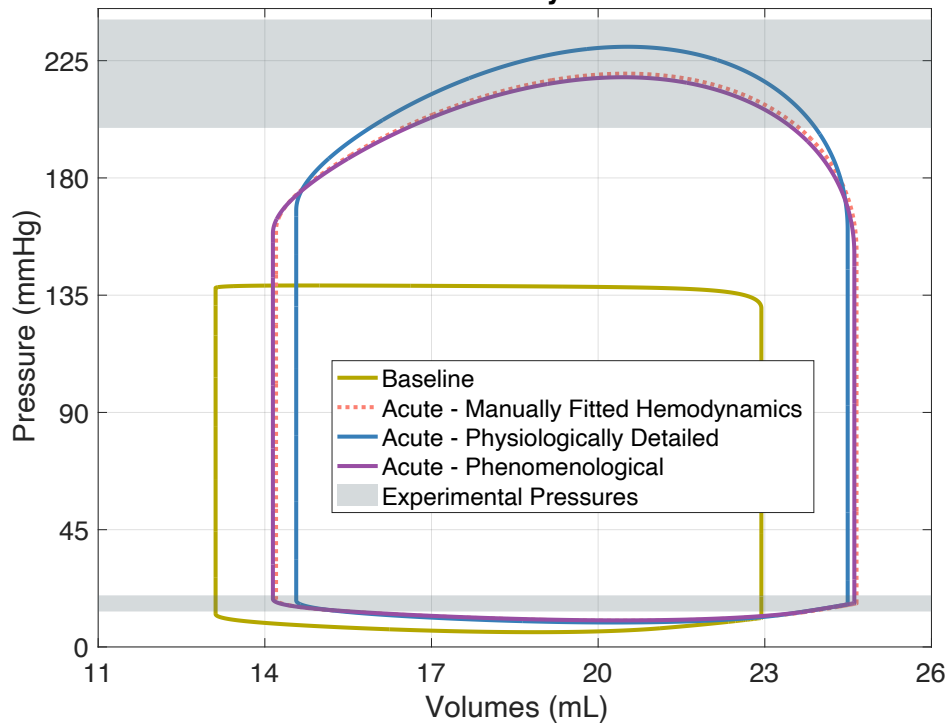
When simulating pressure overload for Sasayama et al., the physiologically detailed and phenomenological short-term reflex models perform similarly in predicting the acute state (**Figure 2.10A**). This suggests that we can capture the reflex responding system in the Sasayama et al. study using both a simplified and detailed model of the baroreceptors.

In the Nakano et al. volume overload study, we observed that the physiologically detailed capacitance-controlled and phenomenological short-term reflex models behave differently. The phenomenological model does better at matching EDP but performs worse than the capacitance-controlled model when trying to match peak systolic LV pressure. We also observed that both the short-term reflex models and the manually fitted hemodynamics version all overestimate peak LV systolic pressure. The phenomenological model does better than the capacitance-controlled model in predicting the same EDV as the manually fitted hemodynamics version. Since the overall goal is to still model LV growth, accurately predicting EDV and EDP is vital.

It is important to note that all 3 short-term reflex models were not verified and validated against experimental data in between the baseline and acute states. Our phenomenological short-term model predicts several oscillations, between the baseline and acute state, but we have no way of verifying this behavior. We also observed that it is difficult to predict HR changes from baseline to acute. We originally predicted HR with both the physiologically detailed model because we had success in doing so, but the experimental canine studies all reported that HR was controlled pharmacologically or electrically paced during the surgery [8]–[11]; thus, we may not have been capturing the true physiological reflex response to adapting HR. Exploratory analysis of the rapid-computational model suggests that the system is sensitive to HR changes; as a result, future work should include trying to better calibrate the model using HR adaptations.

**A**

### Physiologically Detailed and Phenomenological Short-Term Reflex Models for Sasayama et al. Pressure Overload



**B**

### Physiologically Detailed Capacitance-Controlled and Phenomenological Short-Term Reflex Models for Nakano et al. Volume Overload

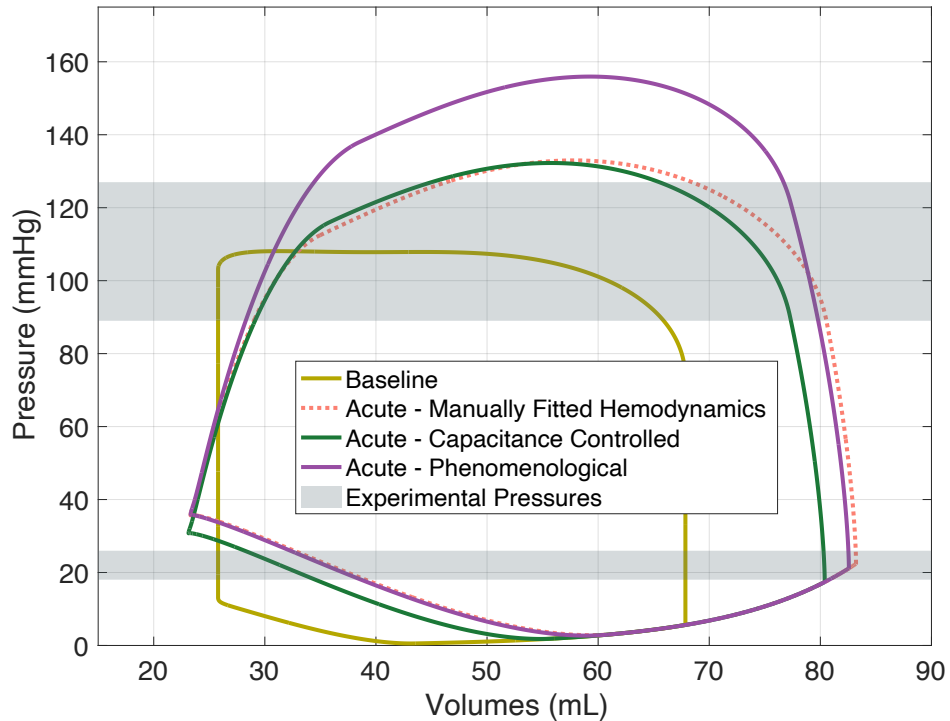


**Figure 2.10:** Depicted are the PV loops from **Figures 2.3A, 2.6, and 2.8E** overlayed on top of each other for Sasyama et al. pressure overload and Nakano et al. volume overload. In both panels, the dotted red loop represents the acute state PV loops from **Appendix A Figures A.1A and A.2B** when we fitted the acute state by manually prescribed hemodynamics. This was the original method used by Witzenburg and Holmes [18] to model the acute state. In both panels, experimental peak systolic LV pressures and EDP mean  $\pm$  1 standard deviation are shown by the gray rectangles. Note: as stated in section 2.3, the physiologically detailed short-term reflex model was not able to simulate the Nakano et al. study. The capacitance-controlled short-term reflex model was not able to simulate the Sasayama et al. study.

We concluded from the Chapter 2 results that we did not develop a short-term reflex model that can accurately predict the acute state hemodynamics in all four 4 canine studies used by Witzenburg and Holmes to fit and validate the rapid-computational model. However, we do show how different levels of physiological detailed in modeling the baroreceptors affects predicting the acute state. The phenomenological short-term reflex model did the best out of the three short-term reflex models in predicting both pressure and volume overload using the same set of parameters. In Chapters 3 and 4, we construct a long-term reflex model and model LV growth in humans, respectively. In both those chapters, we use the phenomenological short-term reflex model for predicting changes in hemodynamics from baseline to acute.

## 3 CHAPTER 3: LONG-TERM REFLEX SYSTEM

### 3.1 INTRODUCTION

In Chapter 2, we explored different approaches to modeling the short-term, baroreceptor-driven hemodynamics responses that occur immediately following the onset of pressure or volume overload. Several studies have shown that hemodynamic adaptations employ different physiologic systems depending on the time scale [33], [39], [46]. In **Figure 2.4**, we had to manually prescribed hemodynamic changes after the acute state to accurately predict long-term LV growth. Rather than manually prescribing hemodynamics, we would like to develop a long-term reflex system to predict hemodynamics on the order of days to months after the acute state.

During long-term hemodynamic adaptation, the renin-angiotensin system plays a key role in regulating blood volumes throughout the body, while quick short-term baroreflexes play a diminished role [33], [39]. The baroreflex system adapts within a couple of hours after a circulatory intervention. This adaptation is known as baroreceptor resetting [46], [47]. After the baroreceptors reset, blood volume becomes the primary regulator of MAP. Blood volume is determined by the kidneys, where arterial pressure and output of salt and water are inversely related on the order of hours to days [48]. When MAP gets too high, blood volumes drop because the kidneys excrete water and salt; conversely, the kidneys retain water and salt when MAP is too low which drives back MAP to normal [39]. On the hormonal scale, renin is released from the kidneys when there is decreased blood volumes and/or decreased MAP. Renin cleaves angiotensin to angiotensin I which downstream is converted to angiotensin-II which is the hormone responsible for vasoconstriction [37].

In addition, during long-term hemodynamic adaptation, CO starts to play a smaller role in the regulation of total peripheral resistance. Tissues tend autoregulate blood flow based on local tissue demands. We have seen that total peripheral resistance, analogous to  $R_{as}$ , responds quickly to change in CO during an acute change; however, over time, tissue autoregulation is used to control local vasculature and total peripheral resistance changes only make a small contribution towards bringing back CO to normal [39]. During an acute circulatory change, local blood flow is controlled by constricting or dilating blood vessels nearby; however, over the course of weeks, structural changes in the blood vessels return the local blood flow towards normal [49], [50].

Because cardiac growth models aim to capture changes that occur over weeks or months, capturing long-term regulation of blood volumes will be important in properly accounting for changes in loading of the ventricle. Due to the limited availability of cardiac hypertrophy data sets, information about salt-water balances and angiotensin-II activity is sparse in LV pressure and volume overload experiments. Consequently, similar to the phenomenological short-term

reflex system, we constructed a phenomenological long-term hemodynamic reflex system that predicts blood volume changes based directly on MAP. In this chapter, we construct and validate a long-term reflex model coupled to the rapid-computational model to regulate SBV based on MAP during chronic pressure and volume overload.

## 3.2 METHODS

### 3.2.1 Adapting Long-Term SBV

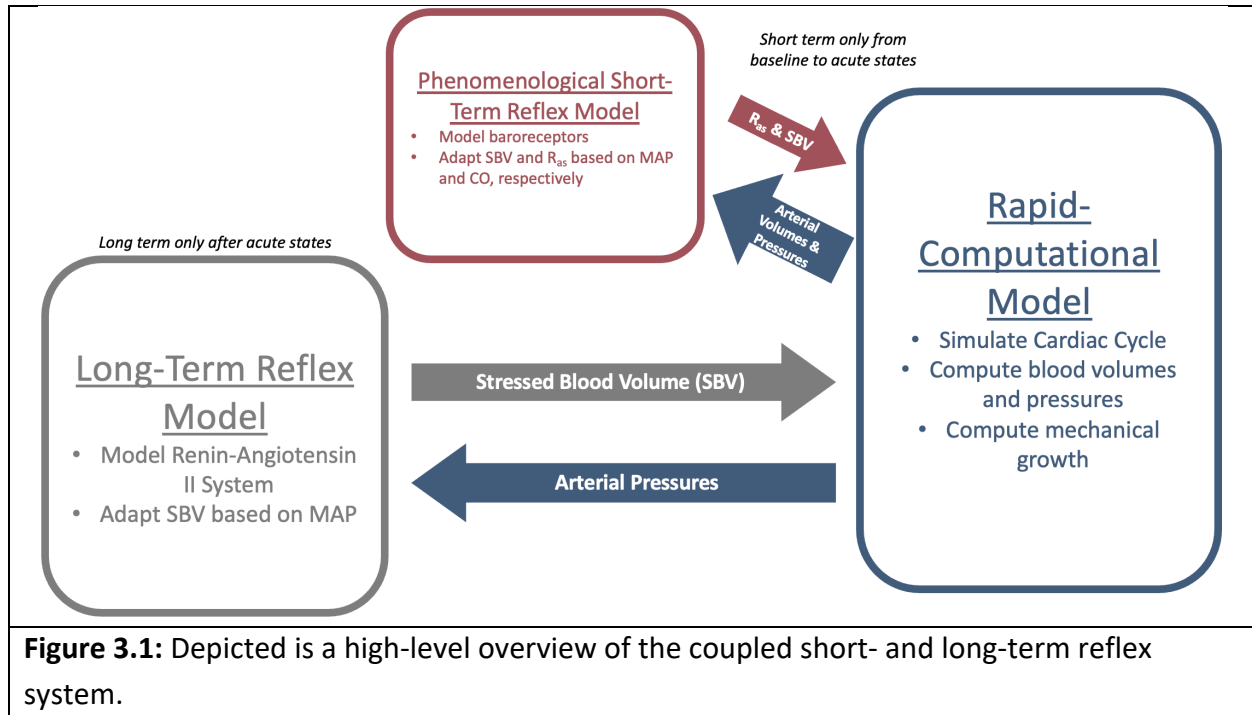
To mimic the kidney's regulation of blood volumes using salt and water levels, we adapt SBV to simulate changes in blood volume. We relate MAP and SBV below in **Equation 3.1**:

$$\frac{1}{SBV} \frac{d(SBV)}{dt} = \frac{S_{MAP}}{\tau_{kidney}}, S_{MAP} = \frac{MAP - \overline{MAP}_{hom}}{\overline{MAP}_{hom}} \quad \text{Equation 3.1}$$

where  $\tau_{kidney}$  is the kidney reflex time constant, and  $\overline{MAP}_{hom}$  is a moving average MAP homeostatic setpoint. The moving average was computed as the mean of the MAP values for the past  $n$  time steps where  $n$  is a customizable time window length. Guyton showed that in a volume loading hypertension experiment, MAP approached a new setpoint that was different from baseline. They concluded that when the heart is strong enough, it will adapt to pump at higher arterial pressures to meet kidney demands [39]. Consequently, we implemented a moving average homeostatic MAP that adapts based on a tunable history timeframe. Guyton also showed that total peripheral resistance adapted independently of CO over the course of days in the same experiment [39]. As a result, we only model blood volume changes through SBV adaptation. The time constant  $\tau_{kidney}$  is a fitted parameter that controls the rate at which SBV is adapted.

### 3.2.2 Coupling the Short- and Long-term Reflex Systems

The long-term system is coupled to the phenomenological short-term system such that the baroreflexes (short-term reflex system) are turned on from baseline to acute, and then the short-term reflexes get turned off immediately after computing the acute state. The long-term reflexes then turn on from the acute state (after an intervention) until the chronic state (days to months after an intervention). The short-term reflex system is turned off after the acute state because the baroreceptors reset, and the kidney reflexes take over hemodynamic regulation. The coupled reflex model input-output diagram is shown in **Figure 3.1**.



### 3.2.3 Reflex System Fitting and Validation

The long-term reflex model parameter  $\tau_{kidney}$  was fitted simultaneously to the Kleaveland et al. and Sasayama et al. volume and pressure overload studies [8], [9]. We optimized  $\tau_{kidney}$  to match experimental EDV, ESV, EDP, MAP, minimum LV volume, and regurgitant fraction at day 9 and 18 of growth from Sasayama et al. and month 1 and 3 of growth from Kleaveland et al. as described in the **Appendix D Equation D.1** cost function. To fit the long-term reflex model, the coupled reflex model, shown in **Figure 3.1**, was run for the corresponding days of growth for each study: 18 days for Sasayama et al. and 90 days for Kleaveland et al. The short-term portion of the coupled reflex model uses the fitted parameters from the phenomenological short-reflex model in Chapter 2. After the acute state, the long-term reflex system was turned on and SBV was adapted. The moving average window length for  $\overline{MAP}_{nom}$  was set to 10, and the long-term reflex model was run for 5 iterations between each rapid-computational model run. During growth simulations in the rapid-computational model, each cardiac cycle (i.e., 1 rapid-computational model iteration) corresponds to one day of growth. As a result, since we run the long-term reflex model 5 times between each cardiac cycle, the time for each long-term reflex iteration is 0.2 day (4.8 hours). A  $\overline{MAP}_{nom}$  moving average window length of 10 is equivalent to 48 hours. Like before, the long-term reflex ODE was solved without a numerical solver because  $dt$  is known ( $dt$  was set to 1 which is equivalent to 4.8 hours).  $R_{as}$ ,  $R_{cs}$ , and LV elastance are kept constant throughout growth (after the acute state). HR was manually prescribed throughout the whole simulation based on experimental data. During the volume overload simulation, MVBR was manually prescribed throughout growth based on experimental data. Model was fitted using

the *fmincon* algorithm, with a non-negativity constraint in MATLAB2021b [45]. The reflex model was then validated against an independent canine volume overload study by Nakano et al. [10].

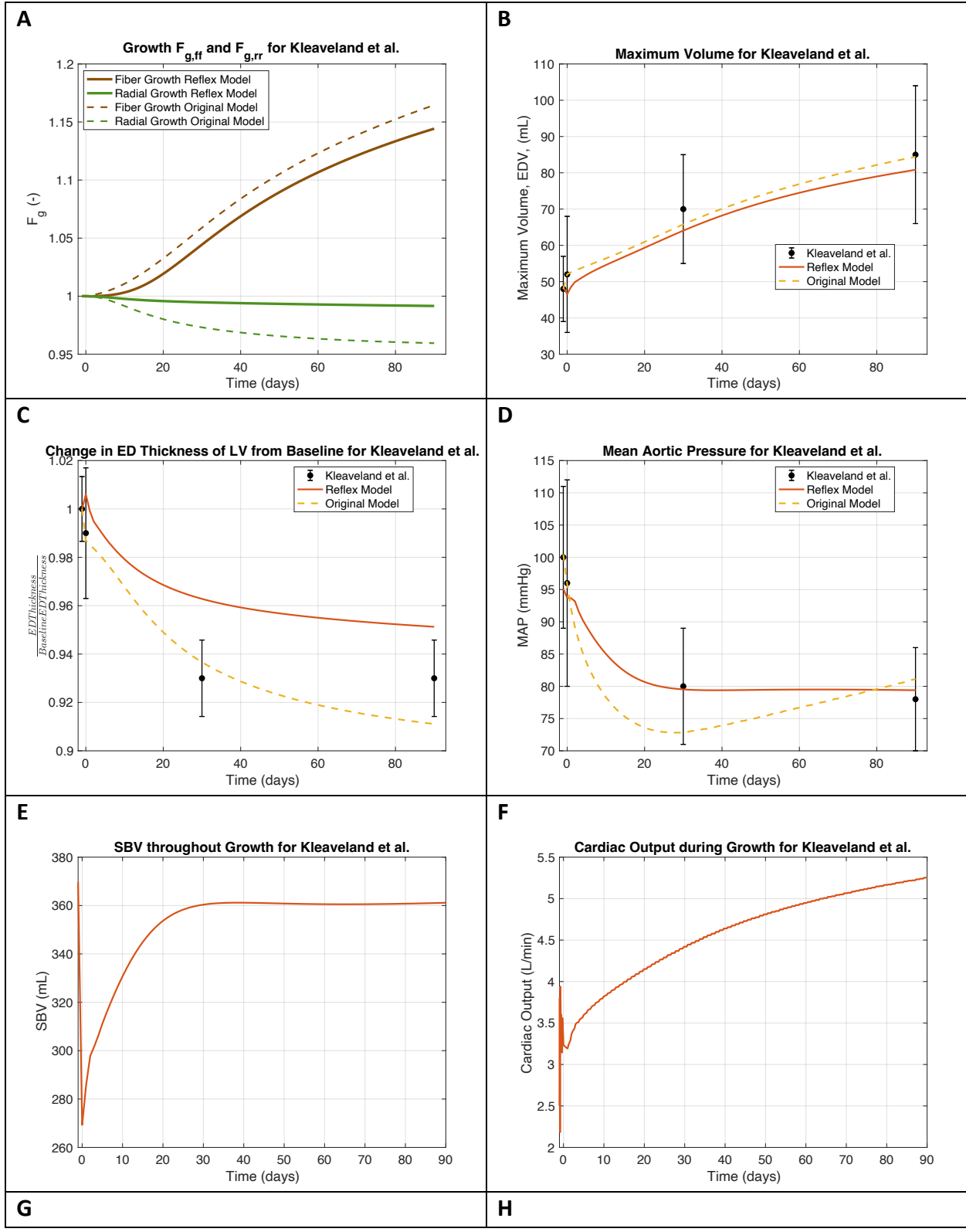
To check the uniqueness of the fitted solution, we ran a parameter sweep where  $\tau_{kidney}$  was varied from 1 to 20. The error (cost function value of **Appendix Equation D.1**) was recorded at each variation. We also tested the effect of the moving average window on the fitted solution by varying the  $\overline{MAP}_{hom}$  time window from 1 to 25 when  $\tau_{kidney}$  was kept at its fitted value.

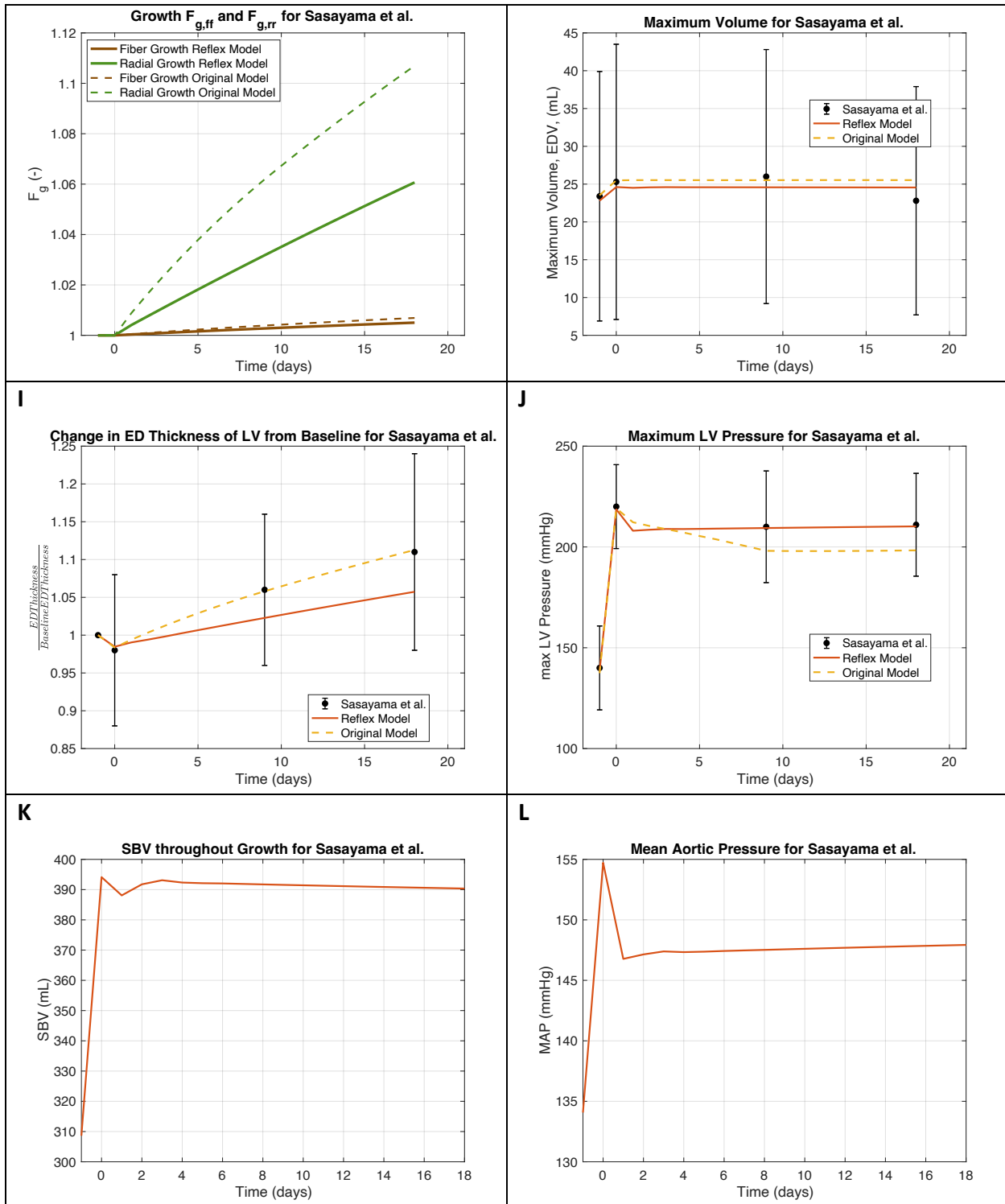
### 3.3 RESULTS

The fitting results are shown in **Figure 3.2**. We compared the chronic growth results to experimental data from the respective studies and the previously published growth results from using only the rapid-computational growth model (no reflexes). The optimal fitted solution was  $\tau_{kidney} = 4.7808 = 22.95$  hours. In the Kleaveland et al. volume overload study, we see that we were able to match maximum LV volume changes, suggesting good predictions of fiber growth. In the Sasayama et al. pressure overload study, we were able to match chronic changes in end-diastolic wall thicknesses (radial growth). Additionally, in the Kleaveland et al. volume overload study, we can see in **Figure 3.2D** that we are better able to match the chronic mean changes in aortic pressure compared to the original rapid-computational growth model suggesting that MAP is adapting to the correct homeostatic value. In the Kleaveland et al. volume overload study, a little bit of fiber growth was observed, and the results from **Figure 3.2A,C** suggest that we underestimate the change in end-diastolic wall thickening.

The independent validation results are shown in **Figure 3.3**. Although we underestimate the radial growth, we are still able to match the experimental results for Nakano et al. Similar to the original rapid-computational growth model, we are still not able to match the experimentally reported steady EDP (**Figure 3.3C**) and decrease in systolic arterial pressure (**Figure 3.3D**) during chronic growth. In the rapid-computational growth model, SBV and EDP are directly correlated. In the growth simulation with the reflex model, we see a gradual decrease in SBV which results in a decrease in EDP.

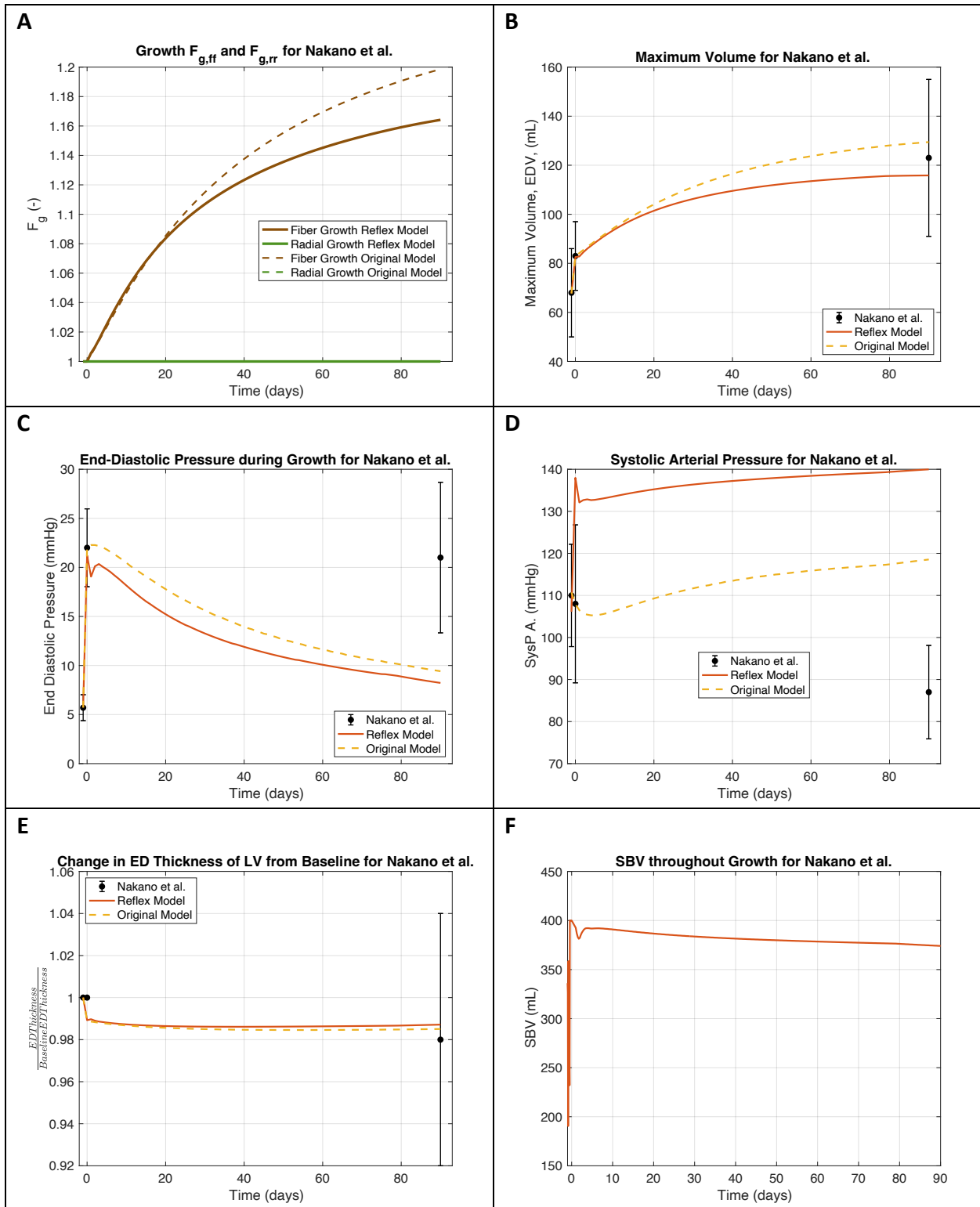
The parameter sweep for  $\tau_{kidney}$  shown in **Figure 3.4A** suggests that the solver found the optimal solution. From **Figure 3.4B** we see that  $\tau_{kidney}$  had very little effect on EDV, ESV, EDP, and maximum LV pressure for pressure overload; however, our ability to match experimental data (MAP, EDP, and minimum LV volume) during simulated volume overload was more sensitive to changes in  $\tau_{kidney}$ . In **Figure 3.5A**, we see the results for the homeostatic moving average window length. The best cost function (**Appendix D Equation D.1**) value is still at a window length of 10. During pressure overload only EDP at day 9 and 18 are most sensitive to the window length. During volume overload, MAP and minimum LV volume are most sensitive to the window length.





**Figure 3.2:** Depicted are the fitted reflex model simulations for Kleaveland et al. (A-E) and Sasayama et al. (G-L) volume and pressure overload, respectively. Original model results depicted by the dotted lines represent the from reparametrized rapid-computational reflex model from **Appendix Table A.1**. During the original model growth simulations, after the acute state hemodynamics were manually prescribed.  $R_{as}$ , MVBR (volume overload only), and LV elastance were manually prescribed. SBV and  $R_{cs}$  were kept constant. The reflex model results (described by **Figure 3.1**) are shown in the solid-colored lines where hemodynamics are computed during the

phenomenological short- and long-term reflex systems. Experimental results are depicted by the black error bars (mean  $\pm$  1 standard deviation). The baseline state is the time point before day 0 and the acute state is time point at day 0.  $F_{g,ff}$  is fiber growth and  $F_{g,rr}$  is radial growth.  $F_g$  is the growth tensor.



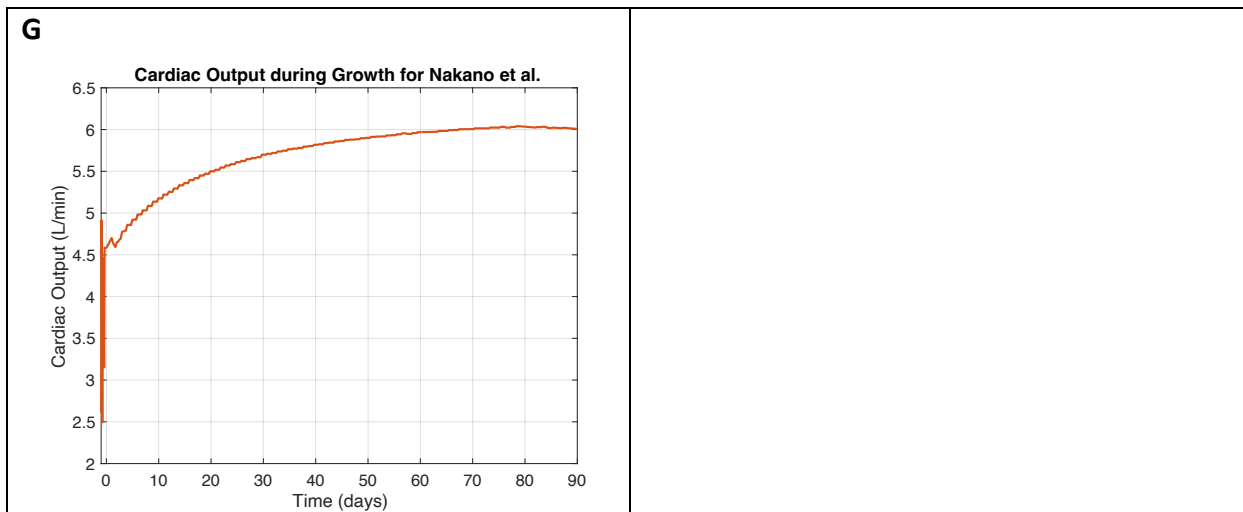


**Figure 3.3:** Depicted are the validation reflex model simulations for Nakano et al. **(A-G)** volume overload. Original model results depicted by the dotted lines represent the from reparametrized rapid-computational reflex model from **Appendix Table A.1**. During the original model growth simulations, after the acute state hemodynamics were manually prescribed.  $R_{as}$ , MVBR, and LV elastance were manually prescribed. SBV and  $R_{cs}$  were kept constant. The reflex model results (described by **Figure 3.1**) are shown in the solid-colored lines where hemodynamics are computed during the phenomenological short- and long-term reflex systems. Experimental results are depicted by the black error bars (mean  $\pm$  1 standard deviation). The baseline state is the time point before day 0 and the acute state is time point at day 0.  $F_{g,ff}$  is fiber growth and  $F_{g,rr}$  is radial growth.  $F_g$  is the growth tensor.

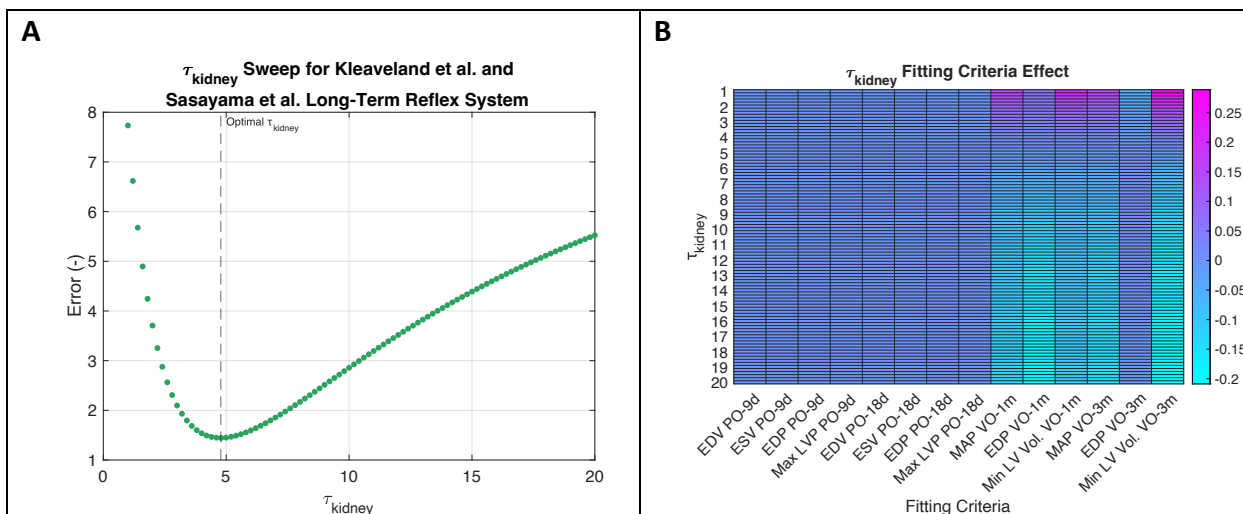
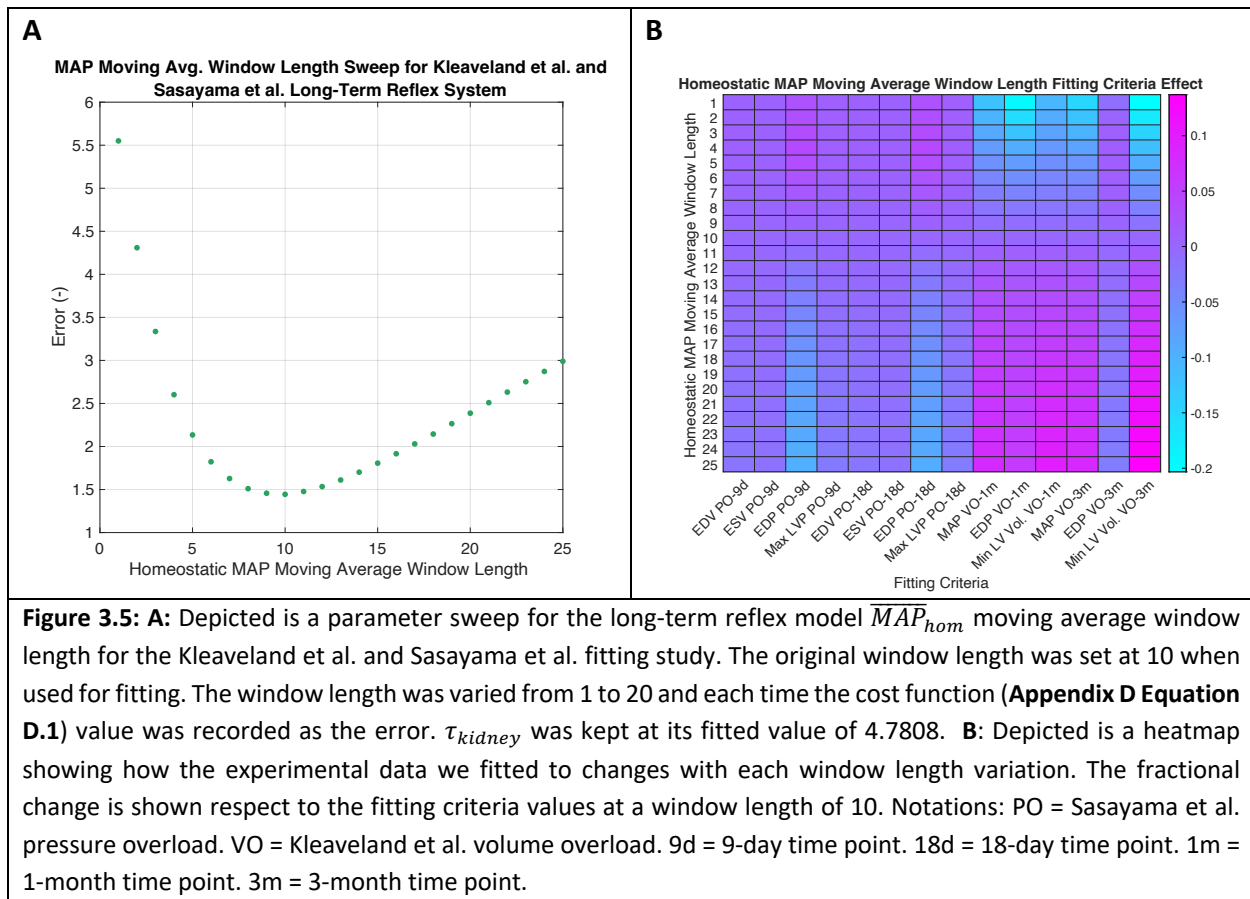


**Figure 3.4: A:** Depicted is a parameter sweep for the long-term reflex model to test the uniqueness of the solution fitted to the Kleaveland et al. and Sasayama et al. studies. The optimized parameter,  $\tau_{kidney}$ , was varied from 1 to 20, and the cost function (**Appendix D Equation D.1**) value was recorded as the error. The optimal  $\tau_{kidney}$  (fitted value) is depicted by the vertical dotted line. **B:** Depicted is a heatmap showing how the experimental data we fitted to changes with each  $\tau_{kidney}$  variation. The fractional change is shown respect to the fitting criteria values at the fitted  $\tau_{kidney} = 4.7808$ . Notations: PO = Sasayama et al. pressure overload. VO = Kleaveland et al. volume overload. 9d = 9-day time point. 18d = 18-day time point. 1m = 1-month time point. 3m = 3-month time point.



### 3.4 DISCUSSION

The goal of Chapter 3 was to develop a long-term reflex model that regulates blood volumes based on long-term changes in MAP. **Figure 3.3** and **Figure 3.4** show that the long-term reflex model can capture the necessary changes for SBV in computing fiber growth over the course of several days for volume and pressure overload. In all three studies, the long-term reflex model accurately predicted the evolution of LV volumes and pressures. There was error in predicting LV EDP and systolic arterial pressure in the Nakano et al. study likely because the short-term errors carried over into the long-term system. We hypothesize that fixing the short-term errors in the Nakano et al. study will help the long-term reflex model better predict EDP and systolic arterial pressure. We also concluded that the long-term reflex model slightly underestimates the changes in end diastolic wall thickening (radial growth). In addition, the results show that the coupled reflex model (short-term + long-term reflexes) can capture LV growth in pressure and volume overload in canines to similar levels of the original rapid-computational model where hemodynamics were manually prescribed.

Similar to the original rapid-computational model, we still cannot capture the decrease in systolic arterial pressure and no change EDP in the Nakano et al. volume overload study. Although these errors may in part to the error in the short-term prediction, **Equation 3.1** still cannot capture both a decrease in systolic arterial pressure and EDP because when MAP increases, SBV will go up resulting in an increased EDP. This scenario highlights that a simplified hemodynamic model adjusting blood volumes based only on one input (MAP) may not be sufficient to capture the hemodynamic response following volume overload. A more detailed model of the renin-angiotensin system may be needed to better regulate the long-term changes in blood volume. For instance, Beard et al. described long-term hemodynamic regulation using a system of ODEs to describe renin-angiotensin activity and neurohumoral control of pressure diuresis/natriuresis [33].

Although total peripheral resistance plays a diminished role in long-term regulation of CO, CO goes back to its baseline state several days after the acute state, including in volume overload [9], [39]. Our long-term reflex system does not try to bring CO down; consequently, we see an increase in CO in both volume overload simulations (**Figure 3.3F** and **Figure 3.4G**). This suggests that we may need to implement a control system to drive back to CO to its baseline state independent of  $R_{as}$ .

Our long-term reflex model is also limited in the fact that it does not use any hormonal inputs to regulate angiotensin-II activity. Estrada et al. previously coupled a cell signaling network model to a LV growth model and showed that hormones, in addition to mechanics, play a major role in cardiac growth [14]. Hormonal outputs from the cell signaling network can feed into a physiologically detailed long-term reflex model to get accurate levels of renin and angiotensin II levels to adapt hemodynamics. The cell signaling model already includes angiotensin-II inside its network. A reflex model that takes in hormonal inputs can be coupled to the framework described by Estrada et al. to further improve long-term hemodynamic predictions.

## 4 CHAPTER 4: CLINICAL MODEL VALIDATION WITH MITRACLIP PATIENTS

### 4.1 INTRODUCTION

In Chapters 2 and 3, we discussed how various short-term reflex models and a long-term reflex model can be used to predict hemodynamic changes after an intervention that causes pressure or volume overload in canines. In the earlier chapters, we wanted to model forward LV growth happening during a diseased state. In Chapter 4, we aim to further validate our coupled reflex model (**Figure 3.1**) against patients who have chronic volume overload but are then treated for it. We are now focused on predicting to what extent the existing LV hypertrophy from chronic volume overload will reverse after a treatment is prescribed to the patient. We used a dataset that consists of patients who have severe or moderate-severe mitral regurgitation (MR) and have undergone a treatment known as MitraClip surgery.

Moderate and severe MR is becoming more and more prevalent in the aging population [51]. Traditionally, to fix the damaged mitral valve leaflets, the patient must undergo surgical mitral valve repair/replacement. Surgical mitral valve repair/replacement has improved patient symptoms, mortality, and LV geometry; however, many of the patients who have MR cannot undergo surgery due to prior comorbidities or because they are deemed to be at prohibitive risk for surgery. As a result, patients who have severe mitral regurgitation and cannot have mitral valve surgery are now eligible to undergo MitraClip treatment [52]. MitraClip treatment (also known as transcatheter mitral valve repair) is a minimally invasive mitral valve repair technique where a clip is placed on the mitral valve leaflets to allow them to fully close and prevent regurgitation. The MitraClip is delivered via a catheter guided by fluoroscopy and transesophageal echocardiography [53].

As previously discussed in section 1.1.1, MR often causes volume overload in the heart because the mitral valve cannot close properly, causing blood to regurgitate across the valve. Thus, the heart must pump a higher volume – the forward stroke volume plus the regurgitant volume – with each beat. Volume overload causes eccentric hypertrophy, in which the LV diameter increases resulting in larger EDVs. MitraClip treatment has been shown to cause reversal of eccentric LV growth because the MR is reduced [54]. Although MitraClip treatment has a high success rate of reducing MR severity, subsequent LV remodeling responses among patients differ vastly. Different studies report different changes in LV growth identifiers (LV cavity diameter, end systolic elastance, EDV, etc.) after clip implantation. For instance, some studies report that MitraClip treatment has been shown to significantly reduce LV EDV several months after clip implantation [54], [55], while other studies report that there is not a significant change

in EDV [56]. Further analysis of these studies suggests a high variability in patient response metrics. Therefore, understanding patient-specific responses might help clinicians better gauge if MitraClip treatment can improve patient health on an individual basis.

There are several variables that influence a patient's MitraClip outcome, and correlative statistical approaches for analyzing MitraClip datasets do not provide enough insight into why an individual patient is responding in a particular way. Thus, our goal is to use our computational growth and hemodynamic modeling frameworks to model LV growth on a personalized patient basis. Our modeling framework allows us to simulate MitraClip implantation in patients before they even go into surgery, which could help guide a personalized treatment depending on how much reversal of LV growth we see in a patient. In this chapter, we use our coupled rapid-computational model and reflex model to predict LV growth in individual patients who have undergone MitraClip treatment.

## 4.2 METHODS

### 4.2.1 Curating the Dataset

We obtained access to data from MitraClip implantations performed at UVA between March 2009 and December 2014. We recorded data for 16 patients consisting of 7 males and 9 females. Ages ranged from 73 to 92 years old. These patients included 1 Asian, 4 African Americans, and 11 Caucasians.

As described in **Table 4.1**, patient measurements of interest were recorded at the following time points: before MitraClip implantation (pre), immediately after implantation (post), 1 month after implantation (post 1 month), 6 months after implantation (post 6 months), and 1 year after implantation (post 1 year). Patients underwent a transthoracic echo (TTE) examination at each time point, and LV geometrical measurements were recorded. (**Table 4.1**). From the TTE, we calculated LV EDV and ESV by outlining the LV myocardial wall and using Simpson's Biplane Method [57]. We used the peak of the R-wave from the electrocardiogram (ECG) to estimate end diastole and used the TTE frame where the LV diameter was the smallest (about 40% of the QRS duration) to estimate end systole. Before MitraClip implantation (pre), we recorded the minimum volume rather than the ESV because it was difficult to estimate end systole in patients with severe MR.

To quantify MR, we compute regurgitant fractions (RF) in each of the patients. As described later, RF is a vital parameter to prescribe MR in our computational modeling framework. RF is defined as the fraction of blood that is flowing backwards into the left atrium within each cardiac cycle. From the TTE, we can compute the amount of blood that passes the aortic valve and subtract it from the total stroke volume (difference between EDV and ESV) to compute the regurgitant volume. The RF calculation is described in **Equation 4.1**:

$$RF = \frac{(EDV - ESV) - (LVOT_{VTI})(LVOT_{CSA})}{EDV - ESV} \quad \text{Equation 4.1}$$

where  $EDV$  and  $ESV$  are the end diastolic and end systolic volumes, respectively.  $LVOT_{VTI}$  is the LV outflow tract velocity time integral, and  $LVOT_{CSA}$  is the LV outflow tract cross sectional area. Based on the principle of continuity, the product of  $LVOT_{VTI}$  and  $LVOT_{CSA}$  is equivalent to the stroke volume across the aortic valve [58].  $LVOT_{VTI}$  is computed from pulsed Doppler during TTE by integrating the velocity of volume going through the outflow tract below the aortic valve respect to time. To compute  $LVOT_{CSA}$ , we assume the aortic valve is circular and use the following relationship:  $LVOT_{CSA} = 0.785 \times LVOT_{diameter}^2$  [59].

Right before the implantation (minutes to hours before) and right after the implantation (minutes to hours after), left atrial (LA) and aortic pressure measurements were recorded using a pressure catheter. HR was logged at each time point. CO measured using thermodilution was recorded before and right after the implantation. Total systemic vascular resistance (TSVR) was recorded right after the implantation.

**Table 4.1:** Depicted below are the patient measurements of interest we recorded. Measurements taken from TTE are shown in pink, and all other measurements are shown purple. Note: RF was calculated using TTE measurements (**Equation. 4.1**). Measurements taken at pre from TTE were recorded between 2 months to 1 day before surgery depending on the patient. Measurements taken at post from TTE were recorded between hours to 1 day after surgery depending on the patient. Pressure, thermodilution, HR, and resistance measurements were taken either hours to minutes before surgery (pre) or minutes to hours after surgery (post). HR at post 1 month, post 6 months, and post 1 year was recorded from the TTE procedure. LV EDV and ESV was mostly measured by either the TTE technician, but we measured the volumes when data from the technician was not available.

| Measurement   | Time points measurement was recorded |      |              |               |             |
|---|--------------------------------------|------|--------------|---------------|-------------|
|   | Pre                                  | Post | Post 1 Month | Post 6 Months | Post 1 Year |
| LV Interventricular Septum Thickness at Diastole (IVSd) | ✓                                    | ✓    | ✓            | ✓             | ✓           |
| LV Internal Diameter at Diastole (LVIDd)                | ✓                                    | ✓    | ✓            | ✓             | ✓           |
| LV Posterior Wall Thickness at Diastole (LVPWd)         | ✓                                    | ✓    | ✓            | ✓             | ✓           |
| LV Internal Diameter at Systole (LVIDs)                 | ✓                                    | ✓    | ✓            | ✓             | ✓           |
| LVOT VTI  | ✓                                    |      |              |               |             |
| LVOT Diameter   | ✓                                    |      |              |               |             |
| Mitral Valve (MV) VTI                                   | ✓                                    |      |              |               |             |
| MR Effective Regurgitant Orifice Area (EROA)            | ✓                                    |      |              |               |             |

|   |   |   |   |   |   |
|---|---|---|---|---|---|
| MR VTI                                    | ✓ |   |   |   |   |
| LV EDV                                    | ✓ | ✓ | ✓ | ✓ | ✓ |
| LV ESV                                    | ✓ | ✓ | ✓ | ✓ | ✓ |
| Regurgitant Fraction (RF)                 | ✓ |   |   |   |   |
| Systolic LA Pressure                      | ✓ | ✓ |   |   |   |
| Diastolic LA Pressure                     | ✓ | ✓ |   |   |   |
| Systolic Aortic Pressure                  | ✓ | ✓ |   |   |   |
| Diastolic Aortic Pressure                 | ✓ | ✓ |   |   |   |
| Systolic Pulmonary Pressure               | ✓ | ✓ |   |   |   |
| Diastolic Pulmonary Pressure              | ✓ | ✓ |   |   |   |
| Thermodilution Cardiac Output (TDCO)      | ✓ | ✓ |   |   |   |
| Heart Rate (HR)                           | ✓ | ✓ | ✓ | ✓ | ✓ |
| Total Systemic Vascular Resistance (TSVR) |   | ✓ |   |   |   |

#### 4.2.2 Fitting Baseline State for Patients

Before modeling LV reverse growth in the MitraClip patients, we fitted the following rapid-computational model parameters to match the baseline (diseased) state of each patient: baseline SBV and baseline  $R_{as}$ . The goal was to obtain a baseline PV loop at the MR state for each patient so that we can later prescribe MitraClip treatment in our model and compute the acute state using the phenomenological short-term reflex model.

To predict patient-specific outcomes for MitraClip patients, we had to recalibrate several parameters in the rapid-computational model. Since the lumped parameter circulation system was calibrated for canines, we needed to use resistance and capacitance values that reflected the human circulation. It was difficult to fit the rapid-computational model circulatory parameters for each patient because not enough circulation data was collected during the MitraClip procedure. As a result, we adopted resistance and capacitance values from Burkhoff and Tyberg who adapted their circulation system for a 75kg male [40]. The circulation parameters are shown in **Table 4.2**.

Baseline SBV and  $R_{as}$  were fitted for each patient to match his/her EDP, end diastolic volume index (EDVI), minimum volume index (minVoll), MAP, regurgitant fraction (RF), and mean pulmonary arterial pressure (mPAP) (Cost function was **Appendix Equation E.1**). LV EDP was not directly measured; however, a Wigger's diagram suggests that systolic left atrial pressure (systolic LAP) is a good estimate for LV EDP. We used the *fmincon* optimization algorithm with a nonnegativity constraint for fitting [45]. Since our circulation parameters are originally calibrated to a 75 kg male [40], we corrected all LV volumes for body surface area (BSA) to obtain EDVI, minVoll, and end systolic volume index (ESVI) (**Equation 4.2**).

$$LV\ Volume\ Index = \frac{(LV\ Volume)(BSA_{75kg\ male})}{BSA_{patient}} \quad \text{Equation 4.2}$$

where LV Volume is the measured volume from TTE,  $BSA_{75kg\ male} = 1.9\ m^2$ , and  $BSA_{patient}$  is the BSA of the patient.

In addition to fitting SBV and  $R_{as}$ , several rapid-computational model parameters had to be specified for each patient. MVBR was prescribed based on the amount of RF present in each patient. We developed a calibration curve by varying MVBR from 0.01 to 4.5 for the canines from the Kleaveland et al. and Nakano et al. volume overload studies and computing the resulting RF after running the rapid computational model. A power function was fitted to obtain a calibration curve that could be used to estimate MVBR to achieve a desired RF (**Figure 4.1**).

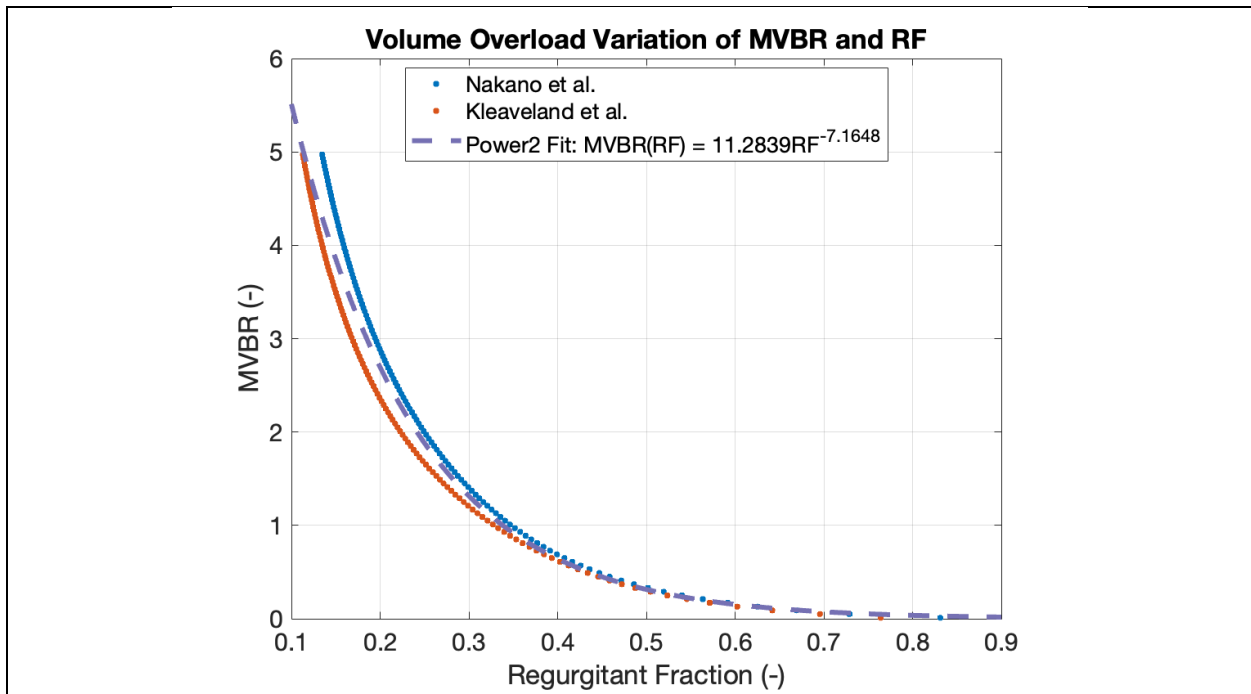


**Figure 4.1:** Depicted are the variations of the MVBR and the resulting regurgitant fractions in the Kleaveland et al. and Nakano et al. canine volume overload studies. At each MVBR, the rapid-computational model was run for each canine study, and the regurgitant fraction was recorded. A power function was fitted to create a calibration curve that inputs regurgitant fraction and outputs MVBR. The function with its fitted parameters is shown in the legend.

The rapid-computational model uses 4 parameters to describe the end systolic pressure volume relationship (ESPVR) and the end diastolic pressure volume relation (EDPVR):  $A$ ,  $B$ ,  $E_{max}$ , and  $V_0$ . The ESPVR and EDPVR are shown in **Equation 4.3** and **4.4**, respectively:

$$P_{ES} = E_{max}(V_{ES} - V_0) \quad \text{Equation 4.3}$$

$$P_{ED} = Ae^{B(V_{ED}-V_0)} - A \quad \text{Equation 4.4}$$

where  $P_{ES}$  and  $P_{ED}$  are the end systolic and end diastolic pressure, respectively.  $V_{ES}$  and  $V_{ED}$  are the end systolic and end diastolic volume, respectively.  $A$  and  $B$  are myocardial material parameters that we kept at the same values as Burkhoff and Tyberg.  $E_{max}$  is the maximum LV end systolic elastance, and since we did not have any data about the patient's LV contractility, we kept  $E_{max}$  at the same value as Burkhoff and Tyberg [40]. We assumed it was same among all patients for the baseline state.  $V_0$  is the unloaded volume in the left ventricle (LV volume when  $P_{ES} = 0$  mmHg).  $V_0$  was estimated for each patient based on a linear ESPVR assumption (**Equation 4.3**). Since we could not obtain patient end systolic pressures ( $P_{ES}$ ), we estimated  $P_{ES}$  based on blood pressure cuff (arterial pressures) measurements (**Equation 4.5**) as previously described by Kelly et al. [60].

$$P_{ES} = \frac{2P_s + P_d}{3} \quad \text{Equation 4.5}$$

where  $P_s$  and  $P_d$  are the systolic and diastolic arterial pressures, respectively.  $P_s$  and  $P_d$  were obtained from blood pressure cuff measurements, but systolic and diastolic aortic catheter pressure measurements were used when available. Now that we know  $P_{ES}$ , we can solve for  $V_0$  in **Equation 4.3**. HR at the pre time point was prescribed for each patient. All the baseline rapid-computational model parameters are summarized in **Table 4.2**.

**Table 4.2:** Depicted below are a description of the rapid-computational model parameters used to create the baseline state for each patient.

| <b>Value</b>                         | <b>Description</b>                  | <b>Source</b>            |
|--------------------------------------|-------------------------------------|--------------------------|
| <b>Circulation Parameters</b>        |                                     |                          |
| $R_{as} = \textit{patient specific}$ | Systemic Arterial Resistance        | Fitted                   |
| $R_{ap} = 0.03 \text{ mmHg*s/mL}$    | Pulmonary Arterial Resistance       | Burkhoff and Tyberg [40] |
| $R_{cs} = 0.03 \text{ mmHg*s/mL}$    | Systemic Characteristic Resistance  | Burkhoff and Tyberg [40] |
| $R_{cp} = 0.02 \text{ mmHg*s/mL}$    | Pulmonary Characteristic Resistance | Burkhoff and Tyberg [40] |
| $R_{vs} = 0.015 \text{ mmHg*s/mL}$   | Systemic Venous Resistance          | Burkhoff and Tyberg [40] |
| $R_{vp} = 0.015 \text{ mmHg*s/mL}$   | Pulmonary Venous Resistance         | Burkhoff and Tyberg [40] |
| $C_{as} = 1.32 \text{ mL/mmHg}$      | Systemic Arterial Capacitance       | Burkhoff and Tyberg [40] |
| $C_{ap} = 13 \text{ mL/mmHg}$        | Pulmonary Arterial Capacitance      | Burkhoff and Tyberg [40] |
| $C_{vs} = 70 \text{ mL/mmHg}$        | Systemic Venous Capacitance         | Burkhoff and Tyberg [40] |
| $C_{vp} = 8 \text{ mL/mmHg}$         | Pulmonary Venous Capacitance        | Burkhoff and Tyberg [40] |

| ESPVR/EDPVR Parameters                 |                                |                          |
|--|--------------------------------|--------------------------|
| $E_{\max} = 3 \text{ mmHg/mL}$         | LV end systolic elastance      | Burkhoff and Tyberg [40] |
| $A = 0.35 \text{ mmHg}$                | Linear material parameter      | Burkhoff and Tyberg [40] |
| $B = 0.033$                            | Exponential material parameter | Burkhoff and Tyberg [40] |
| $V_0 = \textit{patient specific}$      | Unloaded LV Volume             | Calculated               |
| Other Parameters                       |                                |                          |
| Baseline SBV = <i>patient specific</i> | Baseline stressed blood volume | Fitted                   |
| Baseline HR = <i>patient specific</i>  | Baseline Heart Rate            | Patient dataset          |

#### 4.2.3 Using Rapid-Computational Model and Reflex Model to Predict LV Growth

After fitting the baseline (diseased) state for each patient, using the rapid-computational model, we used our coupled reflex and rapid-computational model to predict LV growth. The reflex model, earlier described in **Figure 3.1**, is the coupled phenomenological short- and long-term reflex system. The phenomenological short-term reflex system is used to compute hemodynamics for the acute (immediately after MitraClip implantation) state, and the long-term reflex system is used compute hemodynamics at the post 1 month, 6 months, and 1 year states after MitraClip implantation. When the reflex model is coupled to the rapid-computational model, we can predict both hemodynamic changes and LV growth for individual MitraClip patients.

The acute state is defined as immediately (hours to 1 day) after MitraClip implantation. To simulate MitraClip implantation, we assume there is no more regurgitation; thus, we prescribe an MVBR of infinity. After imposing a step change in MVBR, the phenomenological short-term reflex model is run until MAP and CO reach steady state to obtain a new acute state SBV and  $R_{as}$ . We used the same phenomenological short-term reflex model parameters that were originally fitted to Kleaveland et al. and Sasayama et al. Since the phenomenological short-term reflex model cannot predict HR, we manually prescribed HR based on the patient's post time point HR. In terms of ESPVR and EDPVR parameters, we kept  $E_{\max}$  constant from baseline to acute. Gaemperli et al. did not find a significant difference in LV end systolic elastance before and after MitraClip implantation when looking at patients with functional and degenerative MR [56]. We assume the ESPVR did not shift from baseline to acute, so we kept  $V_0$  constant from baseline to acute. We also assume that the material properties did not change from baseline to acute; thus, we keep  $A$  and  $B$  constant at their baseline value.

After the computing the acute state, we used the long-term reflex model to predict hemodynamics necessary for the rapid-computational model to compute growth. Since we do not have RF information at the post 1 month, 6 months, and 1 year time points, we assumed that there was no MR and prescribe MVBR to be infinity throughout growth. The long-term reflex model predicts SBV throughout growth based on MAP (**Equation 3.1**). We kept  $R_{as}$  constant at its acute state value throughout the growth simulation because our long-term reflex model does

not adapt  $R_{as}$ . HR was manually prescribed based on post 1 month, 6 month, and 1 year recordings using a linear interpolation based on the available data. We used the same long-term reflex model parameters that were originally fitted to Kleaveland et al. and Sasayama et al. Similar to the canine studies, we ran the long-term reflex model 5 times between each growth step. Each rapid-computational model iteration is considered 1 growth step, which simulates 5 days of growth. We computed initial LV wall volume, a rapid-computational growth model parameter, using **Appendix Equation E.2**.  $A$ ,  $B$ ,  $E_{max}$ , and  $V_0$  were adapted during growth in the rapid-computational model as previously described by Witzenburg and Holmes which was based on the fiber and radial growth at every growth step [18]

We previously modeled forward LV growth because we modeled growth following an intervention that induces pressure or volume overload, and we always treated baseline as the healthy state of the heart. However, when modeling MitraClip patients, we want to model LV growth following an intervention that treats volume overload. Since the baseline state is the diseased state of the heart, we are now modeling reverse growth after the acute state because the LV is going to reverse grow to return to its healthy state. Yoshida et al. previously modified Kerckhoffs strain-based growth law by implementing an evolving homeostatic growth setpoint to allow for reversal of growth in a pressure overload study [19]. Oomen et al. later showed that the evolving homeostatic growth setpoint in the growth law can be used predict reverse remodeling in patients with left bundle branch block [20]. As a result, we used the modified growth law to predict reverse growth in MR patients, all of whom have volume overload. We used the same evolving homeostatic growth setpoint memory window as Oomen et al. Due to time constraints, we only modeled patient specific responses for 3 patients.

## 4.3 RESULTS

### 4.3.1 Exploratory MitraClip Dataset Analysis

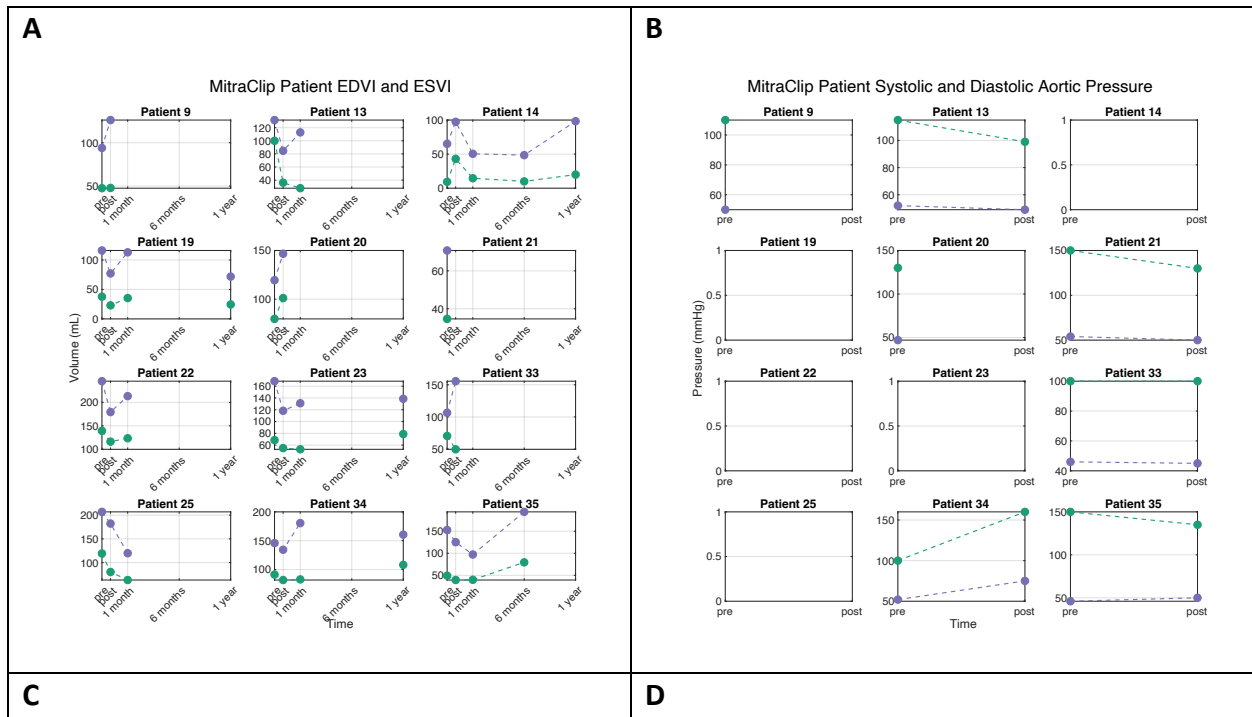
Prior to modeling any of the patients, we conducted a simple exploratory analysis of the data to identify any trends in key growth metrics. **Figure 4.2** shows some of the key changes in patient measurements. It is important to note that in our data collection process, we were not able to obtain all the measurements necessary to run our modeling framework; thus, we are only displaying patients that had enough data to complete the modeling process.

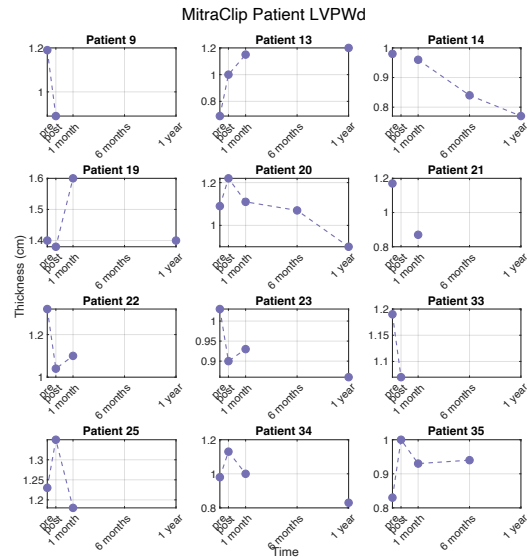
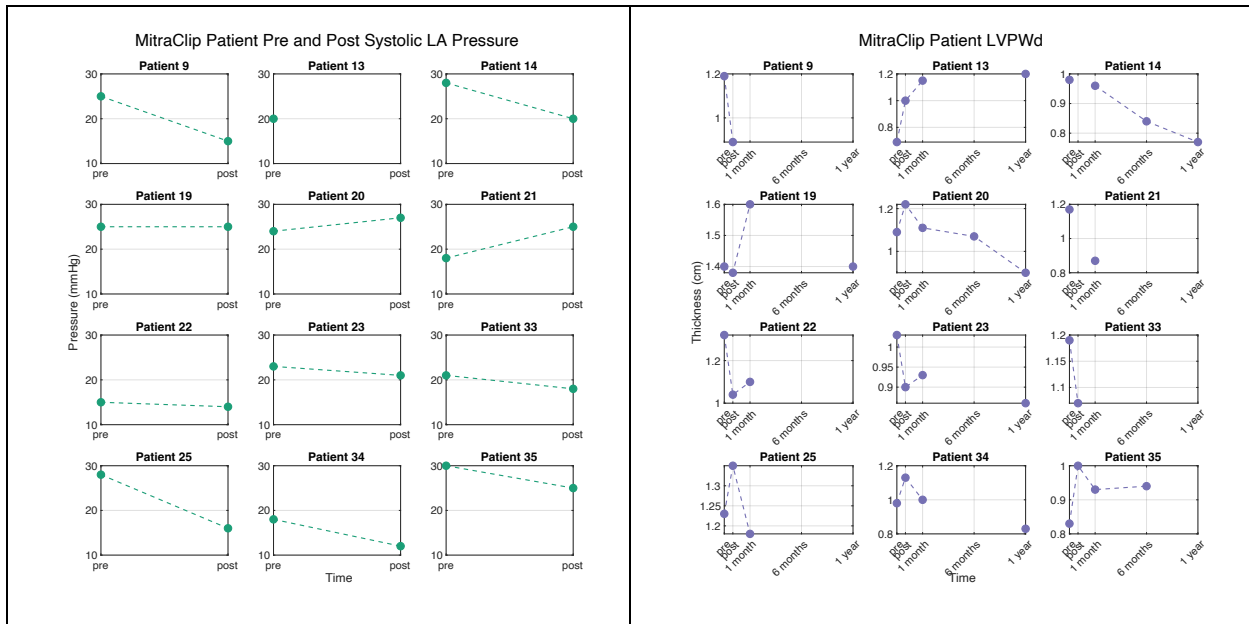
LV EDVI is an indicator of reduction in LV cavity dilation during reverse eccentric growth. In most patients, we see a decrease in EDVI from pre to post, but then see an increase in EDVI (**Figure 4.2A**). This likely suggests that the MitraClip reduced regurgitation at the early time points after surgery, but some regurgitation came back at post 6 months and post 1 year.

In several of the patients, we lacked aortic pressure measurements (**Figure 4.2B**); however, we only needed the MAP at the pre time point to set the initial homeostatic setpoint

for the long-term reflex model. In instances where we lack pre aortic pressure measurements, we would use blood pressure cuff measurements as a substitute. In most patients, we see an acute decrease in systolic LAP immediately after application of the MitraClip; however, in some patients, systolic LAP increased from pre to post (**Figure 4.2C**).

Although not indicative of volume overload and eccentric growth, we saw several changes in LV wall thickness (**Figure 4.2D**). In the canine studies from Chapters 2 and 3, volume overload caused only small changes in wall thickness, whereas in the MitraClip patients, we see changes in wall thickness as much as 40%. As expected and similar to EDVI, we see an initial decrease in LV cavity diameter (**Figure 4.2E**), but then an increase at time points after MitraClip implantation.





E

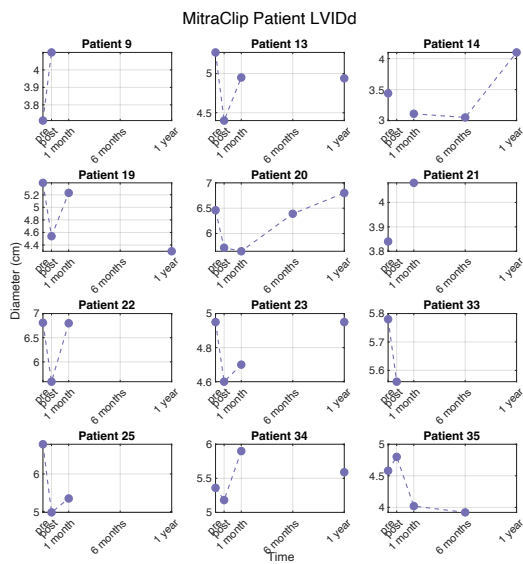


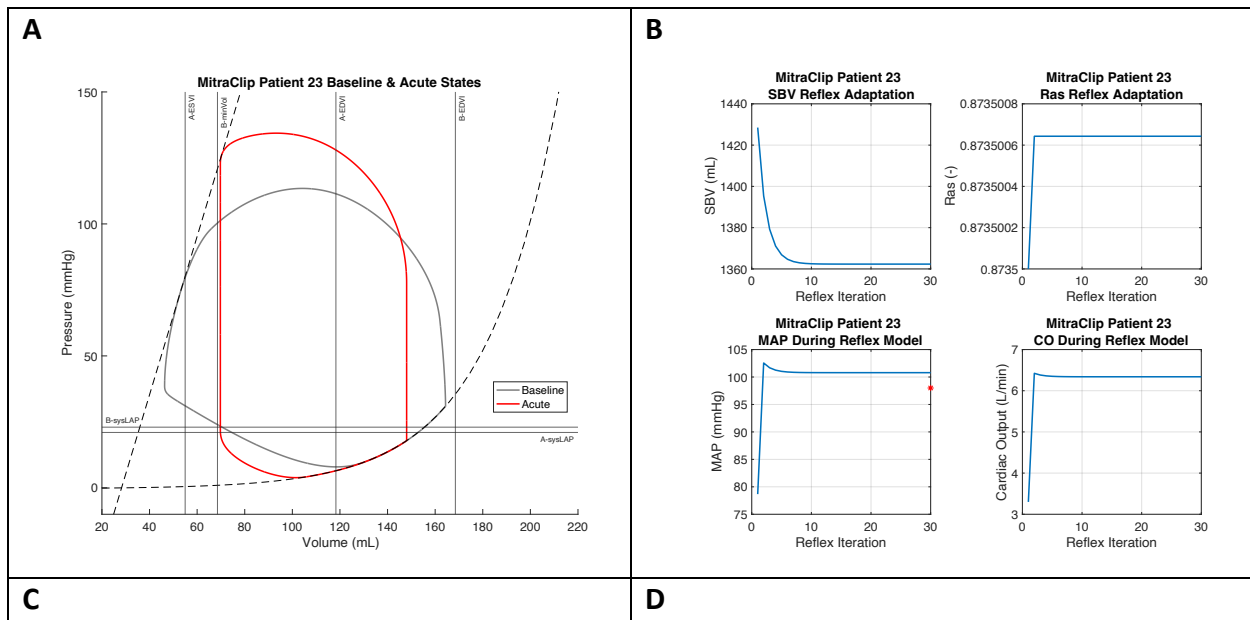
**Figure 4.2:** **A:** Depicted are the measured patient end diastolic volume indexes (EDVIs) and end systolic volume indexes (ESVIs) at pre, post, post 1 month, post 6 months, and post 1 year. **B:** Depicted are the measured patient systolic and diastolic aortic pressures at pre and post. **C:** Depicted are the measured systolic and diastolic left atrial (LA) pressures pre and post. **D:** Depicted is LV posterior wall thickness at diastole (LVPWd). **E:** Depicted is LV internal diameter at diastole (LVIDd). In all panels, diastolic measurements are shown in purple and systolic measurements are shown in teal. Note: for several patients, not all data was available at all time points.

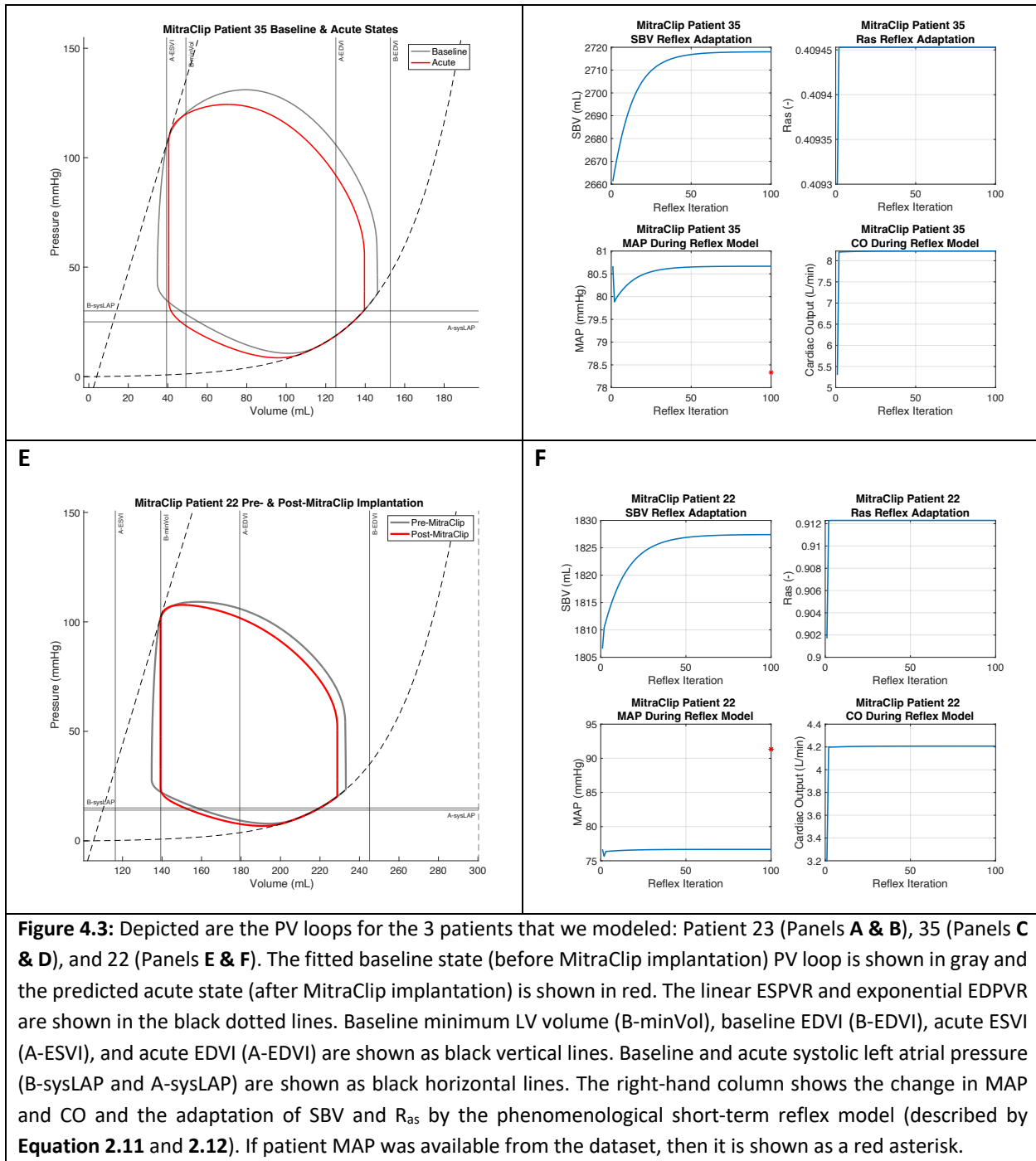
### 4.3.2 Patient-Specific Modeling Results

**Figure 4.3** shows the fitted baseline states when running only the rapid-computational model and the acute state when the phenomenological short-term reflex model was run for 3 of

the patients we modeled. In each of the 3 patients, our model was able to predict the decrease in EDVI from baseline to acute; however, we underestimated the magnitude of the decrease in EDVI. The limited decrease in EDVI in the model could have been caused by an underestimate of the change in SBV or by an inappropriately steep EDPVR. In patients 23 and 35, MAP was measured at the post time point in our dataset. We were able to predict the acute state MAP in patient 23, but not in patient 35.

In all three patients, according to the measurements in our dataset, ESVI decreased from baseline to acute (**Figure 4.3A,C,E**), and our model was not able to accurately predict the lower ESVI. Since we keep the ESPVR constant from baseline to acute, it was difficult for the model to capture the lower ESVI because that would require a left shift of the ESPVR, assuming ESP does not drop very low. In all three patients, the model was not able to accurately match the systolic arterial pressures. Our model predictions for MAP varied among the 3 patients; as a result, we could not reach a conclusion whether our model was able to accurately predict MAP.



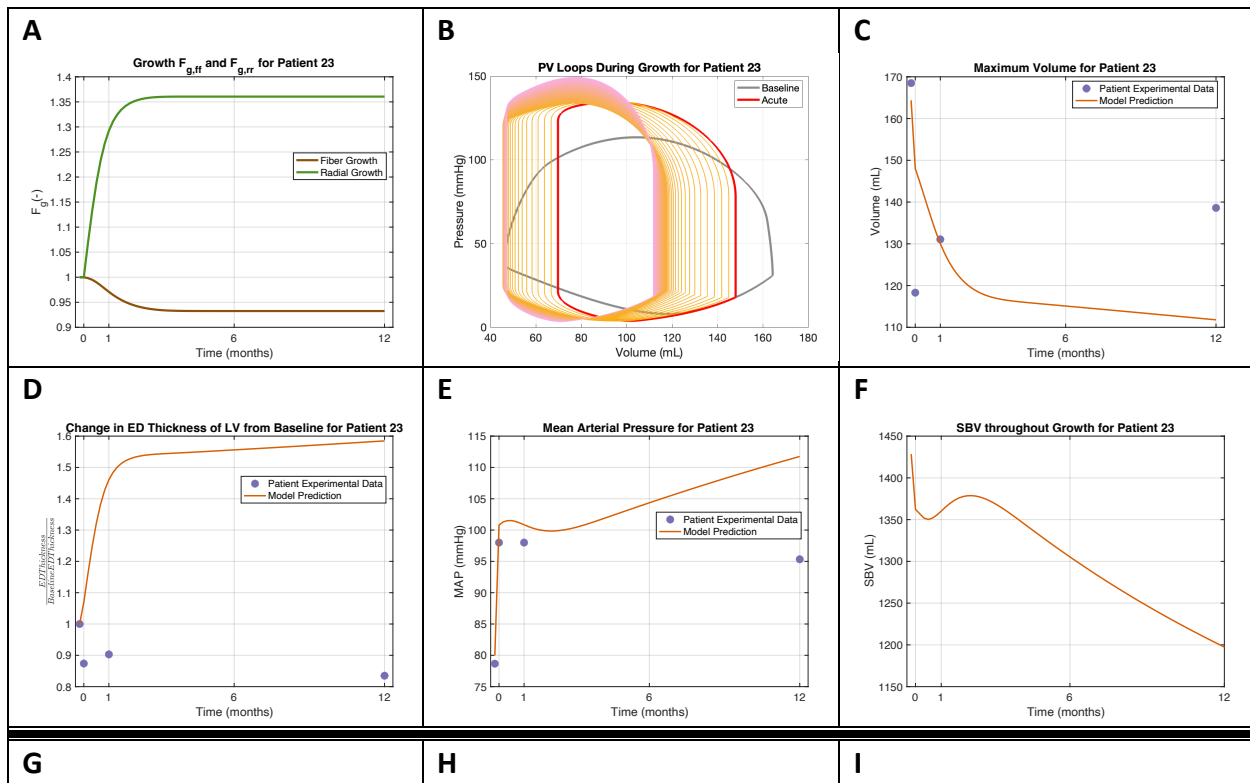


Figures 4.4 shows the LV growth modeling results for patients 23, 35, and 22 when we ran the coupled reflex model and rapid-computational model. In the 3 patients, our model showed a reversal of growth in the fiber direction (i.e., reversal of eccentric growth) which is what we expect after MitraClip implantation. We also expect to see a decrease in maximum LV volume (EDVI) at every time point after MitraClip implantation. In the 3 patients, maximum volume dropped from baseline to acute, but increased from acute to post 1 month. Our model

did not match the maximum volume at the acute state (**Figure 4.3**); however, the model was able to match the maximum LV volume at post 1 month in patients 23 and 22. As a result, the model can capture the overall decrease in maximum LV volume from baseline to post 1 month, but the model cannot capture the increase in maximum LV volume that is observed from acute to post 1 month.

The growth curves (**Figure 4.4A,G,M**) in the 3 patients show predicted radial growth; however, when we look at the measured patient change in end diastolic thickness (**Figure 4.4J,P**) from our dataset, there is a decrease in end diastolic thickness. According to the growth law we used, changes in end systolic strains drive radial growth. From baseline to acute, we saw an increase in ESV which resulted in larger end systolic strains, relative to baseline, leading to some radial growth. In our rapid-computational growth model, a decrease in ESV tends to produce a decrease in end diastolic wall thickness. Thus, we need to better match patient ESVs to match the end diastolic wall thickness. In patient 35, there was an increase in end diastolic thickness and our model accurately predicted that there was radial growth; however, the model was not able to match the magnitudes of change in end diastolic thickness (**Figure 4.4G**).

In patient 23, we matched the post 1 month MAP; however, the reflex model pushes MAP higher than it was experimentally observed in the patient at post 1 year. In patients 22 and 35, we are not able to match the increase in MAP.



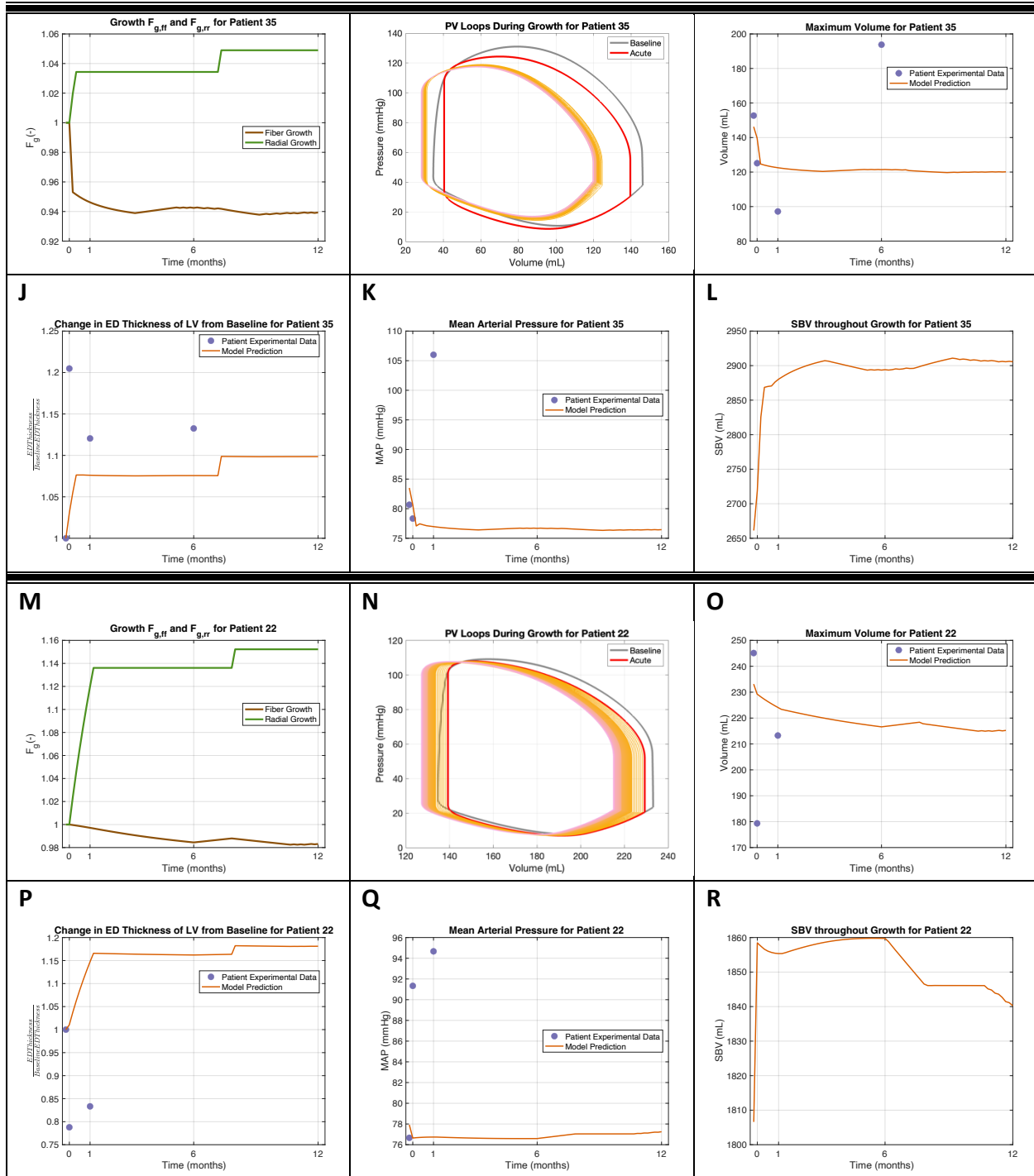
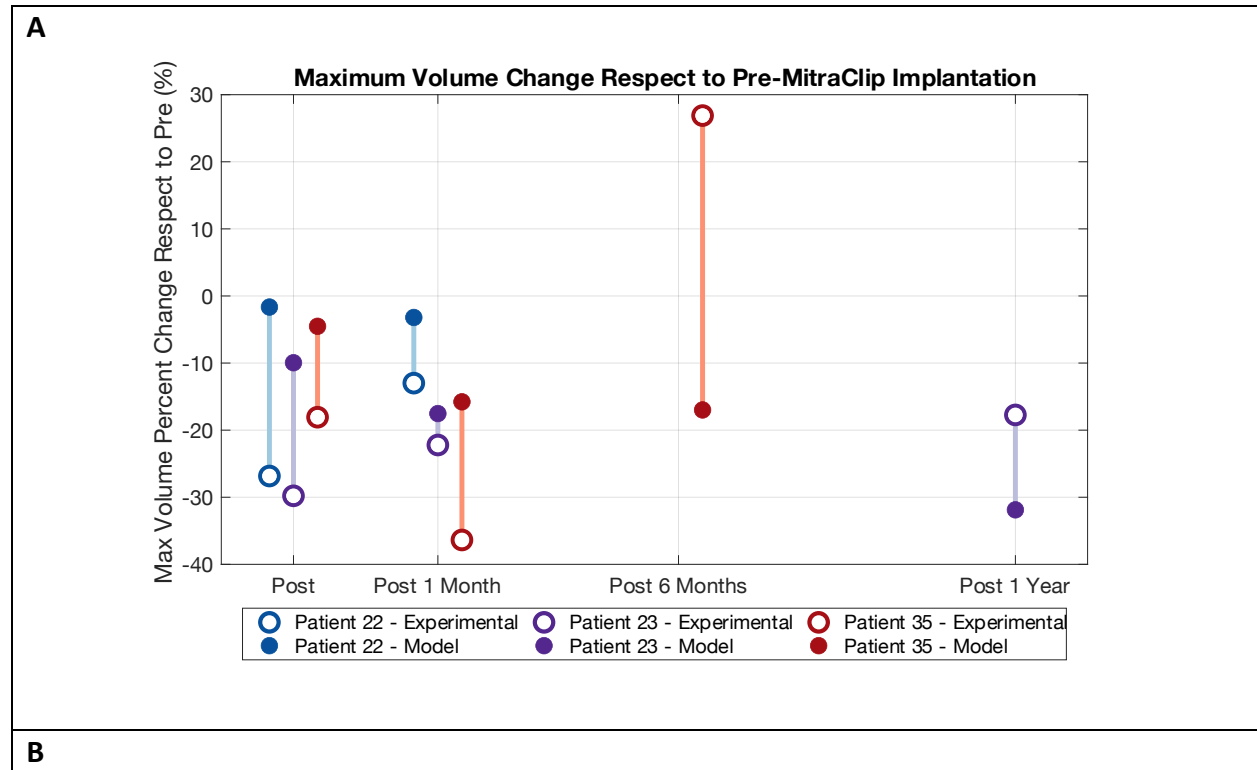


**Figure 4.4:** Depicted are the results from the LV growth simulations for **patient 23 (A-F)**, **patient 35 (G-L)**, and **patient 22 (M-R)** using the coupled reflex model (short-term reflex model + long-term reflex model) and rapid-computational growth model. **A, G, M:** Depicted are the radial ( $F_{g,rr}$ ) and fiber ( $F_{g,ff}$ ) model predictions.  $F_g$  is the growth tensor. **B, H, N:** Depicted are the change in the PV loops during growth. The baseline and acute loops are shown in gray and red, respectively. The orange to pink gradient shows the PV loops as the heart grows (time increase). The gradient goes from 1 day of growth (orange) to 1 year of growth (pink). **C-F, I-L, O-R:** Depicted in these panels are metrics of interest during LV growth. The model prediction is shown in orange and the patient

measurements from our dataset are shown in purple. Time point 0 represents the acute state and the time point before 0 is the baseline state.

Since a decrease in maximum volume (analogous to EDVI in these patients) is indicative of reversal of eccentric growth, we plotted the change in EDVI respect to baseline for all patients to see how our model did (**Figure 4.5A**). For the post and post 1 month time points, our model underestimate EDVI. For two of the patients, the EDVI model prediction error was the smallest at post 1 month, and the error tended to be larger at the post time point. This figure highlights that we cannot match the magnitude of the change in EDVI for the 3 patients.

To simulate a fully prospective patient-specific modeling case, we ran our model without prescribing HR at each time point. Since our modeling framework cannot predict HR, we kept HR constant. Thus, only the baseline (pre) state is fitted and every post state is a prediction (i.e., no parameters were manually prescribed based on post-surgery measurements). The EDVI change results are shown in **Figure 4.5B**. The model predicted very similar EDVIs compared to when HR was manually prescribed from the patient measurements. The errors for patients 33 and 23 at post 1 month and post 1 year, respectively, are smaller when HR is kept constant. The HR constant results suggest that our modeling framework can support prospective patient modeling.



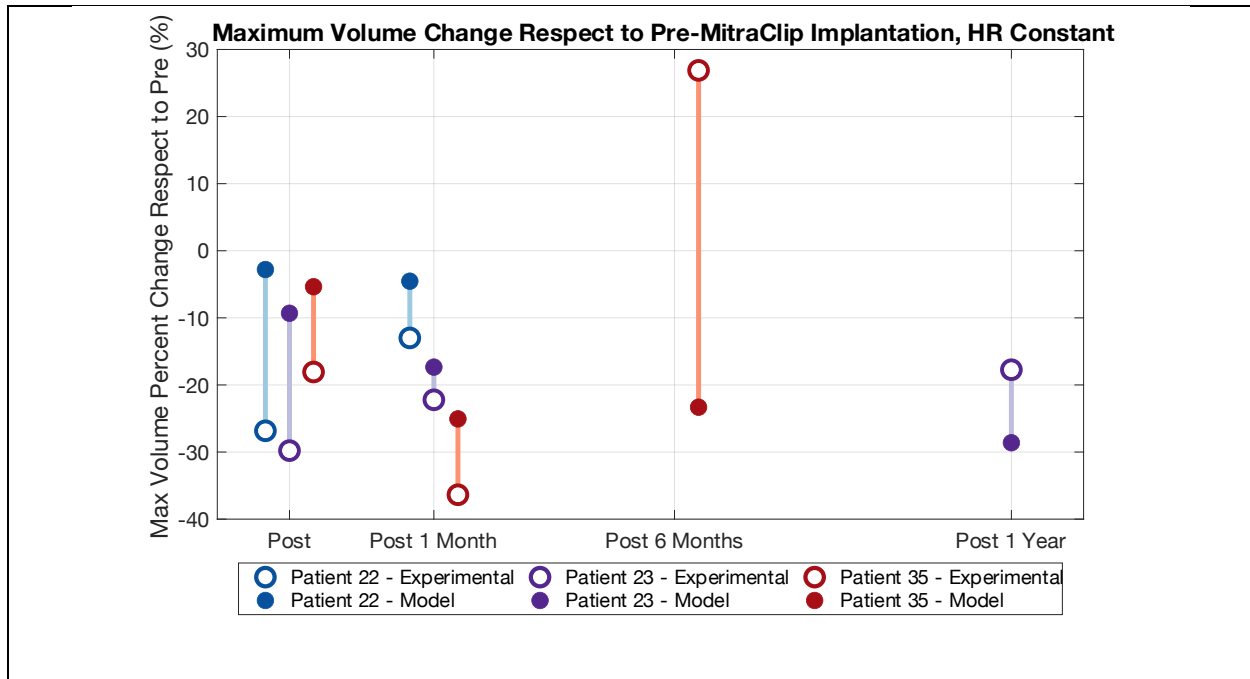


**Figure 4.5: A:** Depicted is a plot of the EDVI change respect to baseline for patients 22 (blue), 23 (purple), and 35 (red) from the dataset and model predictions when HR was manually prescribed at each time point. **B:** Depicted is a plot of the EDVI change respect to baseline when HR was not prescribed (kept constant) at each time for the model (prospective modeling). EDVI change was computed as the difference between baseline (pre) EDVI and each post time point divided by the baseline (pre) EDVI. The patient dataset (experimental) values are shown as the solid colored circles, and the model predictions are shown as the open colored circles.

## 4.4 DISCUSSION

We built a rapid-computational growth and reflex model to prospectively model patient specific responses following disease treatment such as MitraClip implantation. The results from **Figures 4.3** and **4.4** suggest that our modeling framework can predict some reversal of LV growth in MitraClip patients but cannot accurately predict the magnitude of the reversal of cavity size. In addition, the model cannot capture the changes in end diastolic wall thickening (radial growth). Our modeling framework can be further improved to better prospectively model patient specific responses post MitraClip treatment.

Patient data set analysis and the modeling results suggest that accurately calibrating the ESPVR is essential to capturing the baseline and acute state PV loops which is necessary to predicting radial growth. In several patients, we see a decrease in ESVI (**Figure 4.2**), but as shown in our 3 patient modeling cases, we cannot capture the small decrease in ESVI. In all the patient modeling cases, the model predicts an increase in ESVI which leads to increased radial growth. We assume that each patient has the same  $E_{max}$ ; however, patient-specific calibration of  $E_{max}$  may allow us to have a more accurate ESPVR that can capture the small change in ESVI. Chen et al. developed a non-invasive method to estimate  $E_{max}$  based on single heartbeat. They show

that  $E_{max}$  can accurately be estimated using arterial pressures and the ratio of the pre-ejection period to the total systolic period derived from the aortic Doppler waveform [61]. Since we have access to the TTEs for each patient, future work will include computing a patient specific  $E_{max}$ . Better capturing the systolic LV function at baseline and acute may result in better radial growth predictions.

In patients 23 and 35, where post 6 month and 1 year follow up data were available, respectively, the model had trouble estimating the hemodynamics and growth at those times given our MVBR prescription. We assume that MR does not resurface in the patients; however, many of the patients we modeled or intend to model are of old age with several complications where MR may resurface 6-12 months post-surgery. MR recurrence or other complications may explain the late increase in EDVI that our model cannot capture. On the other hand, either the growth law or reflex equations may be contributing to an inability of the model to capture the later increase in EDVI. We used an evolving growth setpoint history window length based on left bundle branch patients calibrated by Oomen et al., but that window might need to be recalibrated for this application. In addition, our long-term reflex model controls hemodynamics solely on MAP. As earlier described in section 3.1.4, we may need to incorporate a more detailed renin-angiotensin reflex system that adapts SBV based on several factors, in addition to MAP, and adapts total peripheral resistance. Beard et al. uses a physiologically detailed model of the renin-angiotensin system that can be implemented in our modeling framework to better predict hemodynamic changes necessary to compute LV growth [33].

In the patients that we modeled, most evidently patients 35 and 22, we see that the magnitude of the decrease in EDVI is relatively small because the change in SBV was relatively small (**Figure 4.3B,D,F**). There are likely two possible reasons we are predicting a small decrease in EDVI. We assumed that the material parameters,  $A$  and  $B$ , are the same as what Burkhoff and Tyberg used for their patients. However, Burkhoff and Tyberg modeled healthy patients, and we modeled patients with dilated LVs due to MR. In dilated LVs, the EDVPR is generally much flatter than normal LVs. Patient-specific material parameters would help generate a flatter EDPVR resulting in larger baseline EDVIs, smaller acute EDVIs, and lower EDPs, which is what we observed in the patient dataset.

Another possibility is that we assumed the phenomenological short-term reflex model parameters fitted to canines can be used in humans. If  $\lambda_3$ , the parameter that controls the magnitude of SBV change (**Equation 2.12**), was larger, then we would see a larger decrease in SBV for the same increase in MAP. The same can be said about  $\lambda_1$  because the change in  $R_{as}$  is very minimal from baseline to acute even though CO increases by a relatively large amount.

To create our calibration curve that converts patient RF to MVBR, we assumed that changes in pressure did not affect the conversion. However, flow across the mitral valve is affected by resistance and change in pressures during systole and diastole. If any of the patients

have very large or small changes in pressures throughout the cardiac cycle, then we would be inaccurately prescribing MVBR using our calibration curve.

Overall, our modeling framework shows promise for modeling LV growth in MitraClip patients; however, further improvements on patient specific parameter estimation and on the coupled reflex model is necessary to capture patient specific responses. Future work includes modeling all the patients in our dataset. By developing a reflex model that can predict hemodynamics necessary for LV growth modeling, we set the framework for expanding our modeling framework to guide patient specific therapies in other disease states such as left bundle branch block. Oomen et al. previously showed that the rapid-computational model can be used to improve cardiac resynchronization therapy, and coupling our reflex model may allow for better patient-specific predictions since hemodynamics regulation plays a major role in LV growth [20].

## 5 CHAPTER 5: CONCLUSIONS AND FUTURE DIRECTIONS

The goal of this thesis was to develop a computational modeling framework to predict hemodynamics and LV growth during pressure and volume overload in both canines and humans. Our lab and others have shown that accurate hemodynamic predictions are essential for modeling LV growth [18], [26], [28], [30]. However, up to this point our computational modeling framework has been limited to only retrospective simulations of LV growth due the absence of hemodynamic predictions—both short and long-term hemodynamic changes had to be fitted to or prescribed from previously recorded experimental data. Therefore, this thesis focused on (Chapter 2) modeling the baroreceptors to predict short-term hemodynamic changes, (Chapter 3) modeling the renin-angiotensin II to predict long-term hemodynamic changes, and (Chapter 4) using the short- and long-term reflex models coupled to our rapid-computational growth model to predict regression of LV hypertrophy in patients who have undergone MitraClip treatment.

### 5.1 SHORT-TERM REFLEX MODELING

In Chapter 2, we developed and tested three different short-term hemodynamic models to predict hemodynamic changes from baseline to acute following the onset of simulated pressure or volume overload. The models varied in physiological detail, and we analyzed the pros and cons of each modeling approach. We did not develop a short-term hemodynamic model that was successfully validated against multiple experimental canine studies for pressure and volume overload. However, we did conclude that the phenomenological short-term reflex model predicted necessary changes in hemodynamics (via changes in SBV and  $R_{as}$ ) to match acute state experimental data in one pressure and one volume overload study.

For future work, we aim to continue improving both the physiologically detailed and phenomenological short-term reflex models to model several pressure and volume overload cases. For the phenomenological short-term reflex model, we already showed a simplified system can predict short-term hemodynamic changes. The upper and lower bounds we set on SBV, HR, and  $R_{as}$  changes were determined based on maximum and minimum values observed in our datasets and exploratory analysis with the rapid-computational model. We would like to set the bounds on SBV and  $R_{as}$  based on the maximum amount a blood vessel can dilate or constrict. *In vitro* experiments can be conducted to determine these bounds. In addition, we fitted one of the exponential decay parameters,  $\lambda_4$ , to match step changes in MAP; however, we did not fit the other exponential decay parameter,  $\lambda_2$ , to match experimental changes in CO. Since CO is determined by HR and stroke volume, we would like to match  $\lambda_2$  to match experimental studies

where HR or stroke volume are controlled, and baroreceptor activity is measured. Since  $R_{as}$  is adapted based on CO, a more accurate  $\lambda_2$  may provide better adaptation of  $R_{as}$ .

Although we can fine tune the phenomenological short-term reflex model to improve predictions in the Nakano et al. and Nagaotmo et al. studies, there is more potential in improving the physiologically detailed short-term reflex models. We likely need to find better ways to fit the baroreflex parameters originally fitted by Beard et al. A balance between a detailed baroreceptor response and minimal ODEs/parameters can be found to best describe the necessary hemodynamic adaptation for the rapid-computational growth model. For the physiologically detailed capacitance-controlled model, we only adapted the arterial capacitances; however, since much of the blood is on the venous side, we would like to adapt venous capacitance to simulate constriction. This may allow us to better match the experimental pressure and volume overload studies we couldn't match.

## 5.2 LONG-TERM REFLEX MODELING

In [Chapter 3](#), we developed a long-term reflex system that adapts blood volumes based on changes in MAP. Compared to manually prescribing hemodynamics throughout growth, the model predicted the evolution of LV volumes and pressures. In the Kleaveland et al. study, where experimental aortic pressures were available, the model predicted MAP well. In the Nakano et al. study, the model had trouble predicting EDP and systolic arterial pressure; however, there was error at the acute state that likely contributed to the long-term reflex model predicting the pressures accurately. The coupled reflex and rapid-computational model predicted eccentric growth well, but had some trouble predicted end diastolic wall thickening (concentric growth).

For future work, we aim to develop more physiologically detailed long-term reflex systems to run a similar comparison analysis like we did with the short-term reflex models. Beard et al. relates the renin-angiotensin II activity and sympathetic tone to adapt peripheral resistance through the system [33]. We discussed earlier in section 3.1 that, on the long-term scale, total peripheral resistance has small effects on CO [39], and we decided not to adapt  $R_{as}$  in the long-term reflex model. Total peripheral resistance is still known to change, and Beard et al. adapts total peripheral resistance based on angiotensin II and sympathetic tone which is determined by a time average arterial pressure. Including this mechanism in our long-term reflex model may help better match some of the radial growth that we underestimated in the Sasayama et al. and Kleaveland et al. studies. In addition, adapting  $R_{as}$  in the long-term system may help improve growth predictions in our Chapter 4 patient study.

In our long-term reflex model, we did not model neurohumoral control of pressure diuresis/natriuresis. Body-fluid volume is heavily regulated by the pressure-diuresis relationship, and we can incorporate it into our system similar to how Beard et al. does it. We can have volume leave the system based on urine output that is governed by changes in MAP and the pressure-

diuresis relationship [33]. This would be an alternative way to control blood volumes compared to SBV adaptation. The downside of using more detailed systems like Beard et al. is that we would be adding more parameters and complications to the model. Simplified, fast computational models are vital in prospective time-sensitive patient modeling [23].

As earlier described in section 3.4, we would like to couple a physiologically detailed long-term reflex model with Estrada et al's cell signaling network model. The cell signaling network already includes angiotensin-II activity; thus, we can directly couple our reflex model with the cell signaling network model to consider hormonal inputs to better predict hemodynamics and improve prospective LV growth modeling.

### 5.3 MITRACLIP PATIENT-SPECIFIC MODELING

In [Chapter 4](#), we used our coupled reflex and rapid-computational growth model to predict patient-specific cardiac reverse growth in patients who underwent MitraClip treatment for MR. Following MitraClip implantation, patients are expected to have reversal of eccentric growth where LV cavity diameter and EDVI decrease. Our modeling framework was able to predict the decrease in EDVI in three patients; however, we were not able to predict the magnitude of decrease in EDVI. In addition, we were not able to accurately predict the decrease in end-diastolic wall thickening that was observed in these patients. Due to limited clinical data availability, we had difficulty prescribing a patient specific ESPVR and EDVPR which likely contributed to not fully predicting reversal of radial and fiber growth.

As described in section 4.4, we aim to use the single-beat method [61] to estimate LV elastance to develop patient specific ESPVRs. A more accurate ESPVR may help us better estimate pre and post end systolic volumes. In addition, we aim to create patient specific EDPVRs that better match dilated hearts and patient body mass. We can scale the Burkhoff and Tyber EDPVR material parameters ( $A$  and  $B$ ) based on each patient's cardiac geometry using the following radiological measurements: end-diastolic wall thickness, LV cavity diameter at end-diastole, and body surface area. In our mitral valve disease patients, we would expect that taking these measurements into consideration would lead to a 'flatter' EDPVR, which would result in smaller post EDVIs and larger pre EDVIs. This would result in larger magnitudes of reverse eccentric growth, which was observed in the patient dataset.

Although we cannot fully match experimental patient data, our modeling efforts highlight the potential of prospective patient specific modeling. As observed by the experimental patient data (**Figure 4.2**), patient responses vary on the individual level. Our modeling framework is able to predict different degrees of LV growth between individual patients with different changes of wall thickness, volumes, and arterial pressures. Our model also outputs PV loops at every step of growth for 12 months following MitraClip implantation. PV loops provide vital information about cardiac function that cannot be obtained in the clinic without continuous invasive measurements.

For example, before patient 23 even receives MitraClip treatment, a clinician may look at the PV loops (**Figure 4.4B**) and suggest a treatment plan for the increase in systolic pressures predicted by the model to occur months after surgery. Clinicians can use these detailed predictions to create individual treatments for patients that would not have been possible with only clinical measurements available.

In the future, we aim to expand our reflex and growth modeling framework to include hormonal signals. The growth law we used assumes that growth is driven by only mechanics; however, Estrada et al. previously showed that hormones play a role in driving concentric LV growth. Hormones have been shown to play a role in the progression of volume overload and HF [62], and they likely play a role in influencing reversal of eccentric LV growth. A cell signaling network model like the one employed in Estrada et al. also includes angiotensin II signaling, thus accommodating predicting changes in growth as well as hemodynamics. In addition, coupling our reflex and growth framework to a cell signaling network will allow us to simulate medications patients may be taking or medications a clinician may want to prescribe. Hormonal changes due to medications were overlooked in this thesis when modeling the MitraClip patients. Capturing the hormonal changes may allow us to better predict MitraClip patient cardiac conditions months after implantation.

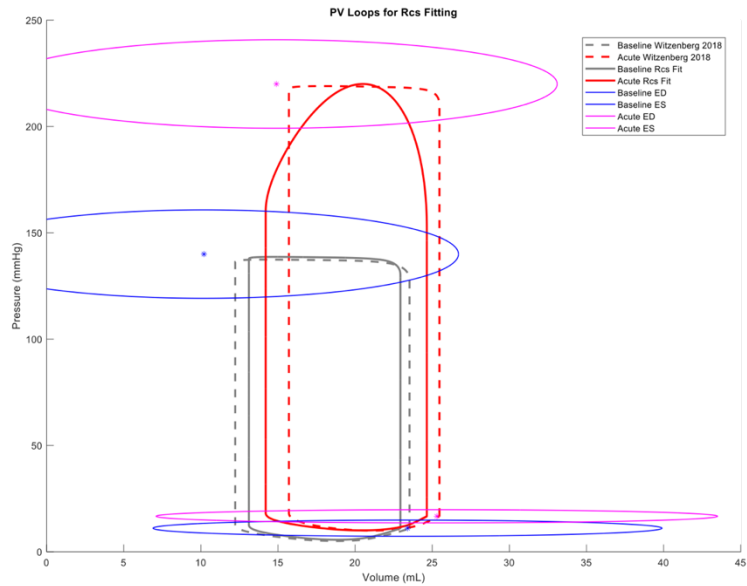
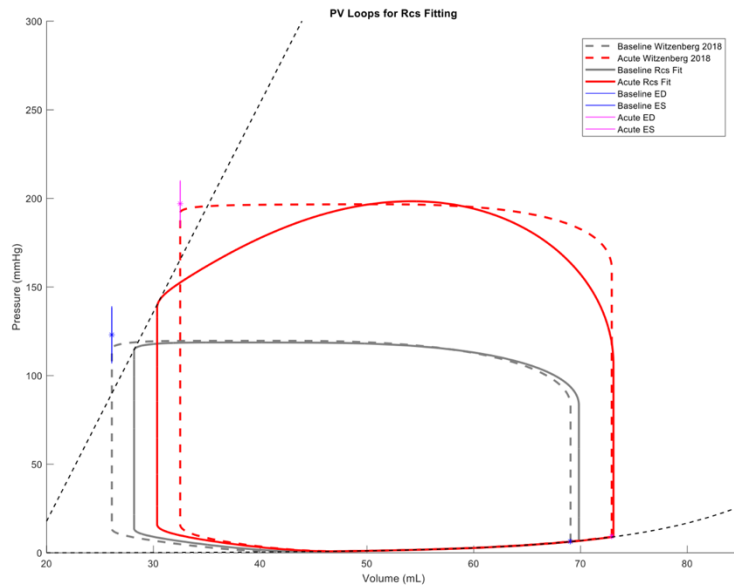
Overall, this thesis contributed to cardiac growth modeling in pressure and volume overload by incorporating reflex systems in the modeling framework. Prospective computational models are necessary to create patient-specific treatments, which can help clinicians better treat and prevent HF.

## 6 APPENDICES

### 6.1 APPENDIX A

**Table A.1:** Depicted in the table are the refitted rapid-computational model parameters such that pressure overload is induced by increasing  $R_{cs}$  and volume overload is induced by decreasing MVBR.  $R_{as}$  is kept constant from baseline to acute. Fitting error is computed based on the cost functions described in Witzenburg and Holmes [18] supplementary material. Baseline  $R_{cs}$  is set to 0.023 for all simulations.

|  | Sasayama et al. Pressure Overload [8] | Nagatomo et al. Pressure Overload[11] | Kleaveland et al. Volume Overload [9] | Nakano et al. Volume Overload [10] |
|--|---------------------------------------|---------------------------------------|---------------------------------------|------------------------------------|
| <b><u>Fitted Parameter</u></b>               |                                       |                                       |                                       |                                    |
| <b>A</b> (mL)                                | 0.3227                                | 0.0688                                | 0.2363                                | 0.0655                             |
| <b>B</b> (mmHg)                              | 0.2322                                | 0.0894                                | 0.1082                                | 0.0895                             |
| <b>V<sub>0</sub></b> (mL)                    | 7.5751                                | 18.4888                               | 14.1098                               | 17.9531                            |
| <b>E</b> (mmHg/mL)                           | 24.8778                               | 11.8049                               | 17.8673                               | 22.4417                            |
| <b>Baseline R<sub>as</sub></b> (mmHg * s/mL) | 8.0297                                | 1.5704                                | 2.1027                                | 2.0517                             |
| <b>Baseline SBV</b> (mL)                     | 308.6214                              | 369.6318                              | 369.6616                              | 334.9921                           |
| <b>Acute R<sub>cs</sub></b> (mmHg * s/mL)    | 0.3562                                | 0.1000                                | <i>same as baseline</i>               | <i>same as baseline</i>            |
| <b>Acute SBV</b> (mL)                        | 389.1055                              | 440.3870                              | 348.9924                              | 383.2973                           |
| <b>Acute MVBR</b> (mmHg * s/mL)              | n/a                                   | n/a                                   | 0.8570                                | 0.1086                             |
| Fitting Error                                | 0.0396                                | 1.206                                 | 0.668                                 | 4.187                              |

**A****B**

**Figure A.1:** **A:** Depicted are the refitted PV loops for Sasayama et al. [8] pressure overload. **B:** Depicted are the refitted PV loops for Nagatomo et al. [11] pressure overload. Experimental data from Sasayama et al. and Nagatomo et al are shown in the blue and pink ellipses.  $R_{cs}$  is increased from baseline to acute and  $R_{as}$  is kept constant. The dotted PV loops are generated from Witzenberg and Holmes's [18] original rapid-computational model.

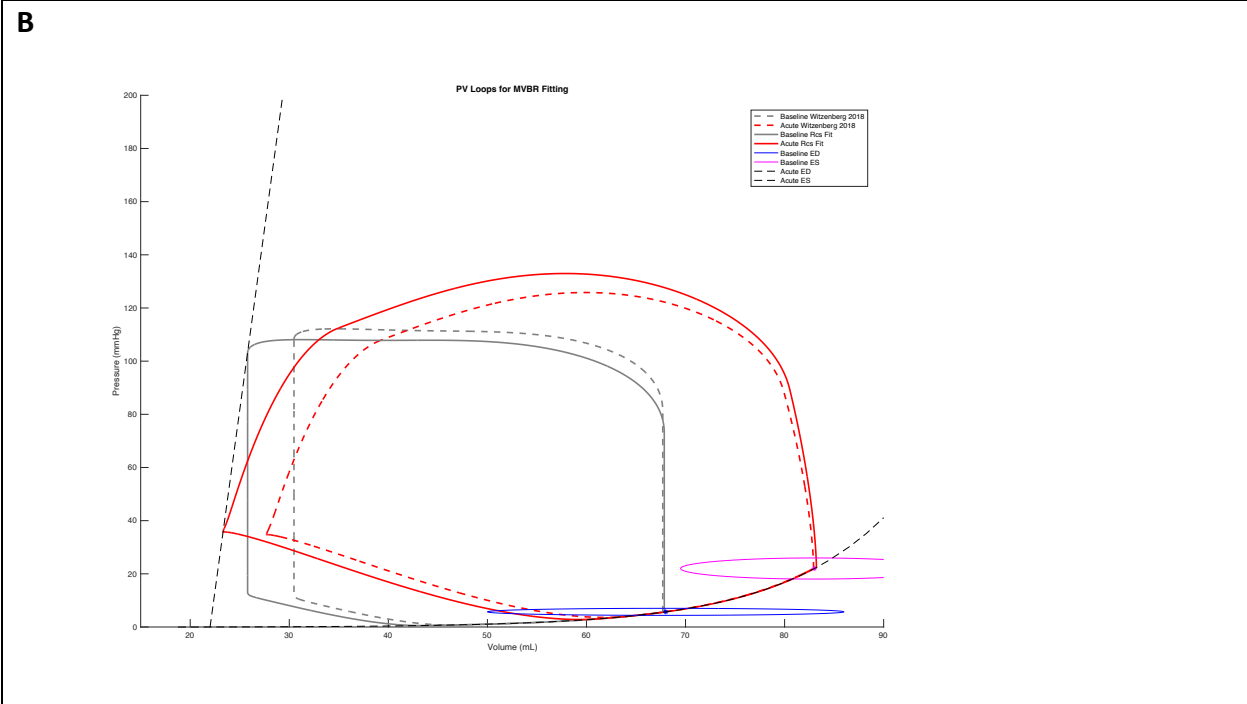
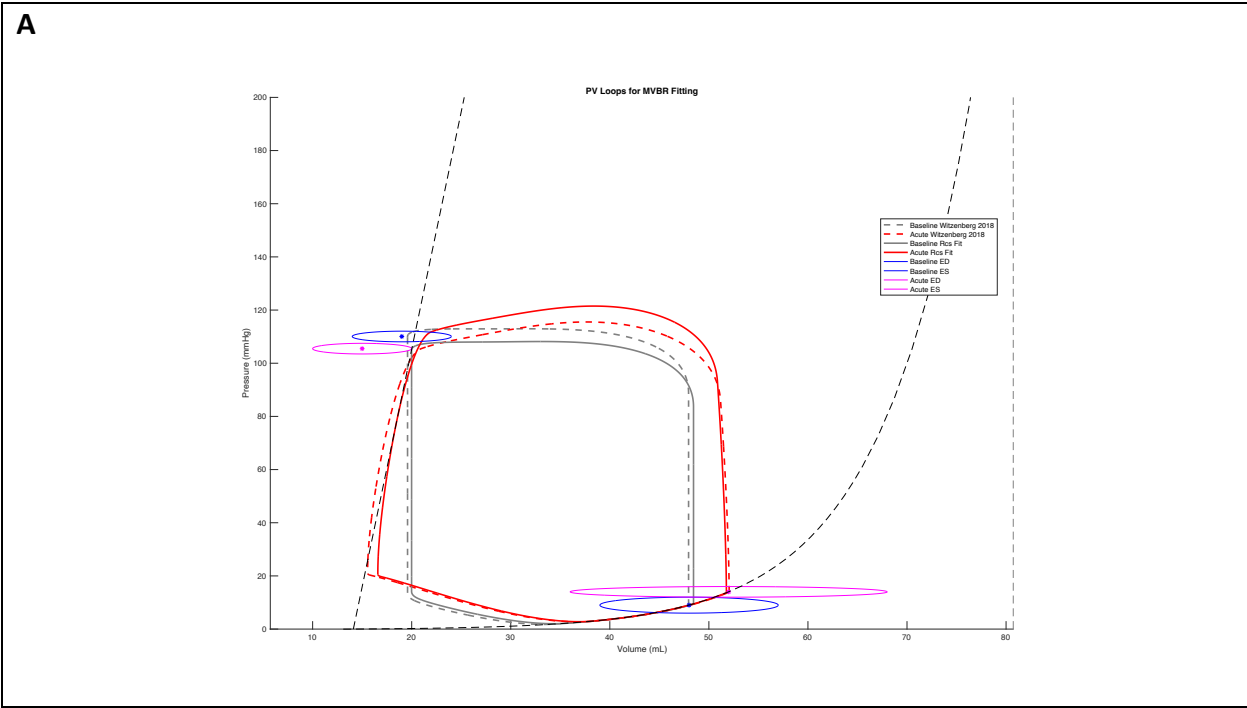


**Figure A.2: A:** Depicted are the refitted PV loops for Kleavland et al. [9] volume overload. **B:** Depicted are the refitted PV loops for Nakano et al. [10] volume overload. Experimental data from Kleavland et al. and Nakano et al are shown in the blue and pink ellipses. MVBR is decreased from baseline to acute and  $R_{as}$  is kept constant. The dotted PV loops are generated from Witzenberg and Holmes's [18] original rapid-computational model.

## 6.2 APPENDIX B

$$\begin{aligned}
 cost_{func} = & \left( \frac{maxLVP_{acute,POmodel} - maxLVP_{acute,Sasayama}}{SDmaxLVP_{acute,Sasayama}} \right)^2 \\
 & + \left( \frac{EDP_{acute,POmodel} - EDP_{acute,Sasayama}}{SDEDP_{acute,Sasayama}} \right)^2 \\
 & + \left( \frac{ESV_{acute,POmodel} - ESV_{acute,Sasayama}}{SDESV_{acute,Sasayama}} \right)^2 \\
 & + \left( \frac{EDV_{acute,POmodel} - EDV_{acute,Sasayama}}{SDEDV_{acute,Sasayama}} \right)^2
 \end{aligned}$$

Equation B.1

$$\begin{aligned}
 cost_{func} = & \left( \frac{MAP_{acute,VOmodel} - MAP_{acute,Kleveland}}{SDMAP_{acute,Kleveland}} \right)^2 \\
 & + \left( \frac{EDP_{acute,VOmodel} - EDP_{acute,Kleveland}}{SDEDP_{acute,Kleveland}} \right)^2 \\
 & + \left( \frac{minV_{acute,VOmodel} - minV_{acute,Kleveland}}{SDminV_{acute,Kleveland}} \right)^2 \\
 & + \left( \frac{RF_{acute,VOmodel} - RF_{acute,Kleveland}}{SDRF_{acute,Kleveland}} \right)^2
 \end{aligned}$$

Equation B.2

$$\begin{aligned}
 cost_{func} = & \left( \frac{EDP_{acute,VOmodel} - EDP_{acute,Nakano}}{SDEDP_{acute,Nakano}} \right)^2 \\
 & + \left( \frac{sysP_{acute,VOmodel} - sysP_{acute,Nakano}}{SDsysP_{acute,Nakano}} \right)^2 \\
 & + \left( \frac{EF_{acute,VOmodel} - EF_{acute,Nakano}}{SDEF_{acute,Nakano}} \right)^2 \\
 & + \left( \frac{RF_{acute,VOmodel} - RF_{acute,Nakano}}{SDRF_{acute,Nakano}} \right)^2
 \end{aligned}$$

Equation B.3

$$\begin{aligned}
 cost_{func} = & \left( \frac{EDP_{acute,POmodel} - EDP_{acute,Nagatomo}}{SDEDP_{acute,Nagatomo}} \right)^2 \\
 & + \left( \frac{maxLVP_{acute,POmodel} - maxLVP_{acute,Nagatomo}}{SDmaxLVP_{acute,Nagatomo}} \right)^2 \\
 & + \left( \frac{ESV_{acute,POmodel} - ESV_{acute,Nagatomo}}{SDESV_{acute,Nagatomo}} \right)^2 \\
 & + \left( \frac{SV_{acute,POmodel} - SV_{acute,Nagatomo}}{SDSV_{acute,Nagatomo}} \right)^2
 \end{aligned}$$

Equation B.4

**Table B.1:** Note: Parameter values that are fitted (when applicable) to match acute state hemodynamics using detailed hemodynamic short-term reflex system. Fitting for Sasayama et al. Pressure overload w/out capacitance control is shown in blue. Fitting for Nakano et al. Volume Overload w/ Capacitance control is shown in orange. No shading means that the same value was used in all simulations.

| <u>Value</u>                                      |                                    | <u>Description</u>                                 | <u>Source</u>  |
|---|------------------------------------|--|--|
| <b>Time Step</b>                                  |                                    |  |  |
| $dt = 1.5$ mins                                   |                                    |  |  |
| <b>Baroreceptor Firing</b>                        |                                    |  |  |
| $V_{U,AsO} = 90.5$ mL                             | $V_{U,AsO} = 97.34$                | UBV in the systemic arteries                       | Calculated   |
| $C_{as} = 1.02$                                   |                                    | Systemic Arterial Capacitance                      | [18]   |
| $T_C = 23.02$                                     |                                    | Total Capacitance                                  | Calculated   |
| $TBV = 2042.3$ mL                                 | $TBV = 2241$ mL                    | Total Blood Volume                                 | Calculated   |
| $V_{OLV}, V_{ORV} = 7.58$ mL                      | $V_{OLV}, V_{ORV} = 22$ mL         | Initial Volume in the LV and RV                    | $R_{cs}$ Induced Pressure Overload Rapid-computational Growth Model for Sasayama et al. or Nakano et al. |
| $\tau_S = 120.5$ min                              | $\tau_S = 150$ min                 | Baroreceptor Time Constant                         | Fitted   |
| $f_0 = 299.8 * 60 * \tau_{gain} \text{ min}^{-1}$ |                                    | Baroreceptor Gain Constant                         | [33]   |
| $a = 0.0651 * 60 * \tau_{gain} \text{ min}^{-1}$  |                                    | Baroreceptor Activation Rate                       | [33]   |
| $b = 0.2004 * 60 * \tau_{gain} \text{ min}^{-1}$  |                                    | Baroreceptor Deactivation Rate                     | [33]   |
| $\delta_0 = 0.4965 * \tau_{baro}$                 |                                    | Baroreceptor Saturation Rate                       | [33]   |
| $\tau_{gain} = 8.1e-05$                           | $\tau_{gain} = 1.5e-05$            | Baroreceptor Gain Adjustment Factor                | Fitted   |
| $\tau_{baro} = 0.01591$                           | $\tau_{baro} = 0.0474$             | Baroreceptor Rate and Saturation Adjustment Factor | Fitted   |
| <b>Sympathetic Tone Control</b>                   |                                    |  |  |
| $f_{SN} = 0.27801 \text{ min}^{-1}$               | $f_{SN} = 0.0311 \text{ min}^{-1}$ | Baroreceptor Arc Parameter                         | Fitted   |
| <b>SBV &amp; HR</b>                               |                                    |  |  |
| $H_1 = 110$ beats/min                             | $H_1 = 110$ beats/min              | Adjustable HR Parameter                            | Calculated   |
| $SBV_1 = 400$ mL                                  | $SBV_1 = n/a$                      | Adjustable SBV Parameter                           | Calculated   |
| $Ras_1 = n/a$                                     | $Ras_1 = 4.8875$                   | Adjustable SBV Parameter                           | Calculated   |

### 6.3 APPENDIX C

$$\begin{aligned}
 cost_{func} = & \left( \frac{\max P_{acute, P0model} - \max P_{acute, Sasayama}}{SD\max P_{acute, Sasayama}} \right)^2 \\
 & + \left( \frac{EDP_{acute, P0model} - EDP_{acute, Sasayama}}{SDEDP_{acute, Sasayama}} \right)^2 \\
 & + \left( \frac{ESV_{acute, P0model} - ESV_{acute, Sasayama}}{SDESV_{acute, Sasayama}} \right)^2 \\
 & + \left( \frac{EDV_{acute, P0model} - EDV_{acute, Sasayama}}{SDEDV_{acute, Sasayama}} \right)^2 \\
 & + \left( \frac{MAP_{acute, V0model} - MAP_{acute, Kleaveland}}{SDMAP_{acute, Kleaveland}} \right)^2 \\
 & + \left( \frac{EDP_{acute, V0model} - EDP_{acute, Kleaveland}}{SDEDP_{acute, Kleaveland}} \right)^2 \\
 & + \left( \frac{\min V_{acute, V0model} - \min V_{acute, Kleaveland}}{SD\min V_{acute, Kleaveland}} \right)^2 \\
 & + \left( \frac{RF_{acute, V0model} - RF_{acute, Kleaveland}}{SDRF_{acute, Kleaveland}} \right)^2
 \end{aligned}
 \tag{Equation C.1}$$

**Table C.1:** Depicted in the table are the high-level short term reflex parameter values when the model was fitted to various experimental studies. During fitting,  $\lambda_1$  and  $\lambda_2$  were constrained from 0 to 10 and  $\lambda_3$  was constrained from 0.001 to 10 to help speed up fitting.  $\lambda_4$  was fitted to Chapleau et al. [34] prior to fitting the other parameters to the pressure and volume overload studies. The green column shows the best fitting scenario. The cost functions for Sasayama et al. and Kleaveland et al. are derived from **Appendix Equation C.1**. The cost functions for Nakano et al. and Nagatomo et al. are shown from **Appendix Equation B.3** and **Appendix Equation B.4**, respectively.

| Parameter   | Experimental Studies Short-Term Reflex Model was Fitted Against |   |  |                                       |   |
|-------------|---|---|--|---------------------------------------|---|
|             | Sasayama et al. [8]<br>Pressure Overload                        | Nagatomo et al. [11]<br>Pressure Overload | Kleaveland et al. [9]<br>Volume Overload | Nakano et al. [10]<br>Volume Overload | Sasayama et al. [8] +<br>Kleaveland et al. [9] Pressure & Volume Overload |
| $\lambda_1$ | 0.9291  | 4.4361                                    | 1.3006                                   | 3.3321                                | 1.2364  |
| $\lambda_2$ | 0.8358  | 3.1731                                    | 0.7990                                   | 10.000                                | 0.7677  |
| $\lambda_3$ | 1.7775  | 0.0010                                    | 2.6479                                   | 3.2605                                | 2.6749  |
| $\lambda_4$ | 1.1734  |   |  |                                       |   |

**Table C.2:** Depicted in the table are the cost function values when the high-level short term reflex model was fitted to and validated against various experimental studies. The cost functions for Sasayama et al. and Kleaveland et al. are derived from **Appendix Equation C.1**. The cost functions for Nakano et al. and Nagatomo et al. are shown from **Appendix Equation B.3** and **Appendix Equation B.4**, respectively. A maximum error of 10000 was assigned to the cost function when the rapid-computational model crashed, the RK4 solver in the rapid-computational model maxed out its iterations, or a negative  $R_{as}$  or SBV was reported.

|                    |   | Fitting Studies                          |   |  |                                       |   |
|--------------------|---|--|---|--|---------------------------------------|---|
|                    |   | Sasayama et al. [8]<br>Pressure Overload | Nagatomo et al. [11]<br>Pressure Overload | Kleaveland et al. [9]<br>Volume Overload | Nakano et al. [10]<br>Volume Overload | Sasayama et al. [8] +<br>Kleaveland et al. [9]<br>Pressure &<br>Volume Overload |
| Validation Studies | Sasayama et al. [8]<br>Pressure Overload  | 0.60152                                  | 10000                                     | 1.3814                                   | 10000                                 | 0.6089  |
|                    | Nagatomo et al. [11]<br>Pressure Overload | 10000                                    | 14.0892                                   | 10000                                    | 10000                                 | 10000   |
|                    | Kleaveland et al. [9]<br>Volume Overload  | 0.15509                                  | 2.6678                                    | 0.10662                                  | 10000                                 | 0.12215   |
|                    | Nakano et al. [10]<br>Volume Overload     | 8.8086                                   | 14.9858                                   | 67.5084                                  | 2.5849                                | 8.8556  |

## 6.4 APPENDIX D

$$\begin{aligned}
 cost_{func} = & \left( \frac{day9\_maxP_{acute, P0model} - day9\_maxP_{acute, Sasayama}}{day9\_SDmaxP_{acute, Sasayama}} \right)^2 \\
 & + \left( \frac{day9\_EDP_{acute, P0model} - day9\_EDP_{acute, Sasayama}}{day9\_SDEDP_{acute, Sasayama}} \right)^2 \\
 & + \left( \frac{day9\_ESV_{acute, P0model} - day9\_ESV_{acute, Sasayama}}{day9\_SDESV_{acute, Sasayama}} \right)^2 \\
 & + \left( \frac{day9\_EDV_{acute, P0model} - day9\_EDV_{acute, Sasayama}}{day9\_SDEDV_{acute, Sasayama}} \right)^2 \\
 & + \left( \frac{day9\_maxP_{acute, P0model} - day9\_maxP_{acute, Sasayama}}{day9\_SDmaxP_{acute, Sasayama}} \right)^2 \\
 & + \left( \frac{day18\_EDP_{acute, P0model} - day18\_EDP_{acute, Sasayama}}{day18\_SDEDP_{acute, Sasayama}} \right)^2 \\
 & + \left( \frac{day18\_ESV_{acute, P0model} - day18\_ESV_{acute, Sasayama}}{day18\_SDESV_{acute, Sasayama}} \right)^2 \\
 & + \left( \frac{day18\_EDV_{acute, P0model} - day18\_EDV_{acute, Sasayama}}{day18\_SDEDV_{acute, Sasayama}} \right)^2 \\
 & + \left( \frac{month1\_MAP_{acute, V0model} - month1\_MAP_{acute, Kleaveland}}{month1\_SDMAP_{acute, Kleaveland}} \right)^2 \\
 & + \left( \frac{month1\_EDP_{acute, V0model} - month1\_EDP_{acute, Kleaveland}}{month1\_SDEDP_{acute, Kleaveland}} \right)^2 \\
 & + \left( \frac{month1\_minV_{acute, V0model} - month1\_minV_{acute, Kleaveland}}{month1\_SDminV_{acute, Kleaveland}} \right)^2 \\
 & + \left( \frac{month3\_MAP_{acute, V0model} - month3\_MAP_{acute, Kleaveland}}{month3\_SDMAP_{acute, Kleaveland}} \right)^2 \\
 & + \left( \frac{month3\_EDP_{acute, V0model} - month3\_EDP_{acute, Kleaveland}}{month3\_SDEDP_{acute, Kleaveland}} \right)^2 \\
 & + \left( \frac{month3\_minV_{acute, V0model} - month3\_minV_{acute, Kleaveland}}{month3\_SDminV_{acute, Kleaveland}} \right)^2
 \end{aligned}$$

Equation  
D.1

## 6.5 APPENDIX E

$$\begin{aligned} cost_{func} = & (EDP_{baseline,model} - EDP_{baseline,patient})^2 \\ & + (EDVI_{baseline,model} - EDVI_{baseline,patient})^2 \\ & + (minVoll_{baseline,model} - minVoll_{baseline,patient})^2 \\ & + (MAP_{baseline,model} - MAP_{baseline,patient})^2 \\ & + (RF_{baseline,model} - RF_{baseline,patient})^2 \\ & + (meanPAP_{baseline,model} - meanPAP_{baseline,patient})^2 \end{aligned} \quad \begin{array}{l} \text{Equation} \\ \text{E.1} \end{array}$$

$$LV \text{ Wall Volume} = \frac{4}{3\pi} \left( \left( LVPWd + \frac{LVIDd}{2} \right)^3 - \left( \frac{LVIDd}{2} \right)^3 \right) \quad \begin{array}{l} \text{Equation} \\ \text{E.2} \end{array}$$

## 7 REFERENCES

- [1] S. Komanduri, Y. Jadhao, S. S. Guduru, P. Cheriyaath, and Y. Wert, "Prevalence and risk factors of heart failure in the USA: NHANES 2013 – 2014 epidemiological follow-up study," *J. Community Hosp. Intern. Med. Perspect.*, vol. 7, no. 1, pp. 15–20, Mar. 2017, doi: 10.1080/20009666.2016.1264696.
- [2] D. Levy *et al.*, "Long-Term Trends in the Incidence of and Survival with Heart Failure," *N. Engl. J. Med.*, vol. 347, no. 18, pp. 1397–1402, Oct. 2002, doi: 10.1056/NEJMoa020265.
- [3] P. A. Heidenreich *et al.*, "Forecasting the impact of heart failure in the United States: a policy statement from the American Heart Association," *Circ. Heart Fail.*, vol. 6, no. 3, pp. 606–619, May 2013, doi: 10.1161/HHF.0b013e318291329a.
- [4] A. A. Inamdar and A. C. Inamdar, "Heart Failure: Diagnosis, Management and Utilization," *J. Clin. Med.*, vol. 5, no. 7, p. 62, Jun. 2016, doi: 10.3390/jcm5070062.
- [5] F. R. Heinzel, F. Hohendanner, G. Jin, S. Sedej, and F. Edelmann, "Myocardial Hypertrophy and Its Role in Heart Failure with Preserved Ejection Fraction," *J. Appl. Physiol. Bethesda Md* 1985, vol. 119, no. 10, pp. 1233–1242, Nov. 2015, doi: 10.1152/japplphysiol.00374.2015.
- [6] J. R. Weber, "Left ventricular hypertrophy: its prime importance as a controllable risk factor," *Am. Heart J.*, vol. 116, no. 1 Pt 2, pp. 272–279, Jul. 1988, doi: 10.1016/0002-8703(88)90100-7.
- [7] C. M. Witzenburg and J. W. Holmes, "A Comparison of Phenomenologic Growth Laws for Myocardial Hypertrophy," *J. Elast.*, vol. 129, no. 1–2, pp. 257–281, Dec. 2017, doi: 10.1007/s10659-017-9631-8.
- [8] S. Sasayama, J. Ross, D. Franklin, C. M. Bloor, S. Bishop, and R. B. Dille, "Adaptations of the left ventricle to chronic pressure overload.," *Circ. Res.*, vol. 38, no. 3, pp. 172–178, Mar. 1976, doi: 10.1161/01.RES.38.3.172.
- [9] J. P. Kleaveland, W. G. Kussmaul, T. Vinciguerra, R. Ditters, and B. A. Carabello, "Volume overload hypertrophy in a closed-chest model of mitral regurgitation," *Am. J. Physiol.-Heart Circ. Physiol.*, vol. 254, no. 6, pp. H1034–H1041, Jun. 1988, doi: 10.1152/ajpheart.1988.254.6.H1034.
- [10] K. Nakano *et al.*, "Depressed contractile function due to canine mitral regurgitation improves after correction of the volume overload.," *J. Clin. Invest.*, vol. 87, no. 6, pp. 2077–2086, Jun. 1991, doi: 10.1172/JCI115238.
- [11] Y. Nagatomo, B. A. Carabello, M. Hamawaki, S. Nemoto, T. Matsuo, and P. J. McDermott, "Translational mechanisms accelerate the rate of protein synthesis during canine pressure-overload hypertrophy," *Am. J. Physiol.-Heart Circ. Physiol.*, vol. 277, no. 6, pp. H2176–H2184, Dec. 1999, doi: 10.1152/ajpheart.1999.277.6.H2176.

- [12] M. R. Dweck *et al.*, “Left ventricular remodeling and hypertrophy in patients with aortic stenosis: insights from cardiovascular magnetic resonance,” *J. Cardiovasc. Magn. Reson.*, vol. 14, no. 1, p. 50, Jul. 2012, doi: 10.1186/1532-429X-14-50.
- [13] C. Muhl, W. R. M. Dassen, and H. Kuipers, “Cardiac remodelling: concentric versus eccentric hypertrophy in strength and endurance athletes,” *Neth. Heart J.*, vol. 16, no. 4, pp. 129–133, Apr. 2008.
- [14] A. C. Estrada, K. Yoshida, J. J. Saucerman, and J. W. Holmes, “A multiscale model of cardiac concentric hypertrophy incorporating both mechanical and hormonal drivers of growth,” *Biomech. Model. Mechanobiol.*, vol. 20, no. 1, pp. 293–307, Feb. 2021, doi: 10.1007/s10237-020-01385-6.
- [15] Å. E. Rieck *et al.*, “Hypertension in Aortic Stenosis,” *Hypertension*, vol. 60, no. 1, pp. 90–97, Jul. 2012, doi: 10.1161/HYPERTENSIONAHA.112.194878.
- [16] D. Huber and H. P. Krayenbuehl, “Determinants of ejection performance in aortic stenosis,” vol. 64, no. 1, p. 9, 1981.
- [17] G. J. Scuderi and J. Butcher, “Naturally Engineered Maturation of Cardiomyocytes,” *Front. Cell Dev. Biol.*, vol. 5, 2017, Accessed: Feb. 27, 2022. [Online]. Available: <https://www.frontiersin.org/article/10.3389/fcell.2017.00050>
- [18] C. M. Witzenburg and J. W. Holmes, “Predicting the time course of ventricular dilation and thickening using a rapid compartmental model,” *J Cardiovasc. Transl. Res.*, vol. 11, no. 2, pp. 109–122, Apr. 2018, doi: 10.1007/s12265-018-9793-1.
- [19] K. Yoshida, A. D. McCulloch, J. H. Omens, and J. W. Holmes, “Predictions of hypertrophy and its regression in response to pressure overload,” *Biomech. Model. Mechanobiol.*, vol. 19, no. 3, pp. 1079–1089, Jun. 2020, doi: 10.1007/s10237-019-01271-w.
- [20] P. J. A. Oomen, T.-K. N. Phung, S. H. Weinberg, K. C. Bilchick, and J. W. Holmes, “A rapid electromechanical model to predict reverse remodeling following cardiac resynchronization therapy,” *Biomech. Model. Mechanobiol.*, vol. 21, no. 1, pp. 231–247, Feb. 2022, doi: 10.1007/s10237-021-01532-7.
- [21] S. Lazam *et al.*, “Twenty-Year Outcome After Mitral Repair Versus Replacement for Severe Degenerative Mitral Regurgitation,” *Circulation*, vol. 135, no. 5, pp. 410–422, Jan. 2017, doi: 10.1161/CIRCULATIONAHA.116.023340.
- [22] K. Yoshida and J. W. Holmes, “Computational models of cardiac hypertrophy,” *Prog. Biophys. Mol. Biol.*, vol. 159, pp. 75–85, Jan. 2021, doi: 10.1016/j.pbiomolbio.2020.07.001.
- [23] J. W. Holmes and J. Lumens, “Clinical Applications of Patient-Specific Models: The Case for a Simple Approach,” *J Cardiovasc. Transl. Res.*, vol. 11, no. 2, pp. 71–79, Apr. 2018, doi: 10.1007/s12265-018-9787-z.
- [24] E. Rondanina and P. H. M. Bovendeerd, “Evaluation of stimulus-effect relations in left ventricular growth using a simple multiscale model,” *Biomech. Model. Mechanobiol.*, vol. 19, no. 1, pp. 263–273, Feb. 2020, doi: 10.1007/s10237-019-01209-2.

- [25] E. K. Rodriguez, A. Hoger, and A. D. McCulloch, "Stress-dependent finite growth in soft elastic tissues," *J. Biomech.*, vol. 27, no. 4, pp. 455–467, Apr. 1994, doi: 10.1016/0021-9290(94)90021-3.
- [26] R. C. P. Kerckhoffs, J. H. Omens, and A. D. McCulloch, "A single strain-based growth law predicts concentric and eccentric cardiac growth during pressure and volume overload," *Mech. Res. Commun.*, vol. 42, pp. 40–50, Jun. 2012, doi: 10.1016/j.mechrescom.2011.11.004.
- [27] Y. Fan *et al.*, "Characterization of Exercise-Induced Myocardium Growth Using Finite Element Modeling and Bayesian Optimization," *Front. Physiol.*, vol. 12, 2021, Accessed: Apr. 05, 2022. [Online]. Available: <https://www.frontiersin.org/article/10.3389/fphys.2021.694940>
- [28] C. M. Witzenburg and J. W. Holmes, "The Impact of Hemodynamic Reflex Compensation Following Myocardial Infarction on Subsequent Ventricular Remodeling," *J. Biomech. Eng.*, vol. 141, no. 9, p. 091010, Sep. 2019, doi: 10.1115/1.4043867.
- [29] N. Côté *et al.*, "Impact of Vascular Hemodynamics on Aortic Stenosis Evaluation: New Insights Into the Pathophysiology of Normal Flow—Small Aortic Valve Area—Low Gradient Pattern," *J. Am. Heart Assoc.*, vol. 6, no. 7, p. e006276, doi: 10.1161/JAHA.117.006276.
- [30] E. Rondanina and P. H. M. Bovendeerd, "Stimulus–effect relations for left ventricular growth obtained with a simple multi-scale model: the influence of hemodynamic feedback," *Biomech. Model. Mechanobiol.*, vol. 19, no. 6, pp. 2111–2126, Dec. 2020, doi: 10.1007/s10237-020-01327-2.
- [31] W. P. Santamore and D. Burkhoff, "Hemodynamic consequences of ventricular interaction as assessed by model analysis," *Am. J. Physiol.-Heart Circ. Physiol.*, vol. 260, no. 1, pp. H146–H157, Jan. 1991, doi: 10.1152/ajpheart.1991.260.1.H146.
- [32] M. Armstrong, C. C. Kerndt, and R. A. Moore, "Physiology, Baroreceptors," in *StatPearls*, Treasure Island (FL): StatPearls Publishing, 2022. Accessed: Apr. 05, 2022. [Online]. Available: <http://www.ncbi.nlm.nih.gov/books/NBK538172/>
- [33] D. A. Beard, K. H. Pettersen, B. E. Carlson, S. W. Omholt, and S. M. Bugenhagen, "A computational analysis of the long-term regulation of arterial pressure," *F1000Research*, vol. 2, Dec. 2013, doi: 10.12688/f1000research.2-208.v2.
- [34] M. W. Chapleau, J. Lu, G. Hajduczuk, and F. M. Abboud, "Mechanism of baroreceptor adaptation in dogs: attenuation of adaptation by the K<sup>+</sup> channel blocker 4-aminopyridine.," *J. Physiol.*, vol. 462, no. 1, pp. 291–306, Mar. 1993, doi: 10.1113/jphysiol.1993.sp019556.
- [35] A. Mahdi, J. Sturdy, J. T. Ottesen, and M. S. Olufsen, "Modeling the Afferent Dynamics of the Baroreflex Control System," *PLOS Comput. Biol.*, vol. 9, no. 12, p. e1003384, Dec. 2013, doi: 10.1371/journal.pcbi.1003384.

- [36] F. S. Zamo *et al.*, “Hemodynamic, Morphometric and Autonomic Patterns in Hypertensive Rats - Renin-Angiotensin System Modulation,” *Clinics*, vol. 65, no. 1, pp. 85–92, Jan. 2010, doi: 10.1590/S1807-59322010000100013.
- [37] J. H. Fountain and S. L. Lappin, *Physiology, Renin Angiotensin System*. StatPearls Publishing, 2021. Accessed: Jan. 18, 2022. [Online]. Available: <https://www.ncbi.nlm.nih.gov/books/NBK470410/>
- [38] C. W. Harshaw, W. Grossman, A. B. Munro, and L. P. McLaurin, “Reduced systemic vascular resistance as therapy for severe mitral regurgitation of valvular origin,” *Ann. Intern. Med.*, vol. 83, no. 3, pp. 312–316, Sep. 1975, doi: 10.7326/0003-4819-83-3-312.
- [39] A. C. Guyton, “The relationship of cardiac output and arterial pressure control,” *Circulation*, vol. 64, no. 6, pp. 1079–1088, Dec. 1981, doi: 10.1161/01.cir.64.6.1079.
- [40] D. Burkhoff and J. V. Tyberg, “Why does pulmonary venous pressure rise after onset of LV dysfunction: a theoretical analysis,” *Am. J. Physiol.-Heart Circ. Physiol.*, vol. 265, no. 5, pp. H1819–H1828, Nov. 1993, doi: 10.1152/ajpheart.1993.265.5.H1819.
- [41] Y. Pirahanchi and B. Bordoni, “Anatomy, Head and Neck, Carotid Baroreceptors,” in *StatPearls*, Treasure Island (FL): StatPearls Publishing, 2022. Accessed: Mar. 19, 2022. [Online]. Available: <http://www.ncbi.nlm.nih.gov/books/NBK537223/>
- [42] H. M. Coleridge, J. C. Coleridge, E. R. Poore, A. M. Roberts, and H. D. Schultz, “Aortic wall properties and baroreceptor behaviour at normal arterial pressure and in acute hypertensive resetting in dogs,” *J. Physiol.*, vol. 350, no. 1, pp. 309–326, May 1984, doi: 10.1113/jphysiol.1984.sp015203.
- [43] A. Baretta *et al.*, “Virtual surgeries in patients with congenital heart disease: a multi-scale modelling test case,” *Philos. Trans. R. Soc. Math. Phys. Eng. Sci.*, vol. 369, no. 1954, pp. 4316–4330, Nov. 2011, doi: 10.1098/rsta.2011.0130.
- [44] “Find minimum of unconstrained multivariable function using derivative-free method - MATLAB fminsearch.” <https://www.mathworks.com/help/matlab/ref/fminsearch.html> (accessed Jan. 19, 2022).
- [45] “Find minimum of constrained nonlinear multivariable function - MATLAB fmincon.” <https://www.mathworks.com/help/optim/ug/fmincon.html> (accessed Feb. 06, 2022).
- [46] P. A. Munch, M. C. Andresen, and A. M. Brown, “Rapid resetting of aortic baroreceptors in vitro,” *Am. J. Physiol.-Heart Circ. Physiol.*, vol. 244, no. 5, pp. H672–H680, May 1983, doi: 10.1152/ajpheart.1983.244.5.H672.
- [47] J. W. Mccubbin, J. H. Green, and I. H. Page, “Baroreceptor function in chronic renal hypertension,” *Circ. Res.*, vol. 4, no. 2, pp. 205–210, Mar. 1956, doi: 10.1161/01.res.4.2.205.
- [48] J. L. Osborn, “Relation between sodium intake, renal function, and the regulation of arterial pressure,” *Hypertension*, vol. 17, no. 1\_Suppl, pp. I91–I91, Jan. 1991, doi: 10.1161/01.HYP.17.1\_Suppl.I91.

- [49] D. Rizzoni, C. Agabiti-Rosei, and E. Agabiti-Rosei, "Hemodynamic Consequences of Changes in Microvascular Structure," *Am. J. Hypertens.*, vol. 30, no. 10, pp. 939–946, Oct. 2017, doi: 10.1093/ajh/hpx032.
- [50] B. Folkow, "The Haemodynamic Consequences of Adaptive Structural Changes of the Resistance Vessels in Hypertension," *Clin. Sci.*, vol. 41, no. 1, pp. 1–12, Jul. 1971, doi: 10.1042/cs0410001.
- [51] V. T. Nkomo, J. M. Gardin, T. N. Skelton, J. S. Gottdiener, C. G. Scott, and M. Enriquez-Sarano, "Burden of valvular heart diseases: a population-based study," *The Lancet*, vol. 368, no. 9540, pp. 1005–1011, Sep. 2006, doi: 10.1016/S0140-6736(06)69208-8.
- [52] M. Gössl and P. Sorajja, "MitraClip patient selection: inclusion and exclusion criteria for optimal outcomes," *Ann. Cardiothorac. Surg.*, vol. 7, no. 6, pp. 771–775, Nov. 2018, doi: 10.21037/acs.2018.08.04.
- [53] T. Ondrus, M. Penicka, M. Kotrc, M. Vanderheyden, and J. Bartunek, "MitraClip: Catheter-based treatment of mitral regurgitation," *Cor Vasa*, vol. 59, no. 1, pp. e85–e91, Feb. 2017, doi: 10.1016/j.crvasa.2017.01.015.
- [54] H. J. Brouwer *et al.*, "Left ventricular remodelling patterns after MitraClip implantation in patients with severe mitral valve regurgitation: mechanistic insights and prognostic implications," *Eur. Heart J. - Cardiovasc. Imaging*, vol. 20, no. 3, pp. 307–313, Mar. 2019, doi: 10.1093/ehjci/jey088.
- [55] P. L. Whitlow *et al.*, "Acute and 12-Month Results With Catheter-Based Mitral Valve Leaflet Repair," *J. Am. Coll. Cardiol.*, vol. 59, no. 2, pp. 130–139, Jan. 2012, doi: 10.1016/j.jacc.2011.08.067.
- [56] O. Gaemperli *et al.*, "Real-Time Left Ventricular Pressure-Volume Loops During Percutaneous Mitral Valve Repair With the MitraClip System," *Circulation*, vol. 127, no. 9, pp. 1018–1027, Mar. 2013, doi: 10.1161/CIRCULATIONAHA.112.135061.
- [57] A. Kosaraju, A. Goyal, Y. Grigороva, and A. N. Makaryus, "Left Ventricular Ejection Fraction," in *StatPearls*, Treasure Island (FL): StatPearls Publishing, 2022. Accessed: Mar. 25, 2022. [Online]. Available: <http://www.ncbi.nlm.nih.gov/books/NBK459131/>
- [58] "The Continuity Equation (The Principle of Continuity)," *ECG & ECHO*. <https://ecgwaves.com/topic/the-continuity-equation/> (accessed Mar. 29, 2022).
- [59] J. Garcia, L. Kadem, E. Larose, M.-A. Clavel, and P. Pibarot, "Comparison between cardiovascular magnetic resonance and transthoracic doppler echocardiography for the estimation of effective orifice area in aortic stenosis," *J. Cardiovasc. Magn. Reson.*, vol. 13, no. 1, p. 25, Apr. 2011, doi: 10.1186/1532-429X-13-25.
- [60] R. P. Kelly *et al.*, "Effective arterial elastance as index of arterial vascular load in humans," *Circulation*, vol. 86, no. 2, pp. 513–521, Aug. 1992, doi: 10.1161/01.CIR.86.2.513.

- [61] C.-H. Chen *et al.*, "Noninvasive single-beat determination of left ventricular end-systolic elastance in humans," *J. Am. Coll. Cardiol.*, vol. 38, no. 7, pp. 2028–2034, Dec. 2001, doi: 10.1016/S0735-1097(01)01651-5.
- [62] I. Pagel *et al.*, "Cardiac and Renal Effects of Growth Hormone in Volume Overload–Induced Heart Failure," *Hypertension*, vol. 39, no. 1, pp. 57–62, Jan. 2002, doi: 10.1161/hy0102.098323.